

Kingdom of Saudi Arabia
Ministry of Education
Umm Al-Qura University
Faculty of Applied Science
Physics Department



**Preparation, Characterization and Spectroscopic Studies of Metal
Nanoparticles and Their Applications in The Environment**

**A Thesis Submitted to Physics Department Faculty of Applied Science
Umm Al-Qura University**

In Partial Fulfillment of the Requirements for the Degree of Master of Physics

By

Najwa Ali Mohammad Barnawi

(B. Sc. In Physics)

No. 43880124

Under Supervision

Prof. Dr. Roshdi Seoudi Mohamed Awed

Prof. of Spectroscopy and Nanotechnology – Physics Department

Faculty of Applied Science – Umm Al-Qura University

Assistant Supervisor

Prof. Dr. Saud Hamed Allehyani

Prof. of Medical Physics – Physics Department

Faculty of Applied Science – Umm Al-Qura University

1441 – 2020

Kingdom of Saudi Arabia
Ministry of Education
Umm Al-Qura University
Faculty of Applied Science
Physics Department



**Preparation, Characterization and Spectroscopic Studies of Metal
Nanoparticles and Their Applications in The Environment**

**A Thesis Submitted to Physics Department Faculty of Applied Science
Umm Al-Qura University**

In Partial Fulfillment of the Requirements for the Degree of Master of Physics

By




Najwa Ali Mohammad Barnawi

(B. Sc. In Physics)

No. 43880124

This Thesis was Discussed and Approved in 18/9/1441 AH

Committee of Examiners

Name	Committee of Examiners	Signature
Prof. Dr. Roshdi Seoudi	Advisor	
Prof. Dr. Yosry Moustafa	Examiner	
Prof. Dr. Said Attia	Examiner	

بِسْمِ اللَّهِ الرَّحْمَنِ الرَّحِيمِ

Acknowledgments

First and foremost, all praises and thanks to **God Al-mighty** for his guidance and shower of blessings throughout my research work to complete this successfully.

I am honored to express my sincere gratitude to my supervisor **Prof. Dr. Roshdi Seoudi Mohamed Awed**, Professor of Spectroscopy and Nanotechnology, Physics Department, Faculty of Applied Science, Umm Al-Qura University, for continuous support with patience, motivation, enthusiasm, and immense of knowledge. His guidance and fruitful discussions helped me in the whole time to complete my research and writing this thesis.

I also would thank my assistant supervisor **Prof. Dr. Saud Hamed Allehyani**, Professor of Medical Physics, Faculty of Applied Science, Umm Al-Qura University, for his support during this work.

I would like to acknowledge everyone who played a role in my academic accomplishments.

Finally, I must express my very profound gratitude to **my parents** for their prayers and support.

I would also like to thank my **brothers and sisters**, especially **Nosibah**, for their helping and motivation.

Najwa Ali Mohammad Barnawi

Appendices

Contents

NO.	Titles	Pages
<i>Appendices</i>		
	<i>Abstract</i>	<i>VIII</i>
	<i>Summary</i>	<i>IX</i>
	<i>List of Abbreviations</i>	<i>XVI</i>
	<i>List of Figures</i>	<i>XVIII</i>
	<i>List of Tables</i>	<i>XXVI</i>
 <i>Chapter 1</i> 		
<i>General Introduction and Literature Survey</i>		
	<i>1.1 Historical Overview of Nano</i>	<i>1</i>
	<i>1.2 Definition of Nanometer Scale, Nanoscience, and Nanotechnology</i>	<i>1</i>
	<i>1.3 Classification of Nanomaterials Based on Dimensions</i>	<i>2</i>
	1.3.1 Zero-Dimension (0-D) Nanomaterials	<i>3</i>
	1.3.2 One-Dimension (1-D) Nanomaterials	<i>4</i>
	1.3.3 Two-Dimension (2-D) Nanomaterials.....	<i>4</i>
	1.3.4 Three-Dimension (3-D) Nanomaterials.....	<i>5</i>
	<i>1.4 Properties of Nanomaterials</i>	<i>6</i>
	1.4.1 Surface Energy of Nanomaterials.....	<i>6</i>
	1.4.2 Quantum Size Effect of Nanomaterials	<i>7</i>
	1.4.3 Mechanical Properties of Nanomaterials.....	<i>9</i>
	1.4.4 Magnetic Properties of Nanomaterials	<i>11</i>

1.4.5 Optical Properties of Nanomaterials	14
<i>1.5 Preparation of Nanomaterials</i>	<i>16</i>
1.5.1 Top-Down Method	17
1.5.2 Bottom-Up Method.....	17
1.5.3 Fabrication of Metal Nanoparticles	19
1.5.4 Fabrication of Magnetic Nanoparticles	20
<i>1.6 Applications of Nanotechnology</i>	<i>20</i>
1.6.1 In Agriculture and Food	20
1.6.2 In Medicine	21
1.6.3 In Energy	22
1.6.4 In Water Remediation.....	22
1.6.4.1 Filtration.....	23
1.6.4.2 Photocatalysis.....	23
<i>1.7 Literature Survey</i>	<i>24</i>
<i>1.8 Aims of the Thesis</i>	<i>30</i>

Chapter 2

Theoretical Consideration

<i>2.1 Introduction of Light Radiation</i>	<i>32</i>
2.1.1 Electromagnetic (EM) Radiation.....	32
<i>2.2 UV-Visible Spectroscopy</i>	<i>34</i>
2.2.1 The Concept of UV-Visible Spectrometer	34
2.2.2 The Absorption and Beer-Lambert's Law.....	35

2.2.3 Theory of Ultraviolet-Visible Electronic Spectroscopy	37
2.3 Transmission Electron Microscopy (TEM)	39
2.3.1 The Principle of Transmission Electron Microscope Technique	40
2.4 Theory of X-Ray Diffraction	43
2.4.1 Bragg's Law.....	43
2.5 Infrared (IR) Spectroscopy	45
2.5.1 Theoretical Basics of Infrared Radiation.....	45
2.5.2 Mathematical Consideration of Absorbing Infrared Spectra	47
2.5.3 Hook's Law for Stretching Vibrations	49
2.5.4 Number of Vibration Modes in Infrared Spectra	52

Chapter 3

Methodology and Instruments

3.1 Materials.....	54
3.1.1 Gold (III) Chloride Hydrate ($\mathbf{HAuCl_4 \cdot H_2O}$)	54
3.1.2 Silver Nitrate ($\mathbf{AgNO_3}$)	54
3.1.3 Sodium Dodecyl Sulfate ($\mathbf{C_{12}H_{25}NaO_4S}$)	55
3.1.4 Iron (II) Chloride Tetrahydrate (Ferrous Chloride) ($\mathbf{FeCl_2 \cdot 4H_2O}$).....	55
3.1.5 Iron (III) Nitrate Nonahydrate (Ferric Nitrate) ($\mathbf{Fe(NO_3)_3 \cdot 9H_2O}$)	56
3.1.6 Chitosan ($\mathbf{C_6H_{11}NO_4}_n$).....	56
3.1.7 Acetic Acid ($\mathbf{C_2H_4O_2}$).....	57
3.1.8 Sodium Hydroxide (\mathbf{NaOH}).....	57
3.1.9 Absolute Ethanol ($\mathbf{C_2H_5OH}$)	58

3.1.10 Sodium Diphosphate Monobasic ($\text{NaH}_2\text{PO}_4 \cdot \text{H}_2\text{O}$).....	58
3.1.11 Disodium Hydrogen Orthophosphate Anhydrous (Na_2HPO_4)	58
3.1.12 Ammonium Hydroxide (NH_4OH)	59
3.1.13 Cobalt (II) Chloride 6-Hydrate (Cobaltous Chloride) ($\text{CoCl}_2 \cdot 6\text{H}_2\text{O}$)59	
3.1.14 Hydrazine Hydrate ($\text{N}_2\text{H}_4 \cdot \text{H}_2\text{O}$).....	60
3.1.15 Nickel (II) Nitrate Hexahydrate ($\text{Ni}(\text{NO}_3)_2 \cdot 6\text{H}_2\text{O}$)	60
3.2 <i>Experimental Methods</i>	60
3.2.1 Green Synthesis of Gold and Silver Nanoparticles	60
3.2.1a Preparation of Gold Nanoparticles with Different Concentrations of Lemon Extract	61
3.2.1b Preparation of Silver Nanoparticles with Different Concentrations of Silver Nitrate.....	62
3.2.2 Synthesis of Iron and Cobalt as a Magnetic Nanoparticles.....	64
3.2.2a Preparation of Iron Nanoparticles Capped by Chitosan at Different Concentrations of Iron	65
3.2.2b Preparation of Cobalt Nanoparticles with Different Concentrations of Sodium Hydroxide.....	67
3.3 <i>Instrumentation Techniques</i>	70
3.3.1 Ultraviolet/Visible Spectrophotometer Technique (UV-Vis)	70
3.3.2 High-Resolution Transmission Electron Microscopy (HR-TEM)	72
3.3.3 X-Ray Diffraction Spectrometer Technique (XRD)	74
3.3.4 Fourier Transform Infrared Spectroscopy (FTIR).....	76

Chapter 4**Results and Discussion**

<i>4.1 Ultraviolet-Visible Spectroscopy</i>	79
4.1.1 Ultraviolet-Visible Spectra of Gold Nanoparticles Prepared at Different Concentrations of Lemon	79
4.1.2 Ultraviolet-Visible Spectra of Silver Nanoparticles Prepared at Different Molar Ratio of Silver Nitrate.....	83
4.1.3 Ultraviolet-Visible Spectra of Iron Nanoparticles Prepared at Different Molarity of Iron Salt	85
4.1.4 Ultraviolet-Visible Spectra of Cobalt Nanoparticles Prepared at Different Concentrations of Sodium Hydroxide	86
<i>4.2 High-Resolution Transmission Electron Microscopy</i>	88
4.2.1 HR-Transmission Electron Microscopy of Gold Nanoparticles Prepared at Different Concentrations of Lemon Extract	88
4.2.2 HR-Transmission Electron Microscopy of Silver Nanoparticles Prepared at Different Molar Ratio of Silver Nitrate	91
4.2.3 HR-Transmission Electron Microscopy of Iron Nanoparticles Prepared at Different Molarity of Iron Salt	93
4.2.4 HR-Transmission Electron Microscopy of Cobalt Nanoparticles Prepared at Different Concentrations of Sodium Hydroxide	96
<i>4.3 X-Ray Diffraction Pattern</i>	99
4.3.1 X-Ray Diffraction for Iron Nanoparticle Prepared at Different Concentrations of Iron Salt.....	99

4.3.2 X-Ray Diffraction of Cobalt Nanoparticles Prepared at Different Concentrations of Sodium Hydroxide	100
<i>4.4 Fourier Transform Infrared Spectroscopy</i>	<i>103</i>
4.4.1 Fourier Transform Infrared Spectroscopy of Gold Nanoparticle Capped with Different Concentrations of Lemon Extract	103
4.4.2 Fourier Transform Infrared Spectroscopy of Silver Nanoparticle Capped by Lemon Extract	106
4.4.3 Fourier Transform Infrared Spectroscopy of Iron Nanoparticle Prepared at Different Concentrations of Ion Salt.....	109
4.4.4 Fourier Transform Infrared Spectroscopy of Cobalt Nanoparticles Prepared at Different Concentrations of Sodium Hydroxide	112
<i>4.5 Applications of Nanoparticles in Water Purification.....</i>	<i>115</i>
4.5.1 UV-Visible Spectroscopy with Different Concentrations of Nickel Nitrate	115
4.5.2 Study the Alternating in Nickel Salt Concentrations Dissolved in Water After Passing through Imbibed Filter by Gold Nanoparticles.....	117
4.5.3 Study the Alternating in Nickel Salt Concentrations Dissolved in Water After Passing through Imbibed Filter by Silver Nanoparticles	120
4.5.4 Study the Alternating in Nickel Salt Concentrations Dissolved in Water After Passing through Imbibed Filter by Iron Nanoparticles	123
4.5.5 Study the Alternating in Nickel Salt Concentrations Dissolved in Water After Passing through Imbibed Filter by Cobalt Nanoparticles	125
<i>Conclusions.....</i>	<i>130</i>
<i>References.....</i>	<i>132</i>

Arabic Summary.....148

Abstract

This thesis aimed to study the preparation method of noble metals nanoparticles (AuNPs and AgNPs) in green synthesis and some of magnetic nanoparticles as (FeNPs and CoNPs) in different sizes using bottom-up approach.

To study the properties of prepared nanoparticles, whole samples were characterized by transmission electron microscope, X-ray diffraction, and Fourier transform infrared spectroscopy. Besides, the spectroscopic studies of synthesized nanoparticles were evaluated via ultraviolet-visible spectroscopy. In addition, some of prepared samples were applied into filter element in order to dilute the concentration of heavy metals (Ni) in waters.

A comparison between theoretical and experimental results in Fourier transform infrared spectroscopy characterization was done. Also, the application results were taken before and after nanoparticles effects, which suggests a good result in water enhancement process.

This study recommends to use different nanoparticles as nickel NiNPs in groundwater treatments. It could be also recommended to utilize inductive coupled plasma or atomic absorption spectroscopy (AAS) instead of ultraviolet-visible spectroscopy in application analysis results.

Summary

This thesis focused on studying the preparation, characterization, and spectroscopic studies of noble metals (gold and silver) and some magnetic nanoparticles (iron and cobalt) with different particles size. Besides, examine the effect of our prepared nanoparticle samples on decreasing the concentration of nickel elements in water. To be informed, this thesis is containing four chapters, where the first one displays a general introduction of nanomaterials with some literature reviews related to our studies. The second one is explaining the mathematical expression of characterizing our samples, while the third chapter exposes the experimental methods of nanoparticle preparation, including used instrumentation devices. Eventually, chapter four discusses the outlined results in the whole thesis.

Chapter 1

This chapter is divided into two main parts, which is a general introduction of nanomaterials and literature review. The first part is subdivided into several sections beginning with a historical overview of nano and some definitions of nanomaterial terminologies. Follow that, classification of nanomaterials according to their dimensions. Besides, the main factor which affects on nanoparticle properties as surface energy and quantum size effect was explained including the mechanical, magnetic, and optical properties. In addition, the general methods of nanomaterials preparation were presented in this chapter with both types, which is either top-down method or bottom-up method involving physical and chemical fabrication techniques as ball milling, chemical vapor deposition, sol-gel, and laser ablation. The fabrication also illustrates metal and magnetic nanoparticle preparation. At the end of this part, the application of nanomaterials in agriculture, food, medicine, energy, and water remediation was demonstrated.

The second part of this chapter outline a number of previous researches regarding of synthesized method for gold, silver, iron, and cobalt nanoparticles and their application in environments. Furthermore, an objective plan was evident at the end of the chapter.

Chapter 2

This chapter clarifies the theoretical background and mathematical basics for measurement device that utilized in characterization purpose in our prepared samples. Starting with introduction of light radiation passing through theoretical electromagnetic radiation. Follow that, an explanation of ultraviolet-visible spectroscopy concept and discussion of theoretical absorbance light by Beer-Lambert's law. Then the theory of UV electronic transition spectroscopy was demonstrated. In addition, The principle of transmission electron microscope technique was discussed with details information about electron beam generating and transferring through specimen as well as the theoretical consideration of x-ray diffraction was mentioned with details configuration of Bragg's law. Last of all, the basics of infrared spectroscopy was represented with a mathematical proof of absorbing spectra and stretching vibrations. The normal vibration modes of infrared were also illustrated in this chapter.

Chapter 3

This chapter was opened with chemical materials used in our preparation samples. Afterward, the methodology of nanoparticles synthesized was demonstrated. In the last of this chapter, the utilized characterization techniques were illustrated.

It begins with gold nanoparticles methodology, AuNPs were prepared by using a constant concentration of gold chloride hydrate $HAuCl_4 \cdot H_2O$ and different

concentrations of lemon extract. In contrast, silver nanoparticles AgNPs were synthesized with a various ratio of silver nitrate $AgNO_3$ and constant quantity of lemon extract. On the other hand, the iron nanoparticles FeNPs coated with chitosan was prepared with a different molar ratio of iron salt ($Fe^{3+}: Fe^{2+}$) and fixed concentration for both chitosan and sodium hydroxide $NaOH$. While the cobalt nanoparticles CoNPs were synthesized by adding equivalent ratio of cobalt salt $CoCl_2 \cdot 6H_2O$ and various concentrations of sodium hydroxide $NaOH$. Follow that, four characterization techniques of prepared nanoparticles covering explanation of devices parts; these devices involve ultraviolet-visible spectroscopy, transmission electron microscope, x-ray diffraction, and Fourier transform infrared spectroscopy.

Chapter 4

In this chapter, the obtained results from prepared samples were discussed and interpreted. The results of UV-Vis spectroscopy for gold nanoparticles AuNPs were demonstrated in range (300 nm – 900 nm) with surface plasmonic resonance SPR band position appeared at wavelength 564 nm, 556 nm, and 548 nm. There is an inverse relation between lemon extract and band position SPR it is shifted to lower wavelength (blue shift); This shift indicates decreasing particle size with increasing lemon extract. While the UV-Vis measurement of silver nanoparticle AgNPs illustrated in a range of (320 nm – 890 nm) representing surface plasmon resonance SPR appeared at wavelength 432 nm, 452 nm, and 448 nm. The recorded notes is wavelength increasing with adding more concentration of $AgNO_3$ and then decrease again. The increasing of AgNPs wavelength is interpreted as the silver nanoparticles aggregate Ag atoms by reducing Ag^+ ions into nanoscale so its particle size increase with increasing $AgNO_3$ then shifted to red-shift, and the extra amount of precursor cause what named blue shift due to new nucleation centers, which would appear as really small metal NPs. On the contrary, the UV-Vis of iron nanoparticles FeNPs

were characterized in the wavelength range (205 nm – 800 nm) with absorption peak appeared at 336 nm, 340 nm, and 344 nm. There was a direct relationship between increasing iron salt ratio and wavelength shifted (redshift) as traditionally known, the particle size and wavelength position have a direct relation. Hence of that, we interpreted increasing in wavelength has no doubt increasing in particle size due to increasing ions in solution, which allows for more nucleation. Furthermore, the results of UV-Vis spectra of prepared cobalt nanoparticles CoNPs were measured using spectral wavelength in a range of (250 nm – 800 nm) has an absorption band appeared at 520 nm, 548 nm, and 528 nm. The increasing and then decreasing again in wavelength of cobalt samples is interpreted as, the increasing in wavelength lead to increase in particle size due to the increasing sodium hydroxide in solution, which acts in nanoparticle formation, and the decreasing again is maybe due to some nanoparticles transfers to nanorod and nanofiber, the difference in band position indicating of forming CoNPs in different sizes.

The whole prepared nanoparticles were characterized via high-resolution transmission electron microscope HR-TEM, and their average particle size was estimated. The HR-TEM of AuNPs is shown spherical shapes with other different geometrical shapes as trigonal, hexagonal, trapezoidal, pentagonal, rectangular, small rod, and oval. The average particle size of AuNPs for spherical shapes was calculated according to Gaussian distribution, and it found to be 54 nm, 22 nm, and 28 nm. These results notified that some results agree with UV-vis while others not, which may be owing to nonuniform shapes beside spherical shapes that appeared in visualized images in the same sample. In contrast, the HR-TEM of AgNPs shows a random distribution with almost spherical shapes and smooth edges it also has other geometrical shapes such ellipsoidal and hexagonal. The average particle size of AgNPs according to Gaussian distribution for spherical particles in image and it

found to be 31 nm, 15 nm, and 28 nm. This result is incompatible with surface plasmon band position of UV data it could attribute to the obtained aggregation during visualize TEM. On the other hand, the HR-TEM of FeNPs were characterized after and before drying. The results demonstrate a random distribution of non-uniform and homogenous particles besides other spherical shapes. The average particle size of spherical shape was 22 nm, 17 nm, and 32 nm for iron after drying, as well as it has 10 nm, 9 nm, and 18 nm for iron before drying. The result clarifies that the FeNPs after drying were larger particle sizes than FeNPs before drying; this probably due to the aggregation of FeNPs after heating has happened. Moreover, the visualization image of HR-TEM for CoNPs show a various geometrical shape in the first sample with spherical, ellipsoidal, pentagonal, and hexagonal in addition to some aggregation particles. This sample has average particle size 27 nm from Gaussian distribution. The morphology of the last two samples appeared as nanorod and nanofiber with an aspect ratio between 5.2 ~ 8.5 nm and 5.6 ~ 8.33 nm. It also has ambiguous particles in some regions; it almost does not have spherical shapes that why the average particle size was ignored in both samples.

The x-ray diffraction result of prepared iron nanoparticles samples was characterized in $2\theta^\circ$ with a range between ($25^\circ \sim 60^\circ$). Its shown that the diffraction pattern of FeNPs has a direct relationship between iron salt ratio and peaks intensity, as the iron salt increase the diffraction pattern peaks be clear and sharp with high intensity. Moreover, the average crystalline size of FeNPs was calculated using Scherrer's equation, and it found to be 38.2 nm, 34.1 nm, and 49.5 nm. Equally important, the XRD pattern of prepared cobalt nanoparticles were measured in $2\theta^\circ$ with a range between ($30^\circ \sim 60^\circ$). The result shows that there is a direct relationship between concentration of sodium hydroxide and peak intensity, as the concentration of sodium hydroxide increase the diffraction pattern intensity increase. In addition,

the crystalline size of CoNPs was estimated via Scherrer's equation, and it found to be 32.9 nm, 31.3 nm, and 41.5 nm.

The results of Fourier transform infrared spectroscopy of gold nanoparticles capped by lemon extract have observed peak at 621 cm^{-1} , 609 cm^{-1} , and 602 cm^{-1} assigned for Au – O stretching vibration. While the FTIR of silver nanoparticles capped by lemon extract have peaks at 567 cm^{-1} , 592 cm^{-1} , and 587 cm^{-1} , which assigned for Ag – O stretching vibration. In addition, the observed peak in iron nanoparticles sample capped by chitosan has appeared at 642 cm^{-1} , 647 cm^{-1} , and 650 cm^{-1} was assigned for Fe – O stretching vibration while the cobalt nanoparticles have peaks at 512 cm^{-1} , 528 cm^{-1} , and 532 cm^{-1} assigned for Co – O stretching vibration. As a matter of fact, the oxygen here comes from capping materials. The theoretical results of prepared nanoparticles samples were calculated, and it found to be 757.04 cm^{-1} , 778.76 cm^{-1} , 824.33 cm^{-1} , and 819.43 cm^{-1} , which assigned to Au – O, Ag – O, Fe – O, and Co – O respectively. It noted that there are differences between theoretical and practical results, which interpreted as a consequence of presence nanoparticles to be coordinated with other functional groups. Every sample had different peaks which is relating to the functional groups existing in capping of our samples as C – H, N – H, C – C, C = O, and C – C as well as it has similar peaks at around 3400 cm^{-1} assigned to O – H functional group, which relates to presented water in samples.

The effect of prepared nanoparticles samples in decreasing nickel concentration was studied by applying them into WILKERSON filter element then pass different concentrations of nickel solution through the filter. It noted that there is a relationship between absorbance intensity and concentration, as the concentration of nickel increase the absorbance increase according to Beer-Lambert law. Besides, the absorbance intensity of nickel solution decrease after using

nanoparticles as impregnated onto membrane filter. Important to note, at low concentration of nickel element, the AgNPs and CoNPs are not active as much as AuNPs and FeNPs, which is owing to electronegativity of elements. In contrast, at high concentration, the CoNPs is more efficient than AuNPs, FeNPs, and AgNPs, respectively. This means it could be utilized prepared nanoparticles in water purification from heavy metals.

List of Abbreviations

Acronyms	Definition
0 – D, 0D	Zero Dimension
1 – D, 1D	One Dimension
2 – D, 2D	Two Dimensions
3 – D, 3D	Three Dimensions
AFM	Atomic Force Microscope
AgNO₃	Chemical Formula for Silver Nitrate
AgNPs	Silver Nanoparticles
AuNPs	Gold Nanoparticles
BPE	Banana Peel Extract
C₂H₅OH	Chemical Formula of Ethanol
(C₆H₁₁NO₄)_n	Chemical Formula of Chitosan
CCD	Charged Coupled Device
CH₃COOH	Chemical Formula for Acetic Acid
Co	Cobalt
CO(OH)₂	Chemical Formula for Cobalt Hydroxide
Co₃O₄	Chemical Formula for Cobalt Oxide
CoCl₂.6H₂O	Chemical Formula of Cobalt (II) Chloride 6-Hydrate (Cobaltous Chloride)
CoNPs	Cobalt Nanoparticles
CSNPs	Core-Shell Nanoparticles
CVD	Chemical Vapor Deposition
DLS	Dynamic Light Scattering
EDAX, EDS, EDX	Energy Dispersive X-Ray Spectroscopy
E_g	Energy Gab
EM Radiation	Electromagnetic Radiation
Fe	Iron
Fe(NO₃)₃.9H₂O	Chemical Formula for Iron (III) Nitrate Nonahydrate (Ferric Nitrate)
Fe₂O₃, Fe₃O₄	Chemical Formula of Iron Oxide

FeCl₂.4H₂O	Chemical Formula Iron (II) Chloride Tetrahydrate (Ferrous Chloride)
FeNPs	Iron Nanoparticles
FESEM	Field Emission Scanning Electron Microscope
FIR	Far-Infrared
HAuCl₄.H₂O	Chemical formula for Gold (III) Chloride Hydrate
HOMO	Highest Occupied Molecular Orbital (valence band)
HR-TEM	High-Resolution Transmission Electron Microscope
IR, FTIR, FT-IR	Fourier Transform Infrared Radiation
KBr	Chemical Formula of Potassium Bromide
LUMO	Lowest Unoccupied Molecular Orbital (conduction band)
MIR	Mid-Infrared
N₂H₄.H₂O	Chemical Formula of Hydrazine Hydrate
Na₂HPO₄	Chemical Formula of Disodium Hydrogen Orthophosphate Anhydrous
NaBH₄	Chemical Formula of Sodium Borohydride
NaH₂PO₄.H₂O	Chemical formula of Sodium Diphosphate Monobasic
NaOH	Chemical Formula for Sodium Hydroxide
NH₄OH	Chemical Formula of Ammonium hydroxide
Ni	Nickel
Ni(NO₃)₂.6H₂O	Chemical Formula of Nickel (II) Nitrate Hexahydrate
NIR	Near-Infrared
NPs	Nanoparticles
PDA	Photo Detector Array
PMT	Photomultiplier Tube
PVC	Physical Vapor Deposition
SDS, C₁₂H₂₅NaO₄S	Sodium Dodecyl Sulphate
SEM	Scanning Electron Microscope
SPR	Surface Plasmon Resonance
TEM	Transmission Electron Microscope
TGA	Thermogravimetric Analysis
UV-Vis	Ultraviolet-Visible
XRD	X-Ray Diffraction

List of Figures

NO.	Titles	Pages
	Figure 1.1: Comparison of the nanometer scale with other scales.	2
	Figure 1.2: TEM of gold spherical nanoparticles and cluster in zero dimension.....	3
	Figure 1.3: SEM of carbon nanofibers as an example of a 1-dimension of nanomaterials.	4
	Figure 1.4: SEM of Ni/Al nanolayers as an example of 2-dimension nanomaterials	5
	Figure 1.5: Bulk polycrystal structure as an example of 3-dimension nanomaterials	6
	Figure 1.6: Schematic image explains the relation between surface area and particle size.....	7
	Figure 1.7: The comparison between particle size and energy gab.....	8
	Figure 1.8: Schematic illustrate the exciton between (HOMO-LUMO) band gab. .	9
	Figure 1.9: Schematic diagram illustrates the diamagnetic materials.	11
	Figure 1.10: Schematic diagram illustrates the paramagnetic materials.	12
	Figure 1.11: Schematic diagram illustrates the superparamagnetic materials.	12
	Figure 1.12: Schematic diagram illustrates the ferromagnetic materials.	13
	Figure 1.13: Schematic diagram illustrates the ferrimagnetic materials.	13
	Figure 1.14: Schematic diagram illustrates the antiferromagnetic materials.	13
	Figure 1.15: The size-dependent coercivity in a magnetic nanoparticle.....	14
	Figure 1.16: Schematic illustration of broken symmetry and functional form of the density of states in 1D, 2D, and 3D confined materials	16
	Figure 1.17: Schematic of nanoparticle Top-Down and Bottom-up approaches ...	16

Figure 1.18: Schematic diagram of the ball milling technique.....	17
Figure 1.19: Schematic sketch of a chemical vapor deposition (CVD) system	18
Figure 1.20: Diagram clarifies the mechanism of the Sol-Gel process.....	18
Figure 1.21: Schematic diagram of laser ablation technique.....	19
Figure 2.1: Plane of electromagnetic wave.....	32
Figure 2.2: Illustration of visible radiation in electromagnetic spectrum	32
Figure 2.3: Illustration represents the comparison between electromagnetic rays.	33
Figure 2.4: Schematic sketch for interaction light with matter.	34
Figure 2.5: Illustration of optical phenomena for absorbance and emission.....	35
Figure 2.6: Schematic illustrates incident and transmitted intensity in Beer Lambert's Laws.....	36
Figure 2.7: Electronic transitions and UV-Visible spectra in molecules.	38
Figure 2.8: Relative energies of molecular orbital and transitions between them.	38
Figure 2.9: Illustration of an electron gun and cathode connection in a microscope	42
Figure 2.10: Geometry for the interference of waves scattered from a crystal plane and Bragg's law illustration.	44
Figure 2.11: Schematic diagram illustrates the infrared spectral region within the electromagnetic spectrum.	46
Figure 2.12: Schematic representation of different molecular vibration modes showing bending and stretching vibrations.	47
Figure 2.13: Potential energy diagram of the harmonic oscillation model.	50
Figure 2.14: Schematic illustrates linear and non-linear chemical bonds.....	53
Figure 3.1: Chemical structure of gold (III) chloride hydrate.	54
Figure 3.2: Chemical structure of silver nitrate.	54
Figure 3.3: Chemical structure of SDS.....	55

Figure 3.4: Chemical structure of ferrous chloride.....	55
Figure 3.5: Chemical structure of ferric nitrate.	56
Figure 3.6: Chitosan chemical structure.	57
Figure 3.7: Chemical structure of acetic acid.	57
Figure 3.8: Sodium hydroxide chemical structure.....	57
Figure 3.9: Chemical structure of ethanol.	58
Figure 3.10: Sodium diphosphate monobasic chemical structure.	58
Figure 3.11: Chemical structure of disodium hydrogen orthophosphate anhydrous.	59
Figure 3.12: Ammonium hydroxide structure.	59
Figure 3.13: Chemical structure of cobaltous chloride.....	59
Figure 3.14: Chemical structure of hydrazine hydrate.	60
Figure 3.15: Chemical structure of nickel (II) nitrate hexahydrate.	60
Figure 3.16: Schematic diagram of experimental steps for preparing AuNPs sample S1.	61
Figure 3.17: Prepared gold nanoparticles samples.	62
Figure 3.18: Representation diagram of experimental steps for preparing AgNPs sample S4.	63
Figure 3.19: Prepared silver nanoparticles samples.	64
Figure 3.20: Representation diagram of experimental steps for preparing FeNPs sample S7.	66
Figure 3.21: Measurement samples of iron nanoparticles.....	67
Figure 3.22: Representation diagram of experimental steps for preparing CoNPs sample S10.....	68
Figure 3.23: Prepared and measurement samples of cobalt nanoparticles.....	69
Figure 3.24: Representation diagram of UV-Vis spectroscopy technique.	71

Figure 3.25: Illustration of TEM copper grid.	73
Figure 3.26: Illustration of an electron beam path in TEM.	73
Figure 3.27: Scheme of x-ray diffraction instrument.	75
Figure 3.28: Illustration of induced emission of characteristic x-ray from an atom with an electron beam.	76
Figure 3.29: Schematic diagram of a conventional Michelson interferometer.	78
Figure 4.1: Ultraviolet-visible spectra of gold nanoparticles prepared by adding 10 ml with concentration ($5.589 \times 10^{-3} M$) of gold salt with a different molar ratio of lemon extract; S1 (4 ml), S2 (5 ml), and S3 (6 ml).	80
Figure 4.2: Schematic illustration of a localized surface plasmon resonance.....	81
Figure 4.3: Plot illustrates the gold nanoparticle at maximum band position (SPR) against lemon extract concentration for S1, S2, and S3.	82
Figure 4.4: Ultraviolet-visible spectra of silver nanoparticles prepared by adding 200 ml with a different molar ratio of silver salt; S4 (3 mM), S5 (4 mM), and S6 (5 mM) with 40 ml lemon.	84
Figure 4.5: Ultraviolet-visible spectra of iron nanoparticles synthesized by adding a different molar ratio of iron salt (Fe^{3+} : Fe^{2+}); S7 (3.6 mM), S8 (4.6 mM), and S9 (5.6 mM) to 200 ml of prepared chitosan.	86
Figure 4.6: Ultraviolet-visible spectra of cobalt nanoparticles prepared by adding 200 ml with concentration (0.25 M) of cobalt salt in different molar ratio of NaOH; S10 (0.5 M), S11 (1.5 M), and S12 (2.5 M).	88
Figure 4.7: High-Resolution transmission electron microscopy images of gold nanoparticles prepared by adding 10 ml with concentration ($5.589 \times 10^{-3} M$) of gold salt to a different molar ratio of lemon extract S1 (4 ml), S2 (5 ml), and S3 (6 ml) and their Gaussian distribution particle size.	90

- Figure 4.8:** High-Resolution transmission electron microscopy images of silver nanoparticles prepared by adding 200 ml with a different molar ratio of silver salt; S4 (3 mM), S5 (4 mM), and S6 (5 mM) with 40 ml lemon extract and their Gaussian distribution particle size.92
- Figure 4.9:** High-Resolution transmission electron microscopy images of iron nanoparticles synthesized by adding a different molar ratio of iron salt (Fe^{3+} : Fe^{2+}) after drying; S7a (3.6 mM), S8a (4.6 mM), and S9a (5.6 mM) into 200 ml of prepared chitosan and their Gaussian histogram distribution particle size.95
- Figure 4.10:** High-Resolution transmission electron microscopy images of iron nanoparticles synthesized by adding a different molar ratio of iron salt (Fe^{3+} : Fe^{2+}) before drying; S7b (3.6 mM), S8b (4.6 mM), and S9b (5.6 mM) into 200 ml of prepared chitosan and their Gaussian histogram distribution particle size.97
- Figure 4.11:** High-Resolution transmission electron microscope images of cobalt nanoparticles prepared by adding 200 ml (0.25 M) of cobalt salt with a different molar ratio of NaOH; S10 (0.5 M) and its Gaussian distribution, S11 (1.5 M), and S12 (2.5 M).98
- Figure 4.12:** X-ray diffraction pattern for iron nanoparticles synthesized by adding a different molar ratio of iron salt (Fe^{3+} : Fe^{2+}); S7 (3.6 mM), S8 (4.6 mM), and S9 (5.6 mM) to 200 ml of prepared chitosan.101
- Figure 4.13:** X-ray diffraction pattern of cobalt nanoparticles prepared by adding 200 ml with concentration (0.25 M) of cobalt salt with a different molar ratio of NaOH; S10 (0.5 M), S11 (1.5 M), and S12 (2.5 M).....102
- Figure 4.14:** Chemical structure of lemon extract.103
- Figure 4.15:** Fourier transforms infrared spectroscopy (FTIR) of gold nanoparticles prepared by adding 10 ml with concentration ($5.589 \times 10^{-3} \text{ M}$) of gold salt with a different molar ratio of lemon extract; S1 (4 ml), S2 (5 ml), and S3 (6 ml).105

Figure 4.16: Fourier transforms infrared spectroscopy (FTIR) of synthesized silver nanoparticles by adding 200 ml with a different molar ratio of silver salt; S4 (3 mM), S5 (4 mM), and S6 (5 mM) with 40 ml lemon extract.	108
Figure 4.17: Fourier transforms infrared spectroscopy (FTIR) for iron nanoparticles synthesized by adding a different molar ratio of iron salt (Fe^{3+} : Fe^{2+}); S7 (3.6 mM), S8 (4.6 mM), and S9 (5.6 mM) to 200 ml of prepared chitosan.	111
Figure 4.18: Fourier transform infrared spectroscopy (FTIR) of synthesized cobalt nanoparticle by adding 200 ml with concentration (0.25 M) of cobalt salt with a different molar ratio of NaOH; S10 (0.5 M), S11 (1.5 M), and S12 (2.5 M).....	114
Figure 4.19: UV–Vis absorbance spectra of nickel salt solution with different concentrations.	116
Figure 4.20: Relationship between the absorbance intensity of nickel electronic transition bands with concentrations at 300 nm and 396 nm.	117
Figure 4.21: Illustration image of filter element including nano samples (AuNPs, AgNPs, FeNPs, or CoNPs).	118
Figure 4.22: UV–Vis absorbance spectra of Ni solution with different concentrations after passing through filter impregnated by gold nanoparticle size 28 nm.....	119
Figure 4.23: Relationship between the absorbance intensity values at 300 nm with change in nickel concentration before and after passing through an imbided filter with AuNPs 28 nm.....	119
Figure 4.24: Relationship between the absorbance intensity values at 396 nm with change in nickel concentration before and after passing through an imbided filter with AuNPs 28 nm.....	120

Figure 4.25: UV–Vis absorbance spectra of Ni solution with different concentrations after passing through filter impregnated by silver nanoparticle size 28 nm.....	121
Figure 4.26: Relationship between the absorbance intensity values at 300 nm with change in nickel concentration before and after passing through an imbided filter with AuNPs 28 nm.....	122
Figure 4.27: Relationship between the absorbance intensity values at 396 nm with change in nickel concentration before and after passing through an imbided filter with AgNPs 28 nm.....	122
Figure 4.28: UV–Vis absorbance spectra of Ni solution with different concentrations after passing through filter impregnated by iron nanoparticle size 18 nm.....	124
Figure 4.29: Relationship between the absorbance intensity values at 300 nm with change in nickel concentration before and after passing through an imbided filter with FeNPs 18 nm.....	124
Figure 4.30: Relationship between the absorbance intensity values at 396 nm with change in nickel concentration before and after passing through an imbided filter with FeNPs 18 nm.....	125
Figure 4.31: UV–Vis absorbance spectra of Ni solution with different concentrations after passing through filter impregnated by cobalt nanoparticle...	126
Figure 4.32: Relationship between the absorbance intensity values at near 300 nm with change in nickel concentration before and after passing through an imbided filter with CoNPs.	127
Figure 4.33: Relationship between the absorbance intensity values at near 396 nm with change in nickel concentration before and after passing through an imbided filter with CoNPs.	127

Figure 4.34: Relationship between the absorbance intensity of unfiltered and filtered Ni solution with some prepared nanoparticles samples at 300 nm electronic transition against concentrations.....129

Figure 4.35: Relationship between the absorbance intensity of unfiltered and filtered Ni solution with some prepared nanoparticles samples at 396 nm electronic transition against concentrations.....129

List of Tables

No.	Titles	Pages
	Table 2.1: Normal mode formula.....	53
	Table 3.1: Quantity of chemical reactant for gold nanoparticle preparation method (S1 – S3).....	62
	Table 3.2: Quantity of chemical reactant for silver nanoparticle preparation method (S4 – S6).....	64
	Table 3.3: Quantity of chemical reactant for iron preparation method (S7 – S9). 67	
	Table 3.4: Quantity of chemical reaction for cobalt preparation method (S10 – S12).....	69
	Table 4.1: Positions of FTIR absorption peaks and their assignment functional groups for gold nanoparticle capped by lemon extract samples (S1 – S3).....	106
	Table 4.2: Positions of FTIR absorption peaks and their assignment functional groups for silver nanoparticle capped by lemon extract samples (S4 – S6).....	109
	Table 4.3: Positions of FTIR absorption peaks and their assignment functional groups for iron nanoparticle capped by chitosan samples (S7 – S9).....	112
	Table 4.4: Positions of FTIR absorption peaks and their assignment functional groups for cobalt nanoparticle prepared at different concentrations of sodium hydroxide samples (S10 – S12).	115

Chapter 1

General Introduction

and

Literature Survey

Chapter 1

General Introduction and Literature Survey

1.1 Historical Overview of Nano

Nanotechnology could not have a specific determination era up till now. An early preoccupation history of nano and how nanoscience incorporated in the world around us started in 1959 when Richard P. Feynman (Nobel Prize in physics 1965) given his a popular talk Entitled, “*there is Plenty of Room at the Bottom*” at American Physical Society. This lecture described the controlling of particle and atom with its manipulating and dealing with small size problems [1, 2]. The first use of “Nanotechnology” invented in 1974 when Norio Taniguchi described the semiconductor processes in nanometer, “The nanotechnology concerned to separation, fusion, and reformation of the material by one atom or one molecule [2].

The implementation has begun with the National Nanotechnology Initiative (NNI) at California Institute of technology after President William J. Clinton gave a speech about the importance of nanoscale science and allotment in the first of the 21st century. Followed that, President George W. Bush said the 21st century is nanotechnology research and its improvement [1, 2].

Nowadays, the nanoscience revolution is getting progressively increase in modern centuries. Nanotechnology has variable research and studies about its concept, material fabrication, and application.

1.2 Definition of Nanometer Scale, Nanoscience, and Nanotechnology

Nanometer and Nanoscale: Word Nano is derived from the Greek Language nános (νάνος) that mean “dwarf” in English [3]. Nano is an SI prefix unit which used to denote a part of one-billionth of a meter, standard by multiplying 10^{-9} as a factor.

How big are one billion meters? It helps to put these numbers into perspective. The human hair width is approximately 40000-60000 nm, a diameter of human DNA is around 2-12 nm, and a single atom size is about several angstroms (0.1 nm) [4]. Therefore, one nanometer would be invisible to human eyes [5]. **Figure 1.1** illustrates the comparison between nanoscale with other scales.

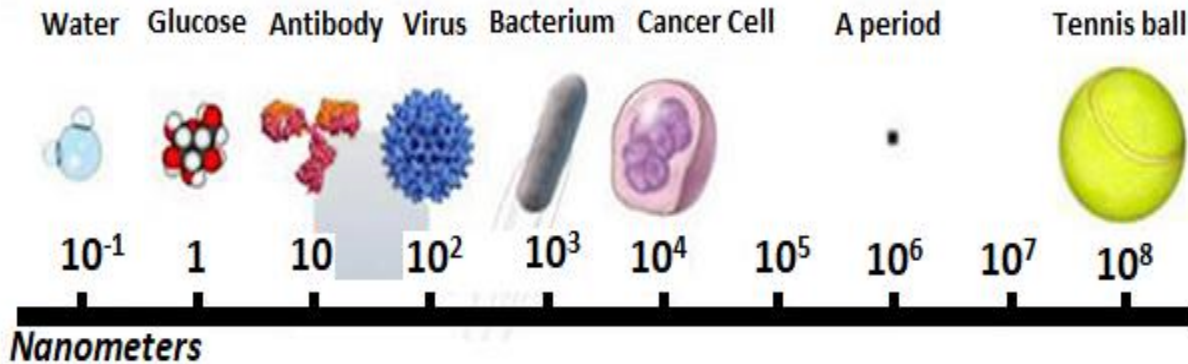


Figure 1.1: Comparison of the nanometer scale with other scales.

Nanoscience is a part of science that studies and deals with phenomena that occur at a small scale (nanometer) structure of atoms and molecules [4].

Nanotechnology is the technology that able to invent new material or instruments in the nanoscale range [6, 7] or enhance the ability of application or product [4]. The nano techniques have applied in the whole world from different fields such as physics, chemistry, biology, and engineering [7].

1.3 Classification of Nanomaterials Based on Dimensions

Nano-objects mostly categorized into four parameters: nanoparticle geometry, morphology, uniformity, and agglomeration [8]. According to nanoparticle geometry, nanomaterials were classified as a zero dimension (0-D), one dimension (1-D), two dimensions (2-D), and three dimensions (3-D).

1.3.1 Zero-Dimension (0-D) Nanomaterials

The total particulate in 0-D is in the nanometer range, which generally referred to as nanoparticle cluster and quantum dots [8] **Figure 1.2**. 0-D nanomaterials have a large surface area, which leads up to chemical and physical affect properties [9]. Various physical and chemical preparation techniques could be performed to control the shape, size, and structure of the particles in zero-dimensional materials. Physical synthesized including sputtering process, flame pyrolysis, laser ablation, and so on, while chemical route includes sol-gel and hydrothermal technique. Most important to note, the 0-D fabricated materials could agglomerate due to high surface energy in a physical approach, not withstand chemical routes [9].

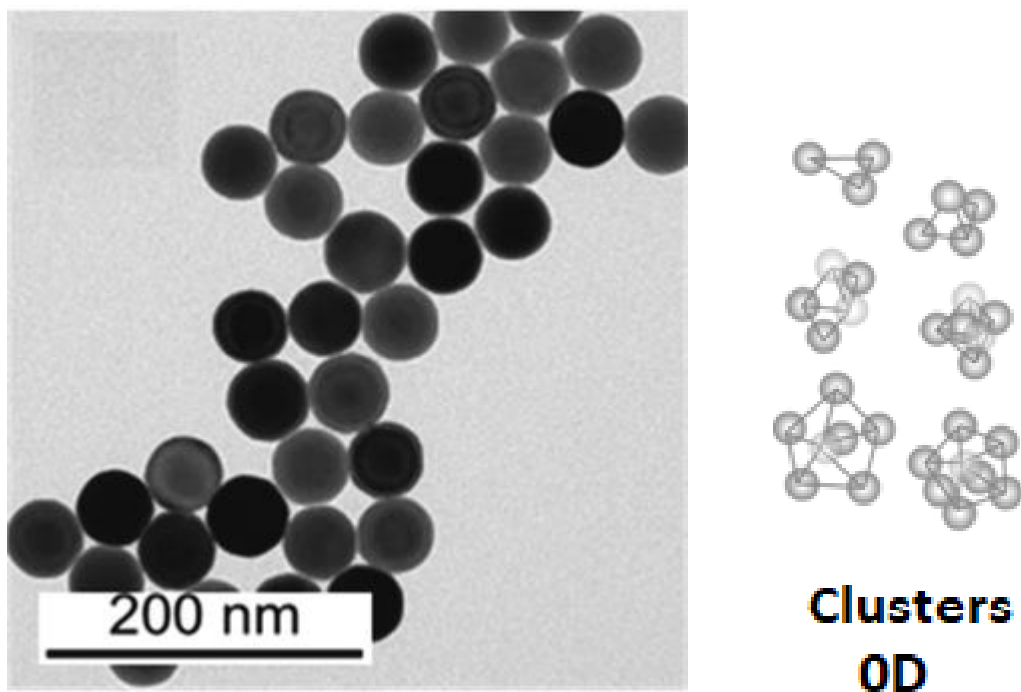


Figure 1.2: TEM of gold spherical nanoparticles and cluster in zero dimension [10].

1.3.2 One-Dimension (1-D) Nanomaterials

One-dimension nanoparticles have two-dimensions at the nanometer scale while the third dimension could exist at the microscale; this means that the confinements were done in two dimensions only. Nanotubes, nanowires, and nanofibers are an example of two-dimension nanomaterials [9, 11] **Figure 1.3**. One-dimensions have specified properties such as high tensile strength, magnificent adsorption, and a high degree contrast of displays [9]. Many physical and chemical methods can be used to prepare 1-D nanomaterials as thermal evaporation, sputtering techniques electrospinning, electrochemical deposition, electrochemical anodization, and lithographic, etc.[9].

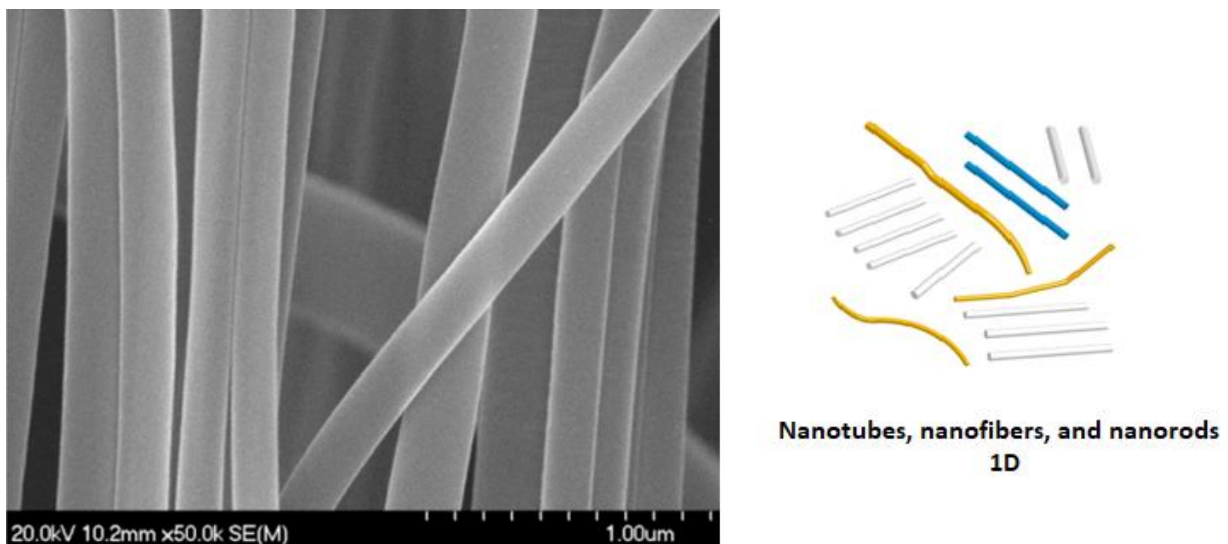


Figure 1.3: SEM of carbon nanofibers as an example of a 1-dimension of nanomaterials [12].

1.3.3 Two-Dimension (2-D) Nanomaterials

Two-dimension nanomaterials defined as a one-dimension of particulate at the nanoscale range; however, the other two dimensions in the microscale. These mean that the confinements were applied in one dimension. Thin-film coating,

nanosheet, and nanolayer are an example of two-dimension nanomaterials as [8, 9] **Figure 1.4**. A typical representation of the 2D fabricated method includes physical vapor deposition (PVD), chemical vapor deposition (CVD), dip-coating [9].

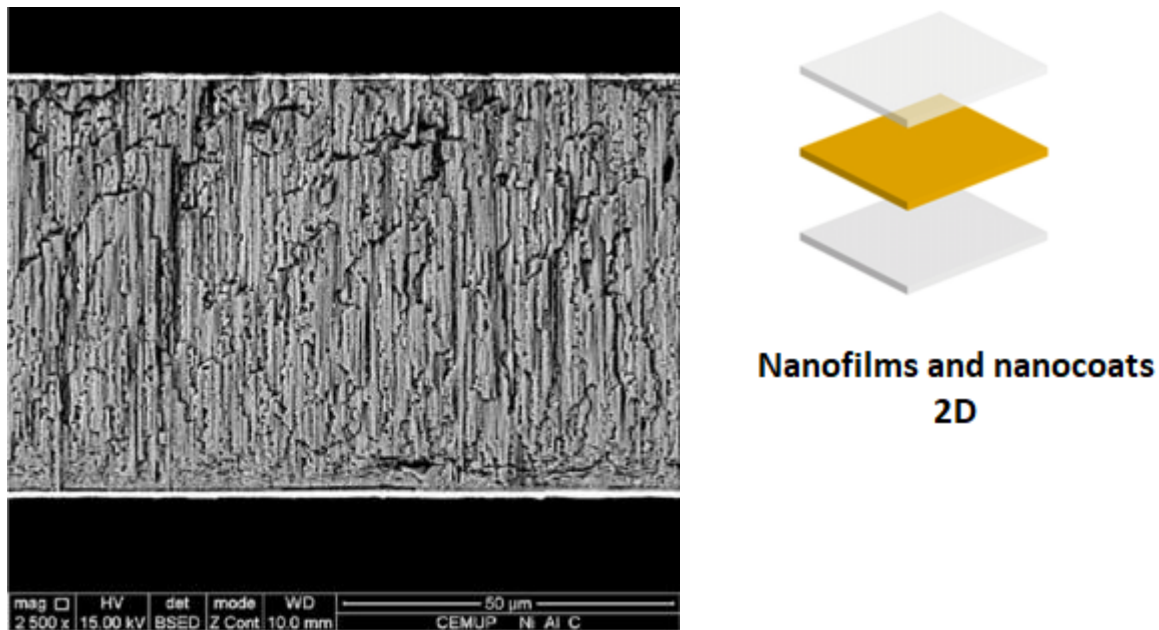


Figure 1.4: SEM of Ni/Al nanolayers as an example of 2-dimension nanomaterials [13].

1.3.4 Three-Dimension (3-D) Nanomaterials

The particulate is defined as all dimensions on the microscale range and no dimension in the nanoscale range, 3D nanomaterials are classified as material are not confined to the nanoscale level [9, 14]. The movement of electrons in this dimension is delocalized; in this case the electron moves within all dimensions [14]. Moreover, 3D nanomaterials can be containing the dispersion of 0D, 1D, or 2D [9]. The most common representation of three-dimension nanosystem is (bulk) polycrystals material [11] **Figure 1.5**.

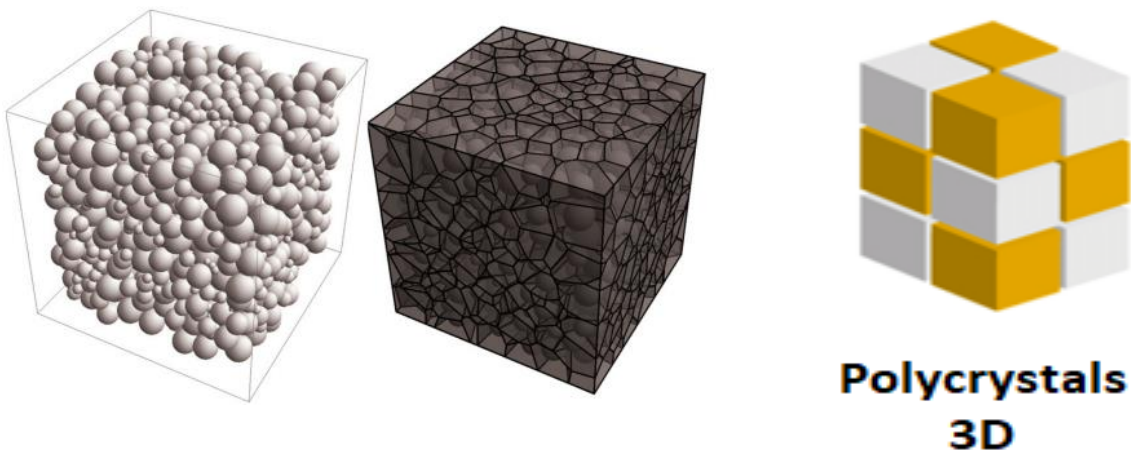


Figure 1.5: Bulk polycrystal structure as an example of 3-dimension nanomaterials [15].

1.4 Properties of Nanomaterials

1.4.1 Surface Energy of Nanomaterials

One of the main parameters of high interest with respect to nanoscale materials is that the massive variation of other larger-scale materials is a surface area to volume ratio. Surface area to volume ratio in nanosized material has a significant effect on in their catalytic properties because of the increase in the surface area allowed to molecules or atoms to overpopulated on the surface, and thus the energy of the surface will be growth [16]. A primary concern, the nanocrystal has a large surface area, which leads to performing more chemical reactions [16].

The surface area to volume ratio of the sphere nanoparticle with radius (r) which equivalent to the ratio $\frac{s}{v} = \frac{3}{r}$ mean, the surface energy was affected by the radius of the nanoparticle [6]. For instance, about 50 % of molecules located at the surface when the spherical nanoparticles have a size 3 nm while 20 % of atoms expressed the surface for the spherical nanoparticles have a 10 nm approximately.

Moreover, around 10% of molecules would be at the surface of the nanoparticle has 30 nm [16] **Figure 1.6**.

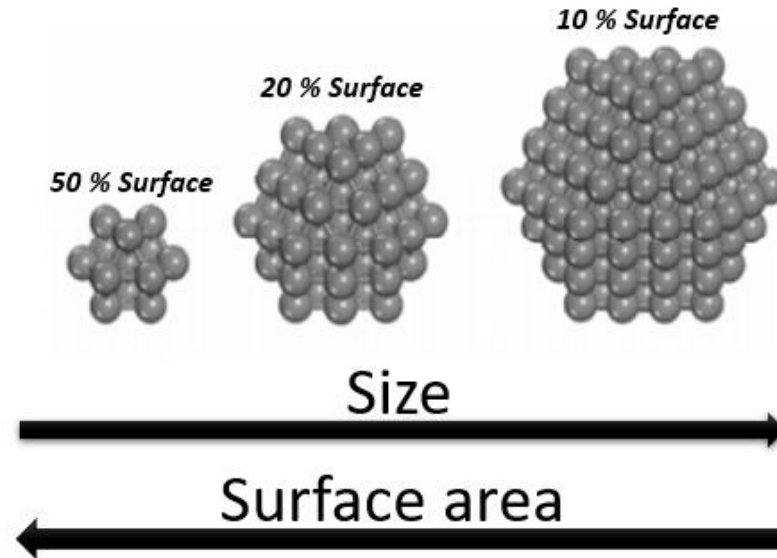


Figure 1.6: Schematic image explains the relation between surface area and particle size.

1.4.2 Quantum Size Effect of Nanomaterials

The optical properties of the semiconductor structure could make exciting differences in the same nanomaterial with different sizes because of its effect on the bandgap. These optical properties are related to electronic properties that depend on the number of atoms on the particle. The change occurs in electronic properties related to quantum mechanics effects [6].

There is no confinement for electrons and holes in a bulk semiconductor due to its continuous energy, where the energy level state is convergent. Highest occupied band (valence band) and lowest unoccupied band (conduction band) separated by the energy gap (E_g) [17] **Figure 1.7**.

The quantum size could be distinguished when the energy level between the two bands becomes excellent. The bands have discrete nature, and the wave function of nanostructure semiconductor of an electron is localized, e.g., quantum dot the entire bulk in semiconductor its electronic wave function is delocalized [6].

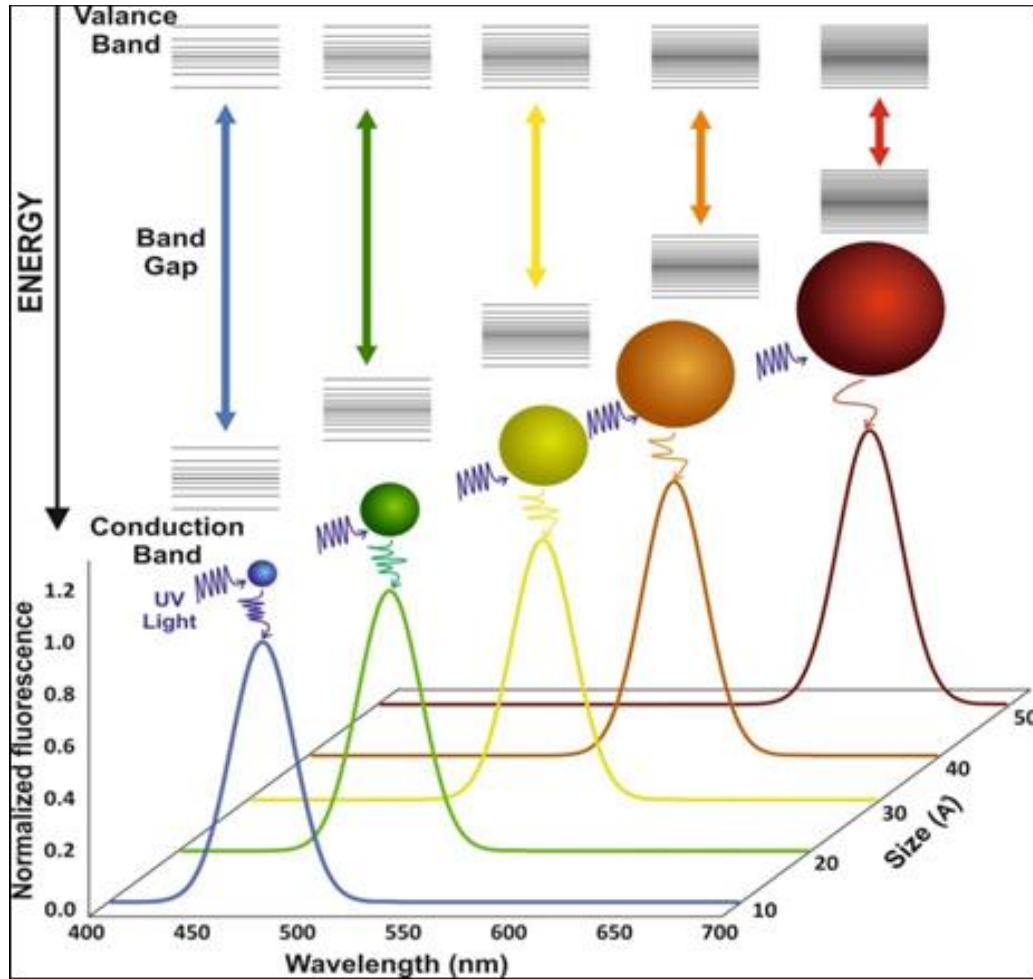


Figure 1.7: The comparison between particle size and energy gap [18].

Exciton in Nanoparticle is a consequence interaction between the promoted electron in the conduction band and left a hole behind in the valance band [19] **Figure 1.8**. A couple of electron-hole bond form attraction reaction such as a hydrogen atom, which has a separation in the middle denoted a Bohr's radius [17].

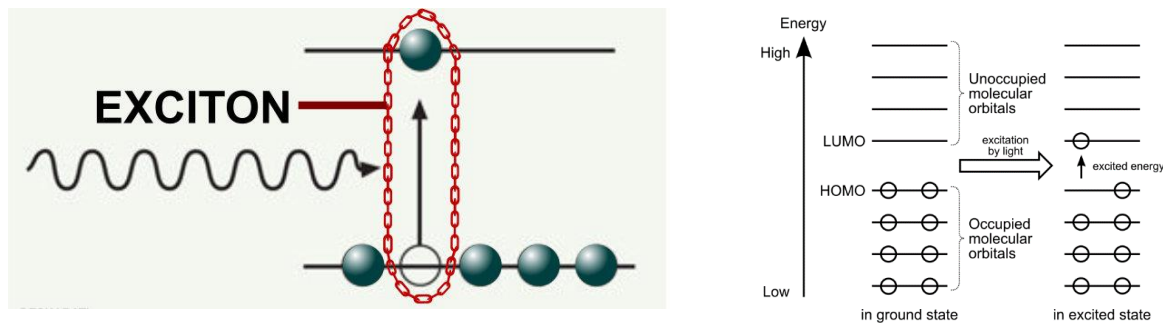


Figure 1.8: Schematic illustrate the exciton between (HOMO-LUMO) band gab.

1.4.3 Mechanical Properties of Nanomaterials

The mechanical properties aid a lot in the proper design of nanomaterials; hence of particle size decreases, the nanomaterial distinctive with large surface area to volume ratio [20]. The influence of increasing surface per volume, cause enormous alteration in crystal mechanical properties such as stress, strain, elastic modulus, hardness, adhesion, and friction [20, 21].

Stress is defined as the force per unit area of material, its expressed as

$$\sigma = F/A \quad (1.1)$$

Where the Greek litter sigma σ represents stress, F is the applied force, and A is a cross-section area of the object [14]. The unit of stress N/m^2 .

Strain the material responding to the acting force (tension or compression) alter length or volume. In other words, the rate change in length dimension to original length [14] is defined as the following equation

$$\varepsilon = \Delta L/L_0 \quad (1.2)$$

$$\varepsilon = \Delta V/V_0 \quad (1.3)$$

Where **Eq. (1.2)** act as a linear strain and **Eq. (1.3)** is volume strain Greek letter epsilon ε represents strain, L is the length, and V refers to volume [14].

Elasticity is the ability of materials to resist a distorting impact attempting to returns its original shape and size when the influence force removed. The relation between stress and strain denoted as elastic modulus [14]. Its shown in **Eq. (1.4)**

$$E = \sigma / \varepsilon \quad (1.4)$$

Where E refers to elastic modulus, and Greek letters σ and ε represent stress and strain, respectively. Moreover, stress is proportional to strain.

Hardness is the ability of materials to resist penetration or indentation in its shape and size [22].

Adhesion is the tendency of different particles or surfaces to bond or stick together. It also defined as the attraction force between substances that bring them into contact [23, 24].

Friction is the attractive force between two adhesive particles or surfaces, caused difficult movement to each other [24].

When the nanomaterial distinctive as hardness and strength, its flexibility will be decreasing follow that lowering in nano robustness comparing with conventional grain size. Briefly, the material's strength correspondingly increases with minimizing particle size [14].

An example in term of mechanical behavior would be changed in nanomaterial properties, the bulk material of copper element is ductile while the copper particles which have 50 nm are strength [25]. As a consequence of maximizing strengths and minimize ductility, copper nanoparticles with size (< 20

nm) are brittle. Through variation of stress and strain, the material could be classified into either brittle or ductile [14].

1.4.4 Magnetic Properties of Nanomaterials

Magnetism is a physical phenomenon that leads material to exchanges its behavior responding to the external magnetic field [14, 26]. The magnetic phenomenon is produced from particle movement by an effect on both electric charge and mass. A particle is referring to electrons, holes, and protons. In addition to its charge might be positive or negative ions. A magnetic dipole arises from the movement of the electric charge and separated by a small distance [27].

Magnetic nanoparticle could be classified into paramagnetic and diamagnetic due to its electron pair state [14].

Diamagnetic materials that have no unpaired electrons and the net of magnetic moment is zero in case no external field applied **Figure 1.9** while in case of an external magnetic field exist; it showed a very weak response it might repel magnetic field. Also, when the external magnetic field removed, the magnetization domain will lose; hence that, the diamagnetic materials could be classified as temporary magnetization [14, 26].



Figure 1.9: Schematic diagram illustrates the diamagnetic materials.

Paramagnetic, the material has unpaired electrons and has permanent magnetization domain, as shown in **Figure 1.10**. It has zero magnetic fields in the absence of an

external field, while in the exhibit of the external magnetic field, the net of the magnetic field increase, and it could be attractive [14, 26].



Figure 1.10: Schematic diagram illustrates the paramagnetic materials.

Superparamagnetic are the materials that have a magnetic form and appear insufficiently small domain number and particle size of ferromagnetic materials; it caused by the thermal energy of multi-domain particles under Curie temperature (the temperature above ferromagnetic substance loses its ferromagnetism and becomes paramagnetic) **Figure 1.11** [28, 29].



Figure 1.11: Schematic diagram illustrates the superparamagnetic materials.

Ferromagnetic the intrinsic materials that have natural magnetization properties even if the external magnetic field was absent. Moreover, the atomic magnetic moment configured in parallel domain **Figure 1.12** [14].

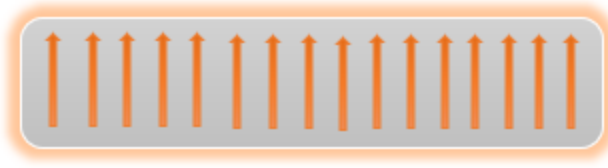


Figure 1.12: Schematic diagram illustrates the ferromagnetic materials.

Ferrimagnetic materials whose atoms or ions arranged as an antiparallel magnetic moment in the presence of external magnetic fields while in the absence case, the magnetization domain will be rearranged randomly and cancel out their magnetic field **Figure 1.13** [27].



Figure 1.13: Schematic diagram illustrates the ferrimagnetic materials.

Antiferromagnetic materials that have two different atoms, these atoms are equal in magnitude and configured in antiparallel direction. Due to that, it has zero magnetic moment **Figure 1.14** [26].

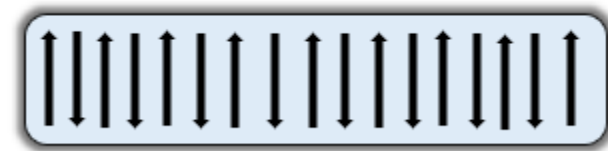


Figure 1.14: Schematic diagram illustrates the antiferromagnetic materials.

The magnetic behavior size specified by the structure domain of magnetic materials. To be more specified, the single domain appears at ferromagnetic material by decreasing size under critical point. Especially important, a small ferromagnetic particle has uniform magnetization at a lower state of free energy. In contrast, the large particles have non-uniform magnetization [27]. The critical size of the single domain might affect various parameters such as saturation value, surface value, surface energy, crystal anisotropy, and particle shape [27].

As the size of the magnetic nanoparticle decrease, the coercivity increase to a maximum value, thereby it would be drastically lower to zeroth **Figure 1.15**. Consequently, the particles become superparamagnetic. Magnetic nanoparticles are almost superparamagnetic because of their nanoscale size [27].

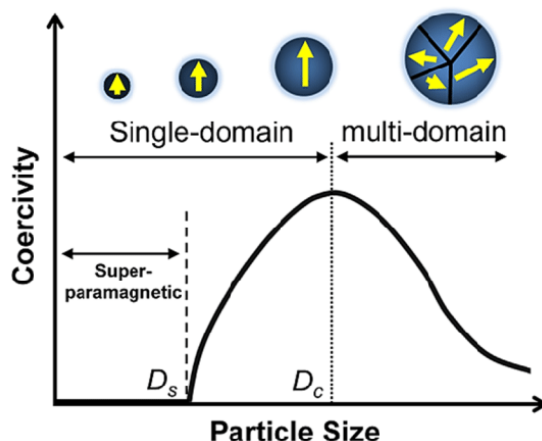


Figure 1.15: The size-dependent coercivity in a magnetic nanoparticle [30].

1.4.5 Optical Properties of Nanomaterials

The differences in energy between the highest occupied molecular orbital HOMO (valance band) and lowest unoccupied molecular orbital LUMO (conduction band) (HOMO-LUMO) the bandgap changed with changing the nanoparticle size in nanomaterials. These lead to a change in optical properties such as absorption,

emission transitions, and strength line between two bands. All physical and chemical properties in nanoscale materials could also be affected by changing its particle size [14, 25]. For instance, the gold element has a yellowish-brown color; however, this color could be changed at the nanoscale size; it has a deep red color when its crystal size has 20 nm. Otherwise, pure silver in bulk state is metallic gray, contrasting to yellowish-gray in nanoparticle [25].

The free particle movement determines via dimension of bulk material. Generally, the electronic density state can be affected by one or more-dimension material through that it could be confined. Hence, the quantum wells, quantum wires, and quantum dots would be obtained **Figure 1.16**. As an example of three-dimension materials is a bulk semiconductor where the density state is proportional to $(E - E_{C/V})^{1/2}$. Quantum well is two-dimension material confined the electron movement in 1D while quantum wire system is one dimension where the electrons are confined in 2D then the density of state is proportional to $(E - E_{C/V})^{-1/2}$. Eventually, an example of a zero-dimension domain is a quantum dot, where the motion of the electron is confined in 3D [17]. All the above can be affected by energy gap value, which directly changes in optical properties.

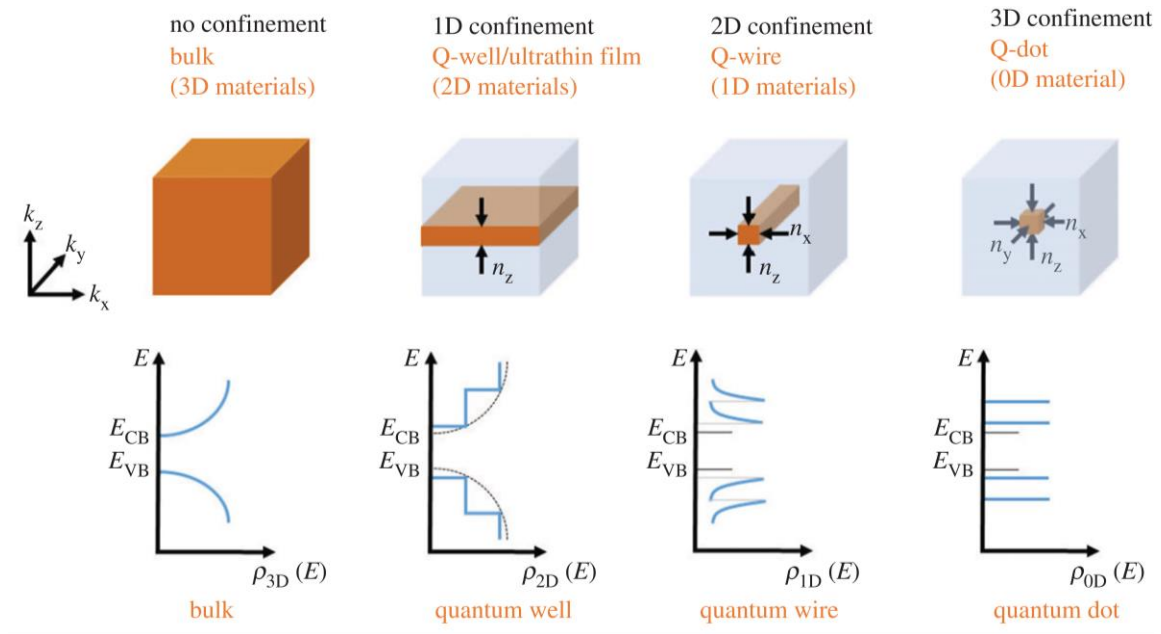


Figure 1.16: Schematic illustration of broken symmetry and functional form of the density of states in 1D, 2D, and 3D confined materials [31].

1.5 Preparation of Nanomaterials

The conventional fabrication method of nanostructures building material relies upon two types; the top-down approach and bottom-up approach **Figure 1.17** [1, 32].

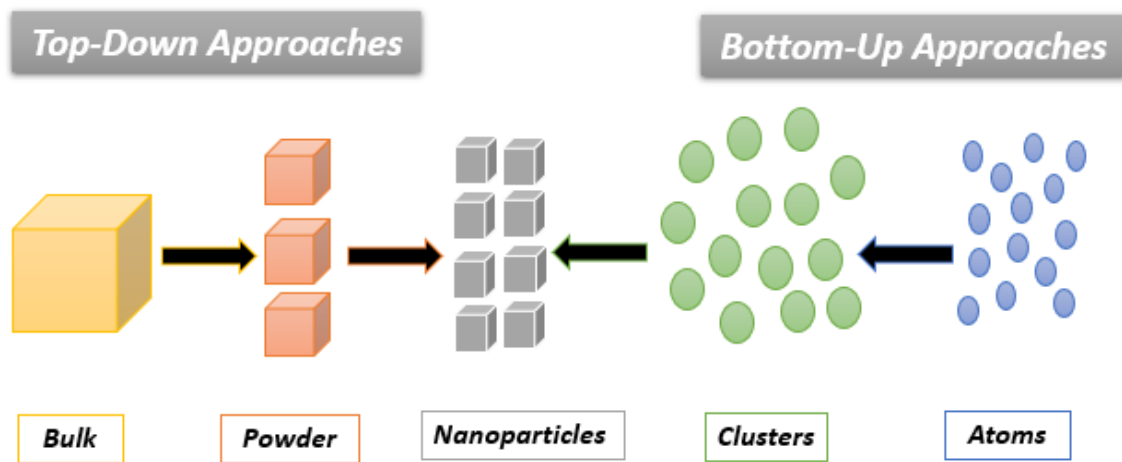


Figure 1.17: Schematic of nanoparticle Top-Down and Bottom-up approaches [33].

1.5.1 Top-Down Method

It is a physical approach that begins engineer bulk material structure to be tiny and extremely nanoscale, e.g., mechanical grinding (ball milling) technique [1, 34].

Ball Milling Technique is a cylindrical sealed container used to blend material into a small scale by using a variety size of the ball, the milling balls fabricated from stainless steel material, which used to crushing structure into more exceptional form [35] by mechanical corrosion **Figure 1.18**. Since the kinetic energy from grinding would transport to particles to perform reduction [34]. The ball milling technique used to produce nanoparticles [36].

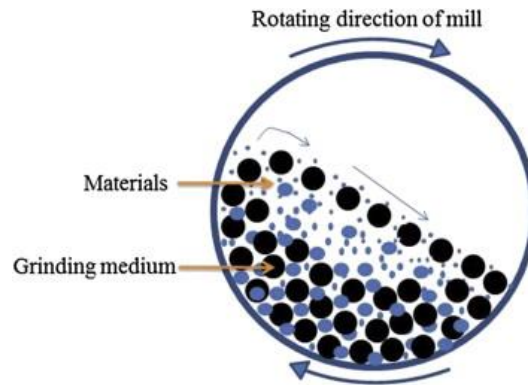


Figure 1.18: Schematic diagram of the ball milling technique [37].

1.5.2 Bottom-Up Method

Nanofabrication approach, which design component starting from atom, molecule, or cluster to be building up one by one, is producing nanoparticles. It would be a physical or chemical method according to its phase [34]. A **gas-phase route** which involves plasma arcing and chemical vapor deposition [34]. **Liquid-phase routes**, such as sol-gel and self-assembly [34].

Chemical Vapor Deposition is a process used to prepare a thin film with nanoparticle size by changing the phase of the chemical precursor into the vapor

phase by heating in the precursor of inert gas **Figure 1.19**. CVD produces high quality and high-performance thin-film e.g., carbon nanotube, metal, graphene, and diamond [38].

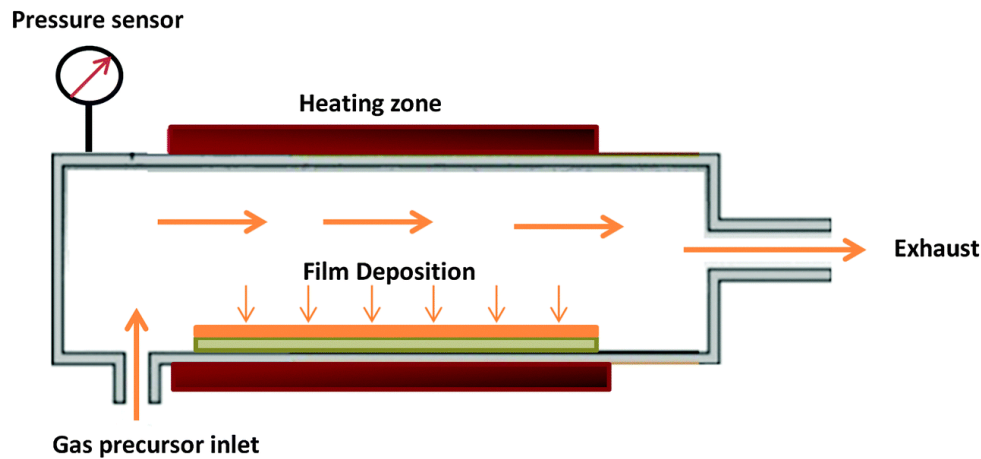


Figure 1.19: Schematic sketch of a chemical vapor deposition (CVD) system [39].

The sol-gel method is a process that uses high purified homogenous liquid precursors or organic polymer to obtain controlled nanoparticle structures in a different size. The colloidal pass through various chemical reactions involves hydrolysis, condensation, nucleation, finally, growth colloidal particles at typical conditions such as temperature, pH, and time **Figure 1.20** [40].

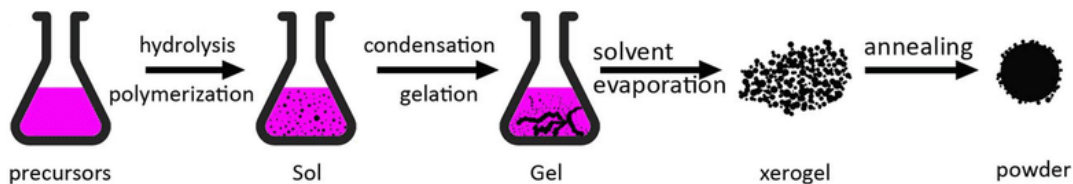


Figure 1.20: Diagram clarifies the mechanism of the Sol-Gel process [41].

Laser Ablation in this method, a laser beam with high frequency was performed to the target (solid material) in order to generate photoionization from heat energy.

Immediately, particles will volatilize as a fog, forming plasma then deposited into the substrate to compose thin-film **Figure 1.21** [42].

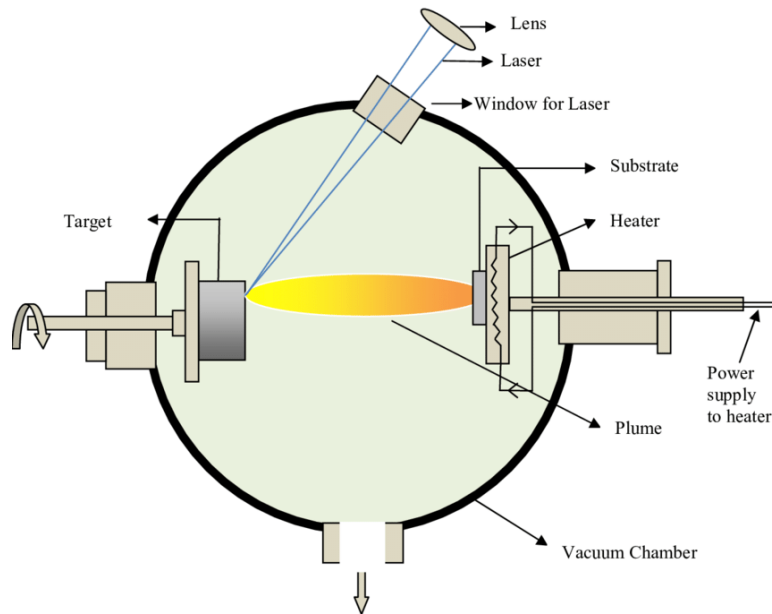


Figure 1.21: Schematic diagram of laser ablation technique [43].

1.5.3 Fabrication of Metal Nanoparticles

The noble metal nanoparticles open new attractive and possible research in various fields, as a result of their individual estimation and properties of utilization. Deposition from the gas phase or laser ablation is a physical approach, while the chemical reaction of liquids is distinguished as a chemical approach. Furthermore, there is another method of nanoparticle creation, which classified as a biological method that uses the microorganisms to produce metal nanoparticle [36].

The typical preparation of nanoparticles in a chemical method is using citrate as capping metal from different salts. Chemical synthesis colloidal particles would be described as spheroids regarding its ratio and size. The centrifugation must be used to separate the nanoparticles from the solvents and unlikable material, which leads to purifying the nanoparticles [36].

1.5.4 Fabrication of Magnetic Nanoparticles

Previously, the synthetic of the super magnetic relaxation was performed in Fe, Co, Ni by electrolysis using mercury cathode. In contrast, modern chemical methods have commonly used specially coating nanoparticles with different surfactants to prohibit agglomeration occurrence. Also, polymers based fabrication methods have been invented to synthesized coated and density uniform clusters of magnetic nanoparticles such as nanoflower [36].

Ferrite nanoparticles have been synthesized by thermal decomposition; its particle size could be diverse by varying the temperature of decomposition, for example, Nickle nanoparticle. While in Iron and Cobalt nanoparticle, the amorphous of the particle could be formed by thermal deposition. Another method could be used to prepare iron nanoparticles by exposing iron nitrides by ammonia at high temperatures. Also, NaBH_4 can be adding to the solution for the reduction of metal ions [36].

1.6 Applications of Nanotechnology

1.6.1 In Agriculture and Food

The nanomaterial becomes the most effective of daily life as a significant influence on sustainable agricultural product material. Nanotechnology contributes to enhancing the bioavailability of plants starting from food processing to the end of packaging performance. Including economic benefit, providing safety nutritive stodge, and high quality [44, 45]. The purpose of nanoscience in sustainable agriculture is to minimize diffuse chemical products and reduce nutrient absence in enrichment [46].

A primary concern of using agriculture nanotechnology implementation such as nano fertilizer and nano pesticides is trail product and nutrients standards to maximize advantages of a product without contamination of the soils, waters, and product the plant against insects and other diseases [46].

Nano-sensor is an alternative development that discovers the food component rapidly. Nanosensors associated with modern information and communication technologies provide a verity novel style for different components detection with high precision, divers type nanosensor evolved to obtain different obligations in food examination. For instance, carbon nanotube could be detected cations, anions, and organic components food [44].

1.6.2 In Medicine

Emerging nanotechnologies in the world encourage a medical strategy to be more modified in disease diagnosis and treatment, where the development indicates a novel method for healthcare [47, 48]. The pharmaceutical nanotechnology system could be segmented into two fundamental types, either nanomaterials or nanodevices. Nanomaterials are sub-classified into nanocrystalline and nanostructure; structured nanomaterial comprises nanoparticles, dendrimers, micelles, metallic nanoparticles, etc. [48].

Nanoparticles drug delivery system maintained by lipid polymer capsules to minimize distribution and dissolution, then its concentration is optimized in targeted tumor sites or specified cells [49, 50]. Cancer therapy performing by micelles and liposomes, which is another option for drug delivery agents, which are insoluble drugs due to their hydrophilic and hydrophobic nature, it could be used in magnetic resonance imaging to produce excellent tumor sites image [48].

As a matter of fact, the nanoparticle in medicine could be used in several cases. For instance, multifunctional nanoparticle (intravenous delivery), virus-based nanoparticles (affect as nanocarriers), lipid and polymer nanoparticle (strong effect response), magnetic and metallic nanoparticle (optimizing targeted drug delivery and detecting earlier stage of disease), aerosol dried powder (useful for inhalation pulmonary medication) eventually, smart nanomaterials (regulate via exterior stimulus). Nanotechnology would be used in surgery as flesh welder to weld artery with high accuracy [48, 51].

1.6.3 In Energy

Solar energy is one of the most remarkable types of renewable energy; it has been developed in nanotechnology for generating electricity and enhancing power efficiency [52, 53]. Applying specific nanoparticle layers to semiconductors (silicon plate), could improve the performance of the solar cell efficiency by converting sunlight absorption to electric power [52, 54].

1.6.4 In Water Remediation

Nanotechnology provides an innovative solution for water polluted problems in the environment and makes it suitable for human utilizing and consumption. Water desalination and purification using superior adsorption nanomaterial [55]. For example, graphene, carbon nanotubes, metal nanoparticle (e.g., silver, iron, and zinc), and magnetic-core (e.g., cobalt, nickel, and iron) [56]. These nanomaterials have the ability to treat water via densification wastewater from pathogens and remove heavy metals such as chromium, mercury, and cadmium [55, 57].

1.6.4.1 Filtration

It is a procedure to separate solid material from solution via allowing the solution to pass across pores medium [55]. Membrane filtration could be categorized into two types; either dead-end filter or cross-flow filter, the water in the dead-end filter has perpendicular flux so that all accumulation solid stuck to the membrane surface. On the other hand, the cross-flow filter flows the water in a parallel direction, which causes shear force. Most noteworthy is the flux in a cross-flow way is higher than the dead-end method [58].

1.6.4.2 Photocatalysis

A principle of heterogenous photocatalysis is a catalyst to attract UV or near UV from sunlight radiation [55]. Light absorbing leads to the transfer of an electron from the valance band to the conduction band [59]. The excitation would originate due to light radiation if the light energy were larger than the bandgap energy of materials [55].

As a consequence of photon absorbed adequate energy, the electron transfer from the valance band left a hole behind; this hole will drifting undersurface of the valance band. Major of charge carriers from photo generation involve redox reaction and submit to distract its blend compound in adsorbed molecules at photocatalysis surface follow that degrade detoxification organic and inorganic molecules [55]. The photo induces chemical reactions when semiconductor powder radiate at solid-liquid interference, this chemical reaction has the ability to degrade organic and inorganic molecules [58].

Nanomaterial photocatalysis has a large surface area to volume ratio, which permits to adsorb molecules [55]. A major development, photocatalysis with metal

oxide nanoparticles such as Titanium dioxide (TiO_2) and Zinc oxide (ZnO), is used to purified waste and effluent water; it also used to reduce air pollution [55].

1.7 Literature Survey

Y. J. Lee et al., (2019) used chitosan and green tea as stabilizing and reducing agent to synthesized gold nanoparticles capped with chitosan in 3 variant shapes (nanospheres, nanostars, and nanorods) using green tea extract as a reducing agent of gold salts UV visible spectra showed the Surface Plasmon Resonance (SPR) band of all three types. Lattice structures for all shapes of nano were confirmed in the high-resolution transmission electron microscope device. The three colloidal solutions of AuNPs were applied to cancer cell lines. The results following orders nanospheres, nanorods, and then nanostars, respectively. The green strategy with a designed shape of gold nanoparticles has an assistant in therapy application [60].

Parang and Moghadamnia (2019) synthesized silver-cobalt nanoparticles by chemical reaction; its effectiveness was proven in medicine application due to its anti-fungal properties [61].

Bhattacharjee et al., (2018) used a weed named *Alternanthera Philoxeroides* in eco-friendly to prepare gold nanoparticles. They used many techniques (UV, DLS, zeta potential, FTIR, EDAX, SEM, AFM) to characterize their sample. Synthesized green Au nanoparticles demonstrated significant results in spite of antimicrobial activity [62].

Choi et al., (2018) used the *Platycodon Grandiflorum* plant as a reducing agent in green preparation of gold and silver nanoparticles. Their result illustrated that AuNPs and AgNPs were prepared at 15nm and 18 nm, respectively. Both samples were face-centered cubic structure. The studies suggested a successful synthesis of green nanoparticle's versatile applications [63].

Alsammarraie et al., (2018) used *Turmeric powder* as a reducing and capping agent to prepare silver nanoparticles. AgNPs were characterized using UV, FTIR, TEM, and energy-dispersive x-ray spectroscopy (EDS). The highest absorption of UV monitored at 432 nm. TEM showed the spherical shape of particle size at 18 ± 0.5 nm. EDS used to detect the presence of the silver element. The process of preparing nanoparticles was environmentally compatible, and the synthesized AgNPs promising candidate for many agricultural applications [64].

Chandirika and Annadurai (2018) prepared AgNPs by treating silver ions with *Abutilon Indicum* extract. The as-formed silver nanoparticle was characterized by UV-Vis spectrophotometer, Fourier transforms infrared spectroscopy, scanning electron microscope, and used their prepared samples in antimicrobial studies. Through which known the radius of nanoparticles was defined with a range of 50-100 nm. The results of AgNPs were found as effectual and encouraging nanomaterial [65].

Kaur et al., (2018) used pomegranate peel to fabricate iron nanoparticle, iron-silver (FeO/AgNPs), and iron-gold (FeO/AuNPs) core-shell nanoparticles. The characteristic of surface Plasmon resonance peak was identified to be 465 nm for (FeO/AgNPs) and 530 nm for AuNPs. The electron microscope technique detected that the shell of silver encircled 13 nm, whether the gold shell was less than 100 nm. The activity of antibacterial and antifungal core-shell nanoparticles (CSNPs) ascertained by the inhabitation method and showed good results towards antibacterial activities. Hence, the as-prepared approach is a reasonable and cost-effective application for water purgation technology [66].

Muhy and Duman (2018) describe the synthetic of magnetic nanoparticles ($CoFe_2O_4$ NPs) using the coat of *Aesculus hippocastanum* plant

extract as a non-toxic and eco-friendly technique. Fabricated NPs were characterized by UV-Vis, DLS, XRD, FT-IR, SEM, and TGA. The results indicated that magnetic nanoparticles could be utilized in water removal and purification [67].

Kangama et al., (2018) applied chitosan with poly aluminum chloride and (Al (OH)₃+HCl) in the water flocculation process to remediate tap water and decrease its price. They found 96.38 % of muddiness, and more than 80.1 % of the aluminum was eliminated. More than anything else, it was as cost-effective treatment [68].

Diaz-Hernandez et al., (2018) prepared magnetic iron oxide nanoparticles using chitosan as warping material. They used transmission electron microscopy, Fourier transform spectroscopy, and X-Ray diffraction tools to characterize their products [69].

Kumar et al., (2017) used *Andean blackberry* extract as stabilizing agents and as reducing silver ions to prepare AgNPs. From the result, the plasmonic band and the crystallinity nature were discussed by UV and X-Ray. The author used prepared samples as a great potential drug against diseases [70].

Jayaprakash et al., (2017) used *Tamarind fruit* extract as reducing and capping under microwave irradiation as eco-friendly synthetic to prepare AgNPs. The formation shape, stabilization, and particle size were performed using various analytical instruments. The prepared silver nanoparticle was studied against antibacterial activity [71].

Raja et al., (2017) Synthesized silver nanoparticles using *Calliandra haematocephala*, as a reducing after that characterized prepared sample by UV, X-ray diffraction analysis, and Zeta potential. The prepared samples were applied in therapeutic applications against antibacterial activities [72]

Alymov et al., (2017) prepared different sizes of iron nanoparticles by reducing the iron hydroxide layer in flowing hydrogen then passivated in argon. A systematic characterization of FeNPs was performed using X-Ray diffraction analysis [73].

Ansari et al., (2017) used the hydrothermal method to synthesized cobalt nanoparticles; oleic acid was used as a capping agent. They used X-Ray diffraction, Raman spectroscopy, and Infrared spectroscopic studies to characterize CoNPs. They investigate that CoNPs contains the ferromagnetic parameter. Further, the temperature depends on magnetic parameters, saturation, permanent coercivity, and reduced permanent magnetization were specified with CoNPs. Above all, prepared samples suggested high effective against cancer cells and the human bloodstream [74].

Devath et al., (2016) used iron nanoparticles in domestic wastewater treating. The authors used UV-Vis spectroscopy to determine the peak of surface Plasmon for FeNPs. It also characterized by a microscope technique to detect the presence of iron nanoparticles [75].

K. Lee et al., (2015) synthesized spherical, triangular, and hexagonal shapes with 23nm diameter gold nanoparticle using *Inonotus Obliquus* extract at room temperature. Synthesized samples exhibited good results against antibacterial, antioxidation, and cytotoxicity against human breast and stomach cancer cell lines [76].

Patra and Baek (2015) prepared AuNPs using a *melon peel*. They used different techniques like UV, SEM, XRD, FTIR, and thermogravimetric analysis to characterize their prepared samples. Surface Plasmon Resonance was at 560nm. Their result showed that the samples were prepared as spherical nanoparticles with

different sizes (20-140 nm). Besides, they used a melon and rind as stabilizer and surfactant agents. The sample was used as a potential antibacterial activity [77].

Ibrahim (2015) prepared AgNPs with environmentally, friendly, and cost-effective approaches using *banana peel extract* (BPE). BPE used as reducing and capping agents for silver salt. Thereafter, silver nanoparticles were characterized by different techniques such as UV, X-Ray, SEM, TEM, and FTIR. The as-prepared silver nanoparticles assist in inhibiting the growth of bacteria [78].

Abdollahi et al., (2015) synthesized chitosan-coated with Fe_3O_4 nanoparticles and used to purify water by minimizing arsenic concentration. The prepared sample was characterized by transmission electron microscopy, Fourier transforms infrared and vibrating sample magnetometer. They cofired that, prepared samples could implement to turbidity water in order to adsorb arsenic, follow that, applying a magnetic field to separate materials [79].

Salman et al., (2014) prepared magnetic cobalt nanoparticles with spherical shape and 400 nm of the diameter by liquid-phase reduction method using hydrazine. They investigated that; dendritic nanoparticles were created at 298 K when the concentration of hydrazine decrease — moreover, large dendritic nanoparticles formed at a 353 K [80].

Zola et al., (2014) utilized different methods to prepare cobalt nanoparticles; the first one is reducing cobalt salt by polyalcohol; the second method is demonstrated by decomposition, an organometallic, and eventually reduce metallic salt by borohydride. They confirmed that the nanoparticles' shape and size distribution would be changed with varying preparation methods [81].

Li et al., (2014) used magnetic chitosan and graphene oxide- ionic liquid to enhance the treatment and remove heavy metal ion as chromium Cr (VI) from

wastewater. Most important, they demonstrated their work by Fourier transform infrared, scanning electron microscopy, and X-Ray diffraction [82].

Sujitha and Kannan (2013) synthesized gold nanoparticles by reducing HAuCl₄ using *Citrus Limon*, *Citrus reticulata*, and *Citrus sinensis* juice extract as a surfactant and stabilizer. The synthetic samples characterized using different spectroscopic techniques like UV, TEM, and XRD. TEM studies offered different shapes with small sizes for particles while Dynamic Light Scattering (DLS) graph sized display larger particle comparing with TEM. In this research, the effectiveness of gold nanoparticles and its biological application [83].

Jayaseelan et al., (2013) synthesized AuNPs using *Abelmoschus esculentus* seeds. And configured these samples using UV, XRD, FTIR, AFM, FESEM, and EDX were analyzed. As a result of characterization, all particles have a spherical shape, and it is the size in the range 45-75nm. The fungus area has been identified and applied to Gold nanoparticles, an effective anti-fungal of the prepared samples was studied [84].

Logeswari et al., (2013) *Solanum Tricobatum*, *Syzygium Cumini*, *Centella Asiatica*, and *Citrus sinensis* used to synthesize green silver nanoparticles. They used many techniques, such as UV, XRD, AFM, and FTIR devise. The result of mediated was 53, 41, and 52 nm, corresponding to *Solanum Tricobatum*, *Syzygium Cumini*, *Centella Asiatica*, and *Citrus sinensis*, respectively [85].

Prathna et al., (2011) used a rapid and straightforward method to synthesized silver nanoparticles using the extract of *Citrus Limon*. The samples were identification by UV, X-Ray Diffractometer (XRD), and Fourier transform infrared (FTIR) spectroscopy. The results obtained the *Citrus Limon* were used as a capping and reducing agent. FTIR revealed the involvement of bioactive compounds from

Citrus Limon in capping and stabilization of AgNPs. TEM showed the formation of a spherical shape under 50 nm [86].

Bankar et al., (2010) used *banana peel extract* (BPE) as a green strategy for preparation gold nanoparticles. It was boiled, mashed, rinsed with acetone, and then dried. Peel powder was used to reduce chloroauric acid. Different nanoparticles were formed when the conditions of the interaction changed with respect to consideration of PH and chloroauric acid, components of PBE, and temperature duration. Their preparing sample was characterized using several techniques, including UV, SEM, X-Ray, and FTIR. Samples had efficacy against antimicrobial activity to most fungi and bacteria [87].

1.8 Aims of the Thesis

- 1- Preparation of some magnetic, noble metal with different nanoparticles sizes and shapes such as (Ag, Au, Fe, and Co) using different chemical methods.
- 2- Ultraviolet-visible spectroscopy (UV-VIS) will be employed to investigate surface plasmon band and their position dependence on the particle sizes of the synthesized samples.
- 3- Study the size distribution and morphology of the prepared samples using high resolution transmission electron microscope (HR-TEM), and the particle size will be estimated from TEM images.
- 4- The crystallinity of prepared samples will be studying using x-ray diffraction pattern (XRD) as well as the average crystalline size of nanoparticles will be calculated.

- 5- Fourier transform infrared spectroscopy (FTIR) will be used to study the chemical interaction between nanoparticles and functional groups of surfactant materials.
- 6- Due to the high reactivity and strong sorption of nanoparticles, the prepared samples will be used to decrease nickel concentrations in water and the effect of the particle's sizes, shapes on changing nickel concentrations will be explaining.

Chapter 2

Theoretical

Consideration

Chapter 2

Theoretical Consideration

2.1 Introduction of Light Radiation

2.1.1 Electromagnetic (EM) Radiation

It is a form of energy produced by oscillating both electric and magnetic waves perpendicular to each other, traveling in packets of energy called photons, as shown in **Figure 2.1**. The energy of the electromagnetic spectrum could be varying according to the wavelength and frequency of the ray diagram presented in **Figure 2.2** [88].

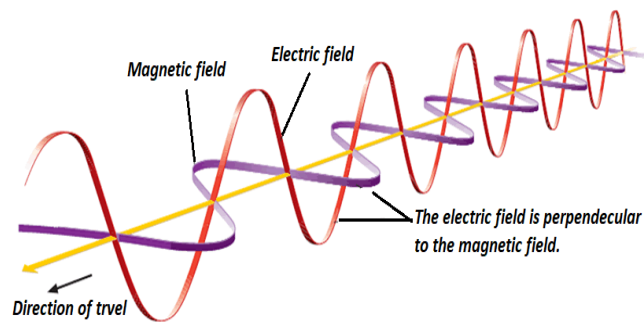


Figure 2.1: Plane of electromagnetic wave.

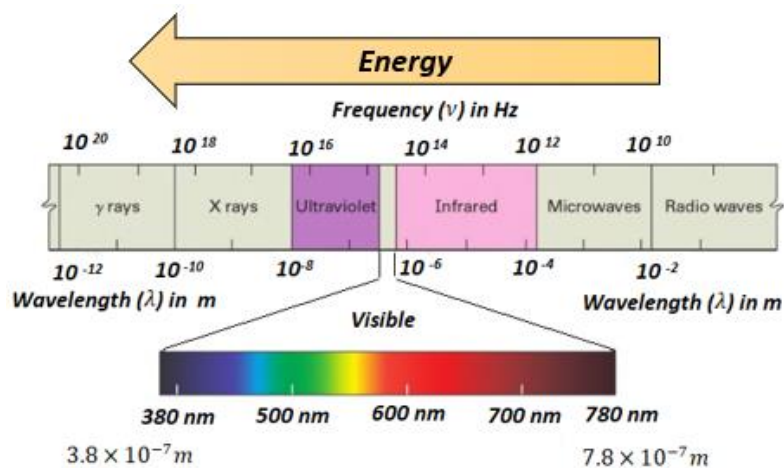


Figure 2.2: Illustration of visible radiation in electromagnetic spectrum [89].

The applied light characterized by wavelength λ , which is known as the distance between two peaks of the wave. The energy of photon relevant to the wavelength given by the following Equation

$$E = h\nu = \frac{hc}{\lambda} \quad (2.1)$$

Where h is known as *Plank's constant* and estimated by ($6.62 \times 10^{-34} J \cdot s$), ν is frequency, while c refers to the velocity of electromagnetic radiation ($3 \times 10^8 m/s$), and λ is the wavelength of light [89, 90].

The Plank's equation state as the energy of the photon is directly proportional to frequency and inversely proportional to its wavelength. To be specified, high frequencies with shorter wavelengths coincide with high-energy radiation, for example, gamma rays. In contrast, low frequencies with longer wavelengths correspond to low-energy radiation, such as radio waves, as illustrate in **Figure 2.3** [89].

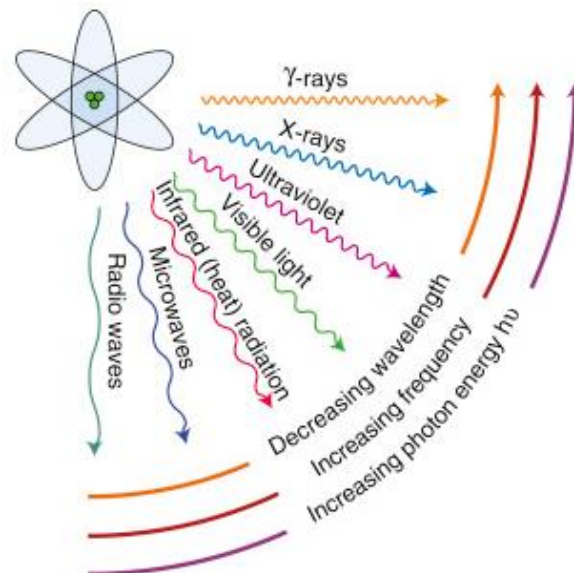


Figure 2.3: Illustration represents the comparison between electromagnetic rays

[88].

2.2 UV-Visible Spectroscopy

2.2.1 The Concept of UV-Visible Spectrometer

When electromagnetic beam radiation-exposed through materials, it would interact gathering, this interaction with light case several methods of operation; absorption, transmission, reflection, and scattering, as illustrated in **Figure 2.4**.

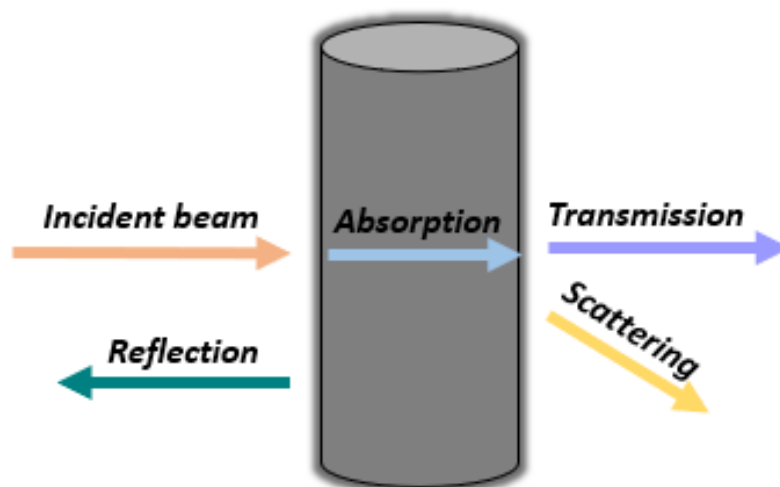


Figure 2.4: Schematic sketch for interaction light with matter.

In the case of measuring the UV-visible spectrum, the absorbance of light could characterize. The wavelength range of UV-vis spectroscopy light is 190-800 nm, related to (190-400 nm) for ultraviolet (UV) range and (400-800 nm) for the visible light region. Both ultraviolet and visible spectroscopy almost utilized for analysis techniques in the purpose of estimate the chemical structure compound, and it can use to study the electronic transition of the molecule [90, 91].

The incident light (photon) consists amount of energy; this energy transferred from electromagnetic waves to the molecule by striking them, which lead molecule to absorb radiation. The absorption obtained when the particular condition achieved,

which is the energy of an incident photon and the energy difference ΔE between allowed states equalized, as illustrated in **Figure 2.5** [89].

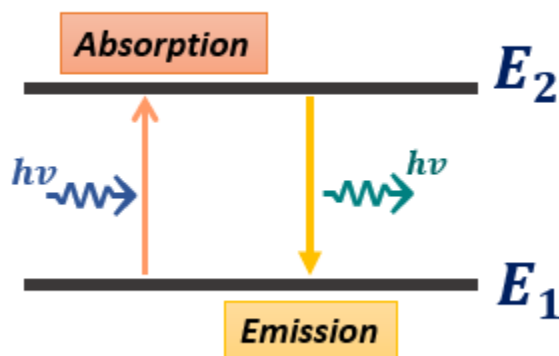


Figure 2.5: Illustration of optical phenomena for absorbance and emission.

The light absorption occurs during the energy of photons are promote the electron from low energy states to a higher state. The capability of the molecule to absorb light as a function of wavelength expressed by the UV-visible spectrum is depended on the molecular structure of the element. The absorbing of structure element and functional groups determine the chromophores, d-d, and f-f transition [89].

2.2.2 The Absorption and Beer-Lambert's Law

The absorbance law is given by

$$A = \log_{10} \left(\frac{1}{T} \right) \quad (2.2)$$

Where A represent the absorbance and T is the transmittance of light equal $T = \left(\frac{I}{I_0} \right)$, I_0 is the intensity of the incident beam, I is the intensity of the transmitted beam **Figure 2.6**.

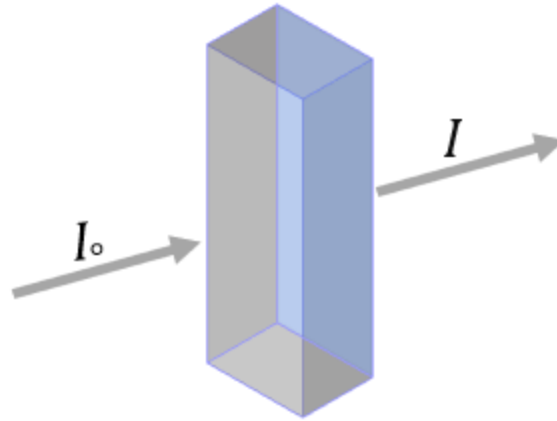


Figure 2.6: Schematic illustrates incident and transmitted intensity in Beer Lambert's Laws.

UV and visible light absorption described by involved both the laws of Lambert and Beer together. According to the law of Lambert's, the absorbance of the sample is directly proportional to the path of light [90], which is represented by the following equation

$$A = \log_{10} \left(\frac{I_0}{I} \right) \propto l \quad (2.3)$$

$$A \propto l \quad (2.4)$$

$$A = \varepsilon l \quad (2.5)$$

Where the Greek letter ε refers to the molar decadic extinction coefficient, and l is the path length.

After a while, Beer discovered his law which states as; the amount of absorbed light is proportional to the concentration of the samples [90], expressed as

$$A = \log_{10} \left(\frac{I_0}{I} \right) \propto c \quad (2.6)$$

$$A \propto c \quad (2.7)$$

$$A = \epsilon c \quad (2.8)$$

These two laws combined into what often referred Beer-Lambert law defined as when a beam of monochromatic radiation passed through the absorbing medium, then the decrease in intensity proportional to the thickness (pathlength) as well as the concentration of the solution [90, 92, 93], the mathematical expression obeys to the following equation

$$A = \log_{10} \left(\frac{I_0}{I} \right) = \epsilon c l \quad (2.9)$$

Where c is the concentration of absorbing species.

Important to note, the Lambert-Beer's law is valid only in case the incident - beam is monochromatic light (the radiation possess just one wavelength) [90, 92].

2.2.3 Theory of Ultraviolet-Visible Electronic Spectroscopy

The ultraviolet and visible spectrum of the molecule consists of one or more bands. These bands display the absorbing of molecule radiation over a range of wavelengths. The reason for these bands is an electronic level transition, usually accompanied by a simultaneous change between the numerous vibrational ultraviolet-visible levels. Furthermore, each vibrational level associated with electronic states also has a large number of rotational levels associated with it, as shown in **Figure 2.7** [92]. These processes quantified as

$$E_{total} = E_{electronic} + E_{vibrational} + E_{rotational} \quad (2.10)$$

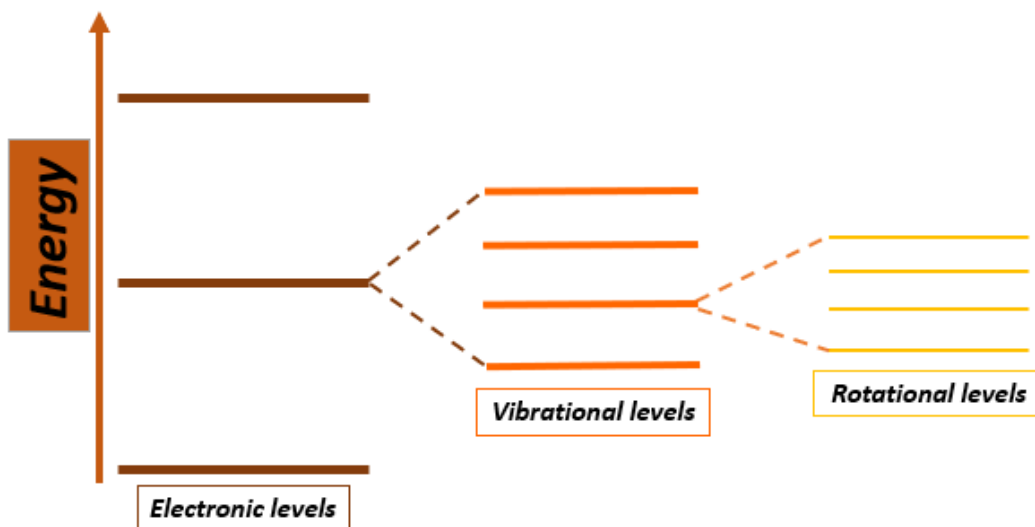


Figure 2.7: Electronic transitions and UV-Visible spectra in molecules.

The type of electronic transition depends on the available electrons and the energy of the photons, as illustrated in **Figure 2.8**.

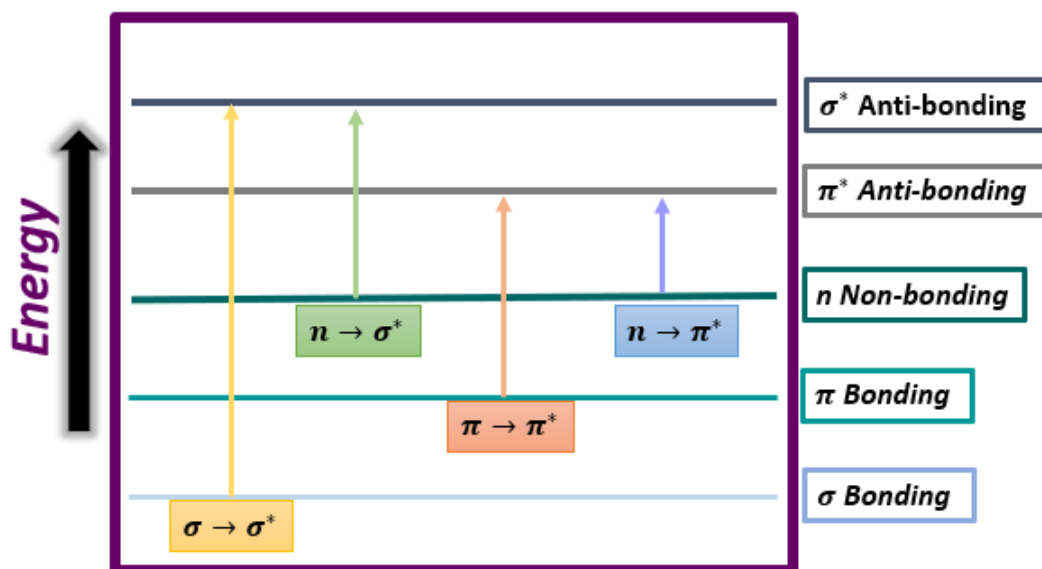


Figure 2.8: Relative energies of molecular orbital and transitions between them.

$\sigma \rightarrow \sigma^*$ transition: it is mean the electron can be excited from the orbital ground state (σ) bonding to the excited orbital state (σ^*) antibonding it is required the highest energy process since (σ) bond is tight. The absorption occurs in saturated

hydrocarbons, e.g., methane and propane. Moreover, this kind of transition demands a short wavelength, which is high energy [93].

$n \rightarrow \sigma^*$ transition: this type of transition occurs in saturated compounds containing atoms with lone pairs of electrons like alcohols and amines. Besides, the $n \rightarrow \sigma^*$ transition requires less energy than $\sigma \rightarrow \sigma^*$ transition [93].

$\pi \rightarrow \pi^*$ transition: it is corresponding to the electron can be excited from the bonding (π) to the antibonding orbital (π^*). With this in mind, (π) electron excitation required low energy than (σ), which means a long wavelength. To be specific, this type of excitation takes place in unsaturated compounds that consist of multiple bonds such as alkenes and alkynes [93].

$n \rightarrow \pi^*$ transition: means an electron excited from non-bonding orbital to antibonding orbital (π^*). This type of transition occurs in unsaturated compounds that consist of unshared pair electron as heteroatoms. Also, the $n \rightarrow \pi^*$ transition demands the least amount of energy and shows absorption at a longer wavelength, and an example of this kind is carbonyl compounds [93].

2.3 Transmission Electron Microscopy (TEM)

The transmission electron microscope technique used throughout the world to investigate the nanomaterial and an atomic world that it could hardly imagine, its image allows viewing atomic level and texture of element, including information about surface feature, shape, and size. A significant factor, the TEM offers the most powerful magnification, potentially over one million times or more. Despite that, it required special housing due to vacuum sensitively to vibrations and electromagnetic fields [94]. High-resolution transmission electron microscope HR-TEM provides

information about nanoparticle morphology and topography in two or three dimensions; it also illuminates the softness and hardness of materials [60].

2.3.1 The Principle of Transmission Electron Microscope Technique

Electron microscopy begins with employ a high voltage commonly (100 – 200 kV) of the electron beam, which leads a current of particles to accelerate the electrons beam to travel with a high speed through the microscope's vacuum tube. The beam of electrons passes through electromagnetic objective lenses with specific focal length; to guide and focus the electron beam to move smoothly and very thin beam towards the specimen (copper grade); which contain the sample on their surface [94, 95].

The electron beam either scattered, absorption, or transmitted after passing a beam over the specimen, transmitted of electron beam hit a fluorescent screen at the bottom of a microscope producing high-resolution image according to the density of the sample as shadow image of the specimen. Especially relevant, the image can be studied directly by the operator and capture the photos [94, 95]. Anode will give the electron beam with a higher speed and smaller de Broglie wavelength. It results in higher resolving power and image on screen [90].

The most important parameter of an optical microscope is magnification and resolution — the magnification of an optical microscope provided by the magnification power of objective also by the ocular lens system. Equally important, the resolution of an optical microscope, which defined as the shortest distance between two objects on a specimen that can be clearly distinguished by observer or camera as two discrete points. The highest magnification is worthless if the resolution is unsatisfied [90].

Ernst Abbe postulated that the best resolution R obtained with an optical microscope is limited by the wavelength λ of photons (400 – 700 nm) that used to probe of the sample and numerical aperture of the system NA is given by

$$R = \frac{\lambda}{2n \cdot \sin \theta} = \frac{\lambda}{2 \cdot NA} \quad (2.11)$$

Where n refers to the refractive index of the space between an objective lens and sample, and θ is the half opening angle of the objective [90].

Overall, resolving power of the optical microscope increase with increasing the refractive index value n ; this is the reason why oil immersion microscopes used to achieve high resolving power. Moreover, the lower wavelength can have higher resolving power, vice versa [90].

The electron gun displayed electron (charged particle) as tiny balls move through space, as well as the electrons have wave properties; the relationship between both expressions denoted as de Broglie wavelength of the particle

$$\lambda = \frac{h}{p} = \frac{h}{mv} \quad (2.12)$$

Where h is plank's constant, p is the momentum of the electron [95].

An electron's momentum usually defined by falling through a potential difference

$$eV = \frac{1}{2}mv^2 \quad (2.13)$$

e is the electronic charge in volts (1 electron volt = $1.602 \times 10^{-19}J$), therefor

$$\lambda = \frac{h}{\sqrt{2m_0eV}} \quad (2.14)$$

Due to the high acceleration voltage in TEM, relativistic effects have to be taken into account [95]

$$\lambda = \frac{h}{\sqrt{2m_0eV(1+\frac{eV}{2m_0c^2})}} \quad (2.15)$$

The electron beam generated at an electron gun of (TEM) by thermionic emission. An electron gun emits thermoelectrics from the tip of the cathode by heating tungsten filament or lanthanum hexaboride (LaB₆). The emitted electrons from the cathode accelerated in an electric field towards a circle-shaped anode operated at zero potential, as shown in **Figure 2.9** [90, 95]. When the work function denoted as φ , the current density at the surface expressed by Richardson Equation

$$j = AT^2 \exp\left(\frac{-\varphi}{K_B T}\right) \quad (2.16)$$

Where A is the emission constant, T is the temperature of the material in Kelvin, and K_B represent Boltzmann constant ($1.38 \times 10^{-23} \text{ J/K}$). This process occurs because the thermal energy overcomes higher than the work function [90, 95].

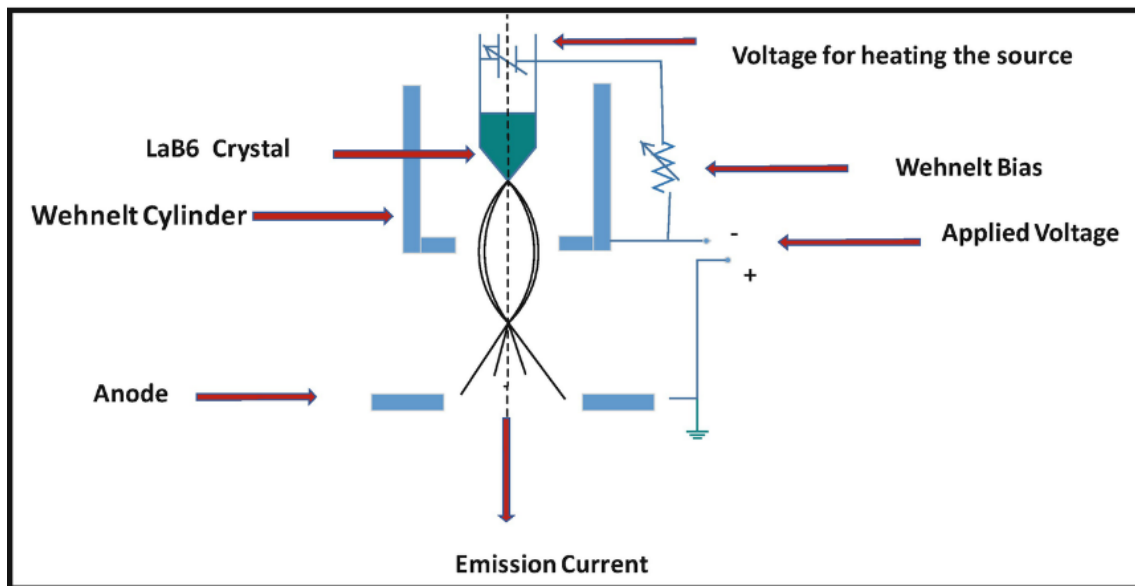


Figure 2.9: Illustration of an electron gun and cathode connection in a microscope [96].

2.4 Theory of X-Ray Diffraction

X-rays diffraction were firstly discovered in 1895 by German scientist Wilhelm Rontgen. It defined as a part of the electromagnetic spectrum that can pass through the sample its wavelength range between (0.01-10 nm). X-radiation could penetrate the materials according to their density. A distinctive quality of the mentioned radiation is possessed extremely short wavelength with high frequency [90, 97].

Single-crystal x-ray diffraction methods are the most commonly used technique for analytical utilities. It provides information about molecular structure; hence that, it could provide a direct determination of crystalline lattice in three-dimension [90].

2.4.1 Bragg's Law

The relationship between crystal lattice surface and the geometry of diffraction provided by Bragg's law [90]; it stated that when x-ray incident into a crystal surface has θ angle it could reflect back with the same angle of scattering beam ($\theta_{incident} = \theta_{reflected}$), with path difference d between two planes, are an equal number with constructive interference wavelength λ , as shown in **Figure 2.10** [97].

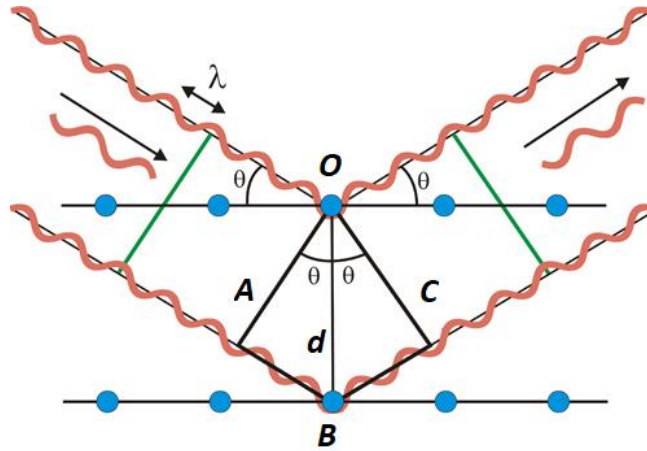


Figure 2.10: Geometry for the interference of waves scattered from a crystal plane and Bragg's law illustration.

It could be derived as

$$n\lambda = AB + BC \quad (2.17)$$

In 1st triangle OAB

$$\sin \theta = \frac{AB}{OB}$$

$$\sin \theta = \frac{AB}{d}$$

$$AB = d \sin \theta$$

In 2nd triangle OBC

$$\sin \theta = \frac{BC}{d}$$

$$BC = d \sin \theta$$

From 1st and 2nd triangle in **Eq. (2.17)**

$$n\lambda = d \sin \theta + d \sin \theta$$

$$= 2d \sin \theta$$

$$n\lambda = 2d_{hkl} \sin \theta_{hkl} \quad (2.18)$$

Where λ is x-ray wavelength, θ_{hkl} is the half-formed angle between incident and diffraction beam $\left(\frac{2\theta}{2}\right)$, d_{hkl} is the perpendicular distance between lattice planes with (hkl) indices, where the value of (hkl) specified by the unit cell of characterized crystal lattice [90].

Among varying wavelengths and observing diffraction patterns, the information about lattice spacing is obtained [97].

The information of nanomaterial could obtain from the peak of the diffraction pattern to calculate the average crystalline size of the sample for a small size less than 100 nm or so [98, 99]. This correlation described by Scherrer equation

$$D = \frac{k\lambda}{\beta \cos \theta} \quad (2.19)$$

Where D represents the average crystal size, k is Scherrer constant for spherical particles equal (0.9), λ is x-ray wavelength, while β refers to the full width at half maximum (FWHM) of reflection peak [98, 99].

2.5 Infrared (IR) Spectroscopy

2.5.1 Theoretical Basics of Infrared Radiation

Infrared radiation is a type of spectroscopy that studies the interaction of infrared spectra with the matter; it uses a spectral light range between 12500 cm^{-1} and 20 cm^{-1} [100]. Infrared radiation subdivided into three kinds; begin with near-infrared (NIR), which has a wavenumber range (12500 cm^{-1} - 4000 cm^{-1}). Another one is mid-infrared (MIR); it's relevant wavenumber subjected between (4000 cm^{-1}

- 400 cm^{-1}). Last of all, far-infrared (FIR) its spectral region confined between (400 cm^{-1} - 20 cm^{-1}), as illustrated in **Figure 2.11** [90].

The infrared spectrum obtained by using an instrument called an infrared spectrometer. The infrared spectrometer has several types of instruments; the most popular one is a Fourier Transform Infrared Spectrometer (FTIR) [100].

A significant development of using IR radiation is identifying the chemical functional groups of samples. The intensity of the infrared spectrum is proportional to the concentration. Hence, IR could be used as a quantitative analysis for concentration measurement [100].

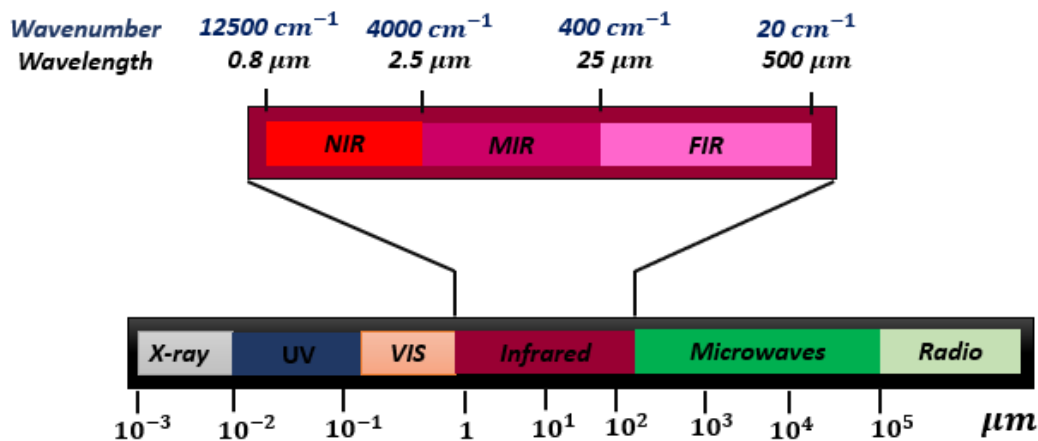


Figure 2.11: Schematic diagram illustrates the infrared spectral region within the electromagnetic spectrum.

The outcome signals peak is absorption bands caused by molecular vibrations. The infrared spectra record the spectrum intensity against incident wavenumber [90, 100].

The incident infrared spectra that affected a chemical compound excited the vibration level on a molecule, and functional groups characterize the appearance bands. There are two types of vibrations; viz stretching or bending vibration. The

vibrational frequency could be simplified as mechanical balls on spring, where the atoms of the molecule represent the ball while chemical bonds represent spring as a classical point of view. **Figure 2.12** represents the difference between both types and their relevant kind [90].

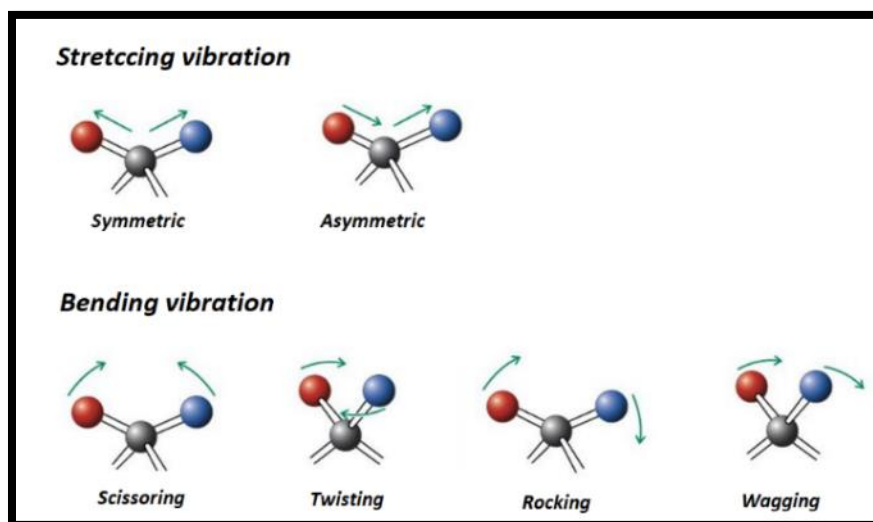


Figure 2.12: Schematic representation of different molecular vibration modes showing bending and stretching vibrations.

2.5.2 Mathematical Consideration of Absorbing Infrared Spectra

There is various type of describing light; via wavelength or wave's frequency. The wavelength λ defined as the distance between two crests or troughs of the wave, its relevant unit is (cm), while the definition of wave's frequency ν is the number of cycles or vibrations undergoes through one second, usually expressed in Hertz (Hz) unit or sec^{-1} [90].

Eq. (2.20) displays the relationship between frequency, wavelength, and the constant speed of light [100].

$$c = \nu\lambda \quad (2.20)$$

Where c is the speed of light, ν represents the frequency, and λ is the wavelength.

The reciprocal of wavelength known as wavenumber is used to distinguish the type of light and used in the purpose of measure the number of cycles in a light wave per centimeter [100].

$$\bar{\nu} = \frac{1}{\lambda} \quad (2.21)$$

Where $\bar{\nu}$ is wavenumber in (cm^{-1}).

From **Eq. (2.20)** and **Eq. (2.21)** and solve for c

$$\nu = \frac{c}{\lambda} \quad (2.22)$$

$$\nu = c \frac{1}{\lambda}$$

$$\nu = c\bar{\nu} \quad (2.23)$$

The previous equations suggest that the light waves might be described, not only according to their wavelength and frequency but also according to their wavenumbers. Furthermore, the equations show that the three quantities are related to each other [100].

Photons are particles of light without mass, but it does have energy. So, the frequency of the photon is proportional to its energy as described by the following Equation

$$E = h\nu \quad (2.24)$$

Substitute from **Eq. (2.22)** and **Eq. (2.23)**, to obtain

$$E = h \frac{c}{\lambda} \quad (2.25)$$

$$E = hc\bar{\nu} \quad (2.26)$$

Where E represent the energy of the photon, h is plank's constant, while c speed constant, $\bar{\nu}$ refer to the wavenumber, and λ is wavelength [100].

The necessary condition for infrared absorption is the sample or compound should have a dipole moment, which measures the polarity of chemical bonds within a molecule; it occurs whenever there is a separation between positive and negative charge. The magnitude of dipole moment could calculate from following an Equation

$$\mu = qr \quad (2.27)$$

Where μ is the magnitude of dipole moment, q is the charge magnitude, and r refers to the distance between charge [100].

The absorption of bands of infrared spectra was absorbed when the oriented electric field of radiation oscillates has the same frequency as a dipole moment. Important to note, the intensity of force has a substantial effect on frequency and intensity absorbed radiation [90].

2.5.3 Hook's Law for Stretching Vibrations

The vibrational transition occurs between different vibrational levels of the same electronic and transition state. Vibrational transitions of molecules have occurred when the energy of infrared overcome force bond, affecting in energy levels called quantum harmonic oscillation or vibrational quantum number ν . A diagram of the vibrational energy level **Figure 2.13** shows the potential energy affected by bond length. At minimum energy level, the molecule remains stable ($\nu = 0$). As a result, its relative bond length show equilibrium state. On the contrary, a bond made longer than equilibrium bond length when molecular energy increases which represent a high vibrational energy level ($\nu = 1$) [90, 100].

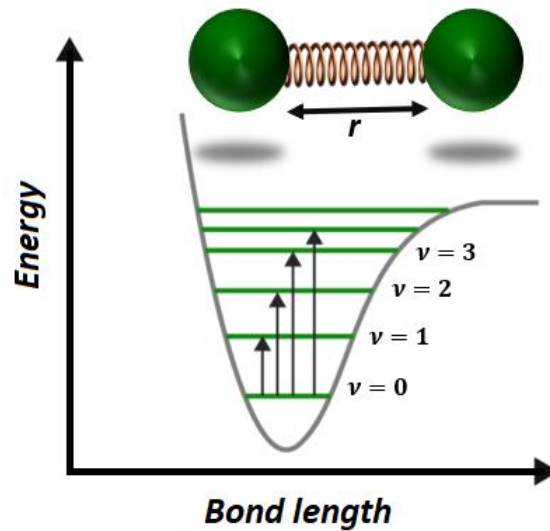


Figure 2.13: Potential energy diagram of the harmonic oscillation model.

Diatomic molecule stretching along x-axis is caused a vibration. This vibration considered to be identical to oscillate two masses around an equilibrium position, connected via a spring — this shows the first approximation under Hook’s law [90].

Hook’s law is used to calculate mathematics vibration frequency of exciting light as a part of a simple harmonic oscillator model as the following Equation

$$F = -kx \quad (2.28)$$

Where F is restoring force, k is spring constant, and x is the displacement spring from the equilibrium position.

Since the of potential energy is

$$V(x) = - \int F dx = \int kx dx = \frac{1}{2} kx^2 \quad (2.29)$$

And from the second law of Newton’s

$$F = ma \quad (2.30)$$

From **Eq. (2.28)** and **Eq. (2.30)**

$$ma = -kx$$

$$m \frac{d^2x}{dt^2} = -kx$$

The total energy is given as

$$E = \frac{1}{2} kx^2 \quad (2.31)$$

Schrodinger wave equation for an independent time at one-dimension of a harmonic oscillator is given by

$$\frac{-\hbar^2}{2m} \frac{d^2\psi}{dx^2} + (V(x) - E(x))\psi = 0$$

$$\frac{d^2\psi}{dx^2} + \frac{8\pi^2m}{h^2} (E(x) - V(x))\psi = 0$$

From **Eq. (2.29)**

$$\frac{d^2\psi}{dx^2} + \frac{8\pi^2m}{h^2} \left(E(x) - \frac{1}{2} kx^2 \right) \psi = 0 \quad (2.32)$$

Eq. (2.32) re-arranged as Hermite differential equation to get vibrational energy level of the molecule as the following Equation

$$E_{vib} = \left(v + \frac{1}{2} \right) h\nu \quad (2.33)$$

$$v = 0, 1, 2, 3, \dots$$

$$E_{vib} = \left(v + \frac{1}{2} \right) hc\bar{\nu} \quad (2.34)$$

where

$$\nu = \frac{1}{2\pi} \sqrt{\frac{k}{\mu}} \quad (2.35)$$

$$\mu = \frac{m_1 m_2}{m_1 + m_2}$$

Where ν is frequency, k is the force constant of spring, μ refers to a reduction in mass of atoms, m_1 and m_2 represent the mass of atom 1 and 2, respectively [100, 101].

Molecular wavenumber of absorbing infrared radiation is given as

$$\bar{\nu} = \frac{1}{2\pi c} \sqrt{\frac{k}{\mu}} \quad (2.36)$$

From Eq. (2.33) and Eq. (2.35) the vibrational energy level of a diatomic molecule, therefore, is written as

$$E_{Vib} = \frac{h}{2\pi} \sqrt{\frac{k}{\mu}} \left(\nu + \frac{1}{2} \right) \quad (2.37)$$

2.5.4 Number of Vibration Modes in Infrared Spectra

As mentioned above, the chemical bond is vibrating due to infrared radiation. The excited atom is a complex of a molecule, and the complex vibration motion is broken down to show what named normal modes. Any mechanical system should have normal modes vibrate at specific frequencies. Above all, different molecule vibrates at a different frequency as a consequence of their different structures [100].

There are two types of vibrational modes; either linear or non-linear, as shown in **Figure 2.14**. According to a linear molecule, the formula of normal modes is $(3N-5)$, where N refers to the number of atoms in a molecule. For example, carbon

dioxide CO_2 has 3-atoms so, it calculated as $(3 \times 3) - 5 = 4$ normal modes. On the other hand, a non-linear molecule has $(3N-6)$ formula for instance, a water molecule H_2O has 3-atoms so, $(3 \times 3) - 6 = 3$ normal modes, as illustrated in **Table 2.1**. The normal modes give the number of peaks in the infrared spectrum [100].

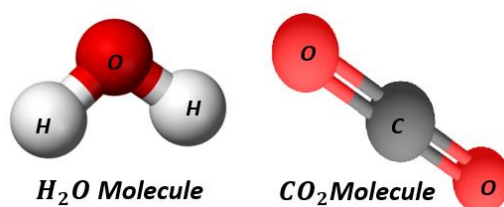


Figure 2.14: Schematic illustrates linear and non-linear chemical bonds.

Table 2.1: Normal mode formula.

Type of Molecule	The formula of normal Mode	Example of 3-Atoms in Molecule
Linear	$3N-5$	4
Non-Linear	$3N-6$	3

Chapter 3

Methodology

and

Instruments

Chapter 3

Methodology and Instruments

3.1 Materials

3.1.1 Gold (III) Chloride Hydrate ($HAuCl_4 \cdot H_2O$)

Gold (III) chloride hydrate ($HAuCl_4 \cdot H_2O$) has a metallic yellow appearance color with molecular weight 339.79 g/mol. Moreover, it has a 99.995% purity trace metal basis. It purchased from Sigma-Aldrich (USA). Their chemical structure is shown in **Figure 3.1**.

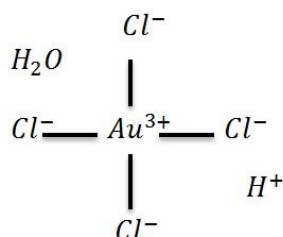


Figure 3.1: Chemical structure of gold (III) chloride hydrate.

3.1.2 Silver Nitrate ($AgNO_3$)

Silver Nitrate is a chemical material has molecular formula ($AgNO_3$) and molecular weight of 169.87 g/mol. It also has a colorless or white crystalline solid becoming black on exposure to light or organic materials. In addition to that, it has a 99.0% purity purchased from BDH (England) company. The structure is demonstrated in **Figure 3.2**.

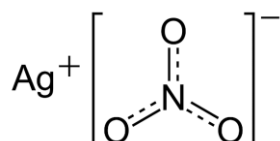


Figure 3.2: Chemical structure of silver nitrate.

3.1.3 Sodium Dodecyl Sulfate ($C_{12}H_{25}NaO_4S$)

Sodium dodecyl sulfate (SDS) is a white to pale yellow powder, has molecular weight 288.378 g/mol with 99% purity. Moreover, it has molecular formula ($C_{12}H_{25}NaO_4S$), and it purchased from Sigma-Aldrich (USA); its structure presented in **Figure 3.3**.

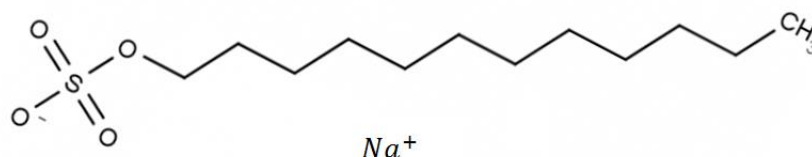


Figure 3.3: Chemical structure of SDS.

3.1.4 Iron (II) Chloride Tetrahydrate (Ferrous Chloride) ($FeCl_2 \cdot 4H_2O$)

Ferrous chloride is a greenish-white crystalline solid, has molecular weight 198.81 g/mol with ($FeCl_2 \cdot 4H_2O$) molecular formula and 99.0% purity. It purchased from Techno Pharmchem, Bahadurgarh, Haryana (INDIA). Their structure is shown in **Figure 3.4**.

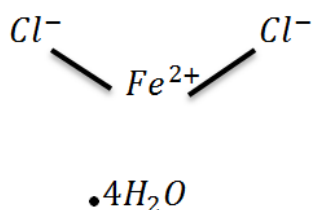


Figure 3.4: Chemical structure of ferrous chloride.

3.1.5 Iron (III) Nitrate Nonahydrate (Ferric Nitrate) ($Fe(NO_3)_3 \cdot 9H_2O$)

Ferric nitrate is a chemical compound that has a chemical formula ($Fe(NO_3)_3 \cdot 9H_2O$). However, it forms colorless to pale violet crystals it forms a yellow solution when dissolved. This compound has a molecular weight of 404.0 g/mol with 98% purity. Last of all, it was purchased from Sigma-Aldrich. Its chemical structure is illustrated in **Figure 3.5**.

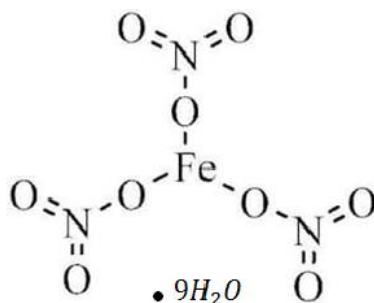


Figure 3.5: Chemical structure of ferric nitrate.

3.1.6 Chitosan ($C_6H_{11}NO_4$)_n

Chitosan is an organic material derived from chitin. The chitin can be extracted from shrimp shells and other crustaceans, then treated by the acid in the first place to dissolve the calcium carbonate followed that decantation by an alkaline solution to dissolve [102]. This material has a low molecular weight (50-190 KDa) and their molecular formula ($C_6H_{11}NO_4$)_n. Moreover, it has floral white color in powder form which is turned to colorless solution while dissolving. It acquired from Sigma Aldrich. Their structure is given in **Figure 3.6**.

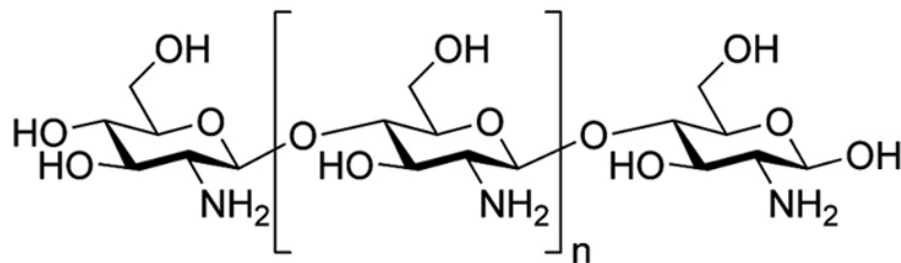


Figure 3.6: Chitosan chemical structure.

3.1.7 Acetic Acid ($C_2H_4O_2$)

Acetic acid is a colorless liquid organic compound with the chemical formula (CH_3COOH) and molecular weight 60.052 g/mol. Its purity reaches 99.8%, was acquired from Sigma-Aldrich corporation. The acetic acid structure is demonstrated in **Figure 3.7**.

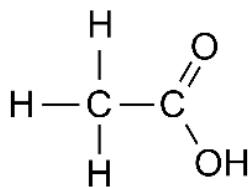


Figure 3.7: Chemical structure of acetic acid.

3.1.8 Sodium Hydroxide ($NaOH$)

Sodium hydroxide ($NaOH$) it is an inorganic compound appeared as white, waxy, and opaque crystal with molecular weight 40 g/mol. Furthermore, it has more than 98% pureness; the manufacturing company was Sigma-Aldrich. Its chemical structure is shown in **Figure 3.8**.

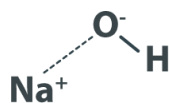


Figure 3.8: Sodium hydroxide chemical structure.

3.1.9 Absolute Ethanol (C_2H_5OH)

Ethanol is a primary alcohol, which is a volatile and colorless liquid. The molecular weight of (C_2H_5OH) is 46.07g/mol. Its purity reaches 99.9% and it purchased from SimNT company. Their structure presented in **Figure 3.9**.

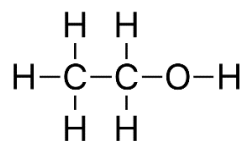


Figure 3.9: Chemical structure of ethanol.

3.1.10 Sodium Diphosphate Monobasic ($NaH_2PO_4 \cdot H_2O$)

Sodium diphosphate monobasic has a chemical formula ($NaH_2PO_4 \cdot H_2O$) with a molecular weight of 137.99 g/mol. It has 99.0% pureness with white crystalline granules, was purchased from BDH. Their structure is demonstrated in **Figure 3.10**.

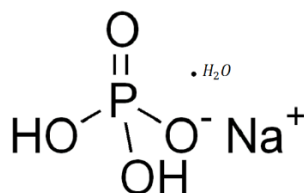


Figure 3.10: Sodium diphosphate monobasic chemical structure.

3.1.11 Disodium Hydrogen Orthophosphate Anhydrous (Na_2HPO_4)

Disodium hydrogen orthophosphate anhydrous is a white powder color appearance, and it has a molecular formula (Na_2HPO_4) with molecular weight 141.96 g/mol and 98% purity. It purchased from Techno Pharmchem, Bahadurgarh, Haryana (INDIA). **Figure 3.11** illustrates its chemical structure.

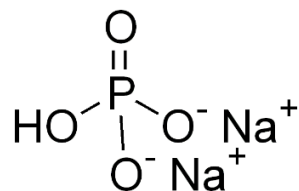


Figure 3.11: Chemical structure of disodium hydrogen orthophosphate anhydrous.

3.1.12 Ammonium Hydroxide (NH_4OH)

Ammonium hydroxide is a colorless aqueous solution has 35.046 g/mol molecular weight and (NH_4OH) liner formula. It purchased from CODEX CARLO ERBA company with 28% purity. Their chemical structure is shown in **Figure 3.12**.

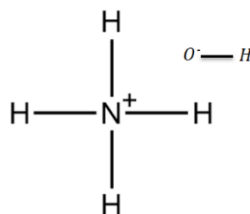


Figure 3.12: Ammonium hydroxide structure.

3.1.13 Cobalt (II) Chloride 6-Hydrate (Cobaltous Chloride) ($CoCl_2 \cdot 6H_2O$)

Cobaltous chloride is an inorganic compound that has a dark red color, ($CoCl_2 \cdot 6H_2O$) chemical formula with 237.93 g/mol molecular weight and 99% purity. It purchased from the BDH corporation. It's chemical structure demonstrated in **Figure 3.13**.

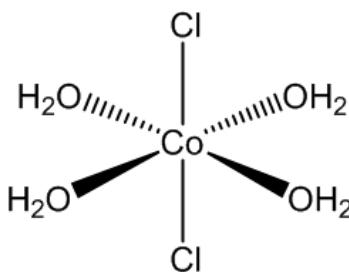


Figure 3.13: Chemical structure of cobaltous chloride.

3.1.14 Hydrazine Hydrate ($N_2H_4 \cdot H_2O$)

Hydrazine hydrate is a colorless chemical compound that has 50.061 g/mol molecular weight. Its chemical formula is ($N_2H_4 \cdot H_2O$), and this structure was illustrated in **Figure 3.14**.

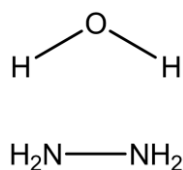


Figure 3.14: Chemical structure of hydrazine hydrate.

3.1.15 Nickel (II) Nitrate Hexahydrate ($Ni(NO_3)_2 \cdot 6H_2O$)

Nickel (II) nitrate hexahydrate ($Ni(NO_3)_2 \cdot 6H_2O$) is a linear formula that has 290.79 g/mol molecular weight and greenish-blue crystal color. **Figure 3.15** shown its chemical structure.

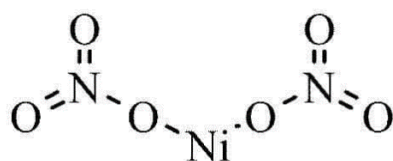


Figure 3.15: Chemical structure of nickel (II) nitrate hexahydrate.

3.2 Experimental Methods

3.2.1 Green Synthesis of Gold and Silver Nanoparticles

Fresh fruits of lemon were taken as a reducing and capping agent. The lemon was washed, cut, and squeezed to extract the juice. This extract was filtered using Whatman filter paper to remove undesired impurities. The mixture was boiled for 2 hours. This juice used for further experiments.

3.2.1a Preparation of Gold Nanoparticles with Different Concentrations of Lemon Extract

To prepare gold nanoparticles sample S_1 , 10 ml of $HAuCl_4 \cdot H_2O$ ($5.589 \times 10^{-3} M$) was added to 50 ml distilled water and brought to a boil with vigorous stirring for about 20 minutes of heat. To this solution, (4 ml) of the lemon extract was added, then the heat was turned off while the sample still under stirring. Afterward, a color change was observed from a bright yellow color to purple and then to ruby red within 10 minutes. The ruby-red colloidal solution was stirred for an additional 20 minutes, then cooled at room temperature. For this prepared colloidal sample, UV-visible and TEM were measured. The sample was centrifuged at (15,000 rpm) for 30 minutes, then dried for 18 h at $80^\circ C$ and collected for IR measuring. To sum up, the steps of preparation gold nanoparticles demonstrated on **Figure 3.16**.

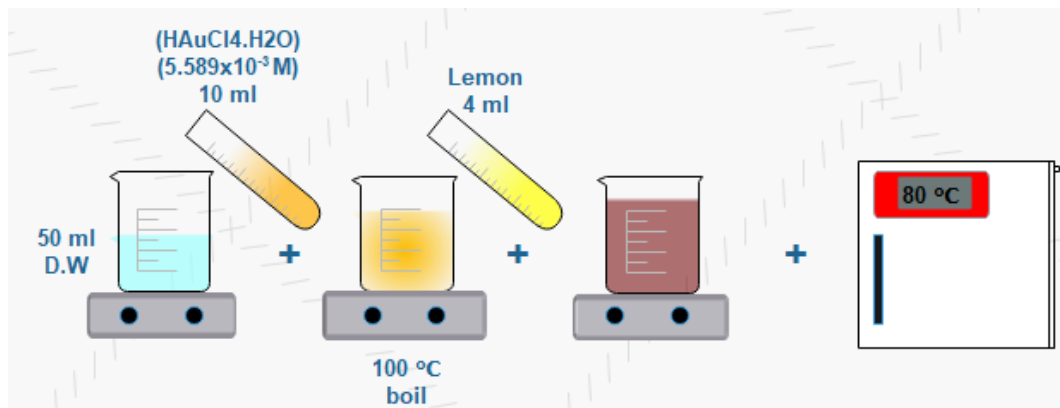


Figure 3.16: Schematic diagram of experimental steps for preparing AuNPs sample S_1 .

Sample S_2 and S_3 were prepared by the same method as mentioned above in S_1 expect that the lemon solution was changed according to **Table 3.1**. All three samples could be found in **Figure 3.17**.

Table 3.1: Quantity of chemical reactant for gold nanoparticle preparation method ($S_1 - S_3$).

Samples	Distilled Water	$HAuCl_4 \cdot H_2O$ ($5.589 \times 10^{-3} M$)	Lemon Extraction Solution
S_1	50 ml	10 ml	4 ml
S_2	50 ml	10 ml	5 ml
S_3	50 ml	10 ml	6 ml



Figure 3.17: Prepared gold nanoparticles samples.

3.2.1b Preparation of Silver Nanoparticles with Different Concentrations of Silver Nitrate

Silver nanoparticles sample S_4 was prepared by dissolving 0.1019 g of $AgNO_3$ (3 mM) in 200 ml distilled water. This solution was added dropwise to 40 ml of lemon extract at 80 °C under dark conditions with continuous stirring for reduction Ag^+ ions. As a consequence, yellowish color was appeared at the same

time of adding silver solution then turned to yellow after a while it converted to dark brown. To avoid silver nanoparticles aggregation, after 3 h of a mixture, 12 ml of (8 % w/v) sodium dodecyl sulfate (SDS) was added, and the hot plate turned off after 25 minutes. This colloid stored at room temperature. The UV-vis and TEM were measured for this sample. The sample was collected to be used in IR measuring after centrifugation at (15,000 rpm) for 30 min and washed with distilled water then dried at 80 °C for 18h. The steps of preparation silver nanoparticles were simplified in **Figure 3.18**.

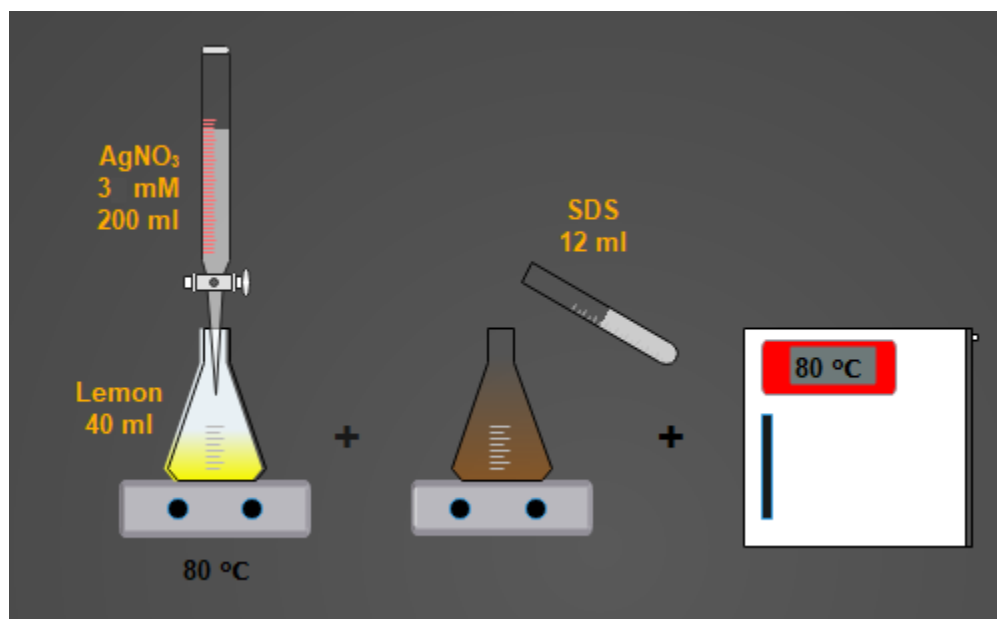


Figure 3.18: Representation diagram of experimental steps for preparing AgNPs sample S_4 .

Sample S_5 and S_6 was prepared by varying concentration of $AgNO_3$ as following to **Table 3.2**. The image of three samples could be found in **Figure 3.19**.

Table 3.2: Quantity of chemical reactant for silver nanoparticle preparation method ($S_4 - S_6$).

Samples	Lemon	(200 ml) of $AgNO_3$	Solution of SDS (8 % w/v)
S_4	40 ml	3 mM	12 ml
S_5	40 ml	4 mM	12 ml
S_6	40 ml	5 mM	12 ml



Figure 3.19: Prepared silver nanoparticles samples.

3.2.2 Synthesis of Iron and Cobalt as a Magnetic Nanoparticles

Chitosan in this experiment was used as capping material for iron nanoparticle. To prepare a 1% solution of chitosan, 2 g of chitosan dissolved in 200 ml of distilled water with a high-speed stirrer. 6 ml of acetic acid added while

agitation is continuing. Stirred and heated continually for one hour or until dissolution is complete.

3.2.2a Preparation of Iron Nanoparticles Capped by Chitosan at Different Concentrations of Iron

Chitosan-coated magnetic nanoparticles were formed by co-precipitation of iron salts in chitosan polymer S_7 . To prepare this sample, a 3.6×10^{-3} mM of (Fe^{3+} : Fe^{2+}) was dissolved in 1% from prepared chitosan. The ratio of (Fe^{3+} : Fe^{2+}) was prepared by adding ferric nitrate and ferrous chloride with (2:1) molar ratio at 85 °C for 40 minutes. After that, the solution was ultrasonicated at (70% amplitude) for 10 min to promote better distribution, and then the chitosan-iron solution was precipitated by adding a dropwise of (NaOH: ethanol) with a mixture volume ratio of (4:1). The alkaline precipitate mixture was homogenized in solution again using a vortex for 30s. This colloid was aged under orbital shaker for 18h (60 rpm). After that, the composite precipitate was collected by centrifugation for 30 min at (15000 rpm). The suspensions were removed, and the precipitate washed with 50 mM phosphate buffer pH 7.22 and ethanol with a (1:1) volume ratio. The precipitate samples were redistribution in distilled water before dried for UV-vis measuring. Then, dried at 80 °C for 10 h. Finally, an agate mortar used to find fine powder to be ready for TEM, X-ray, and FTIR analysis (Note: TEM was measured before and after dried). **Figure 3.20** outlines the steps of synthesized silver nanoparticles. While measurement samples were illustrated in **Figure 3.21**.

Note: 100 ml of phosphate buffer was prepared by mixed 50 mM of Sodium Diphosphate Monobasic ($NaH_2PO_4 \cdot H_2O$) with 50 mM of Disodium Hydrogen Orthophosphate Anhydrous (Na_2HPO_4). The mixture of solution was adjusted with ammonia and acetic acid to reach 7.22 pH.

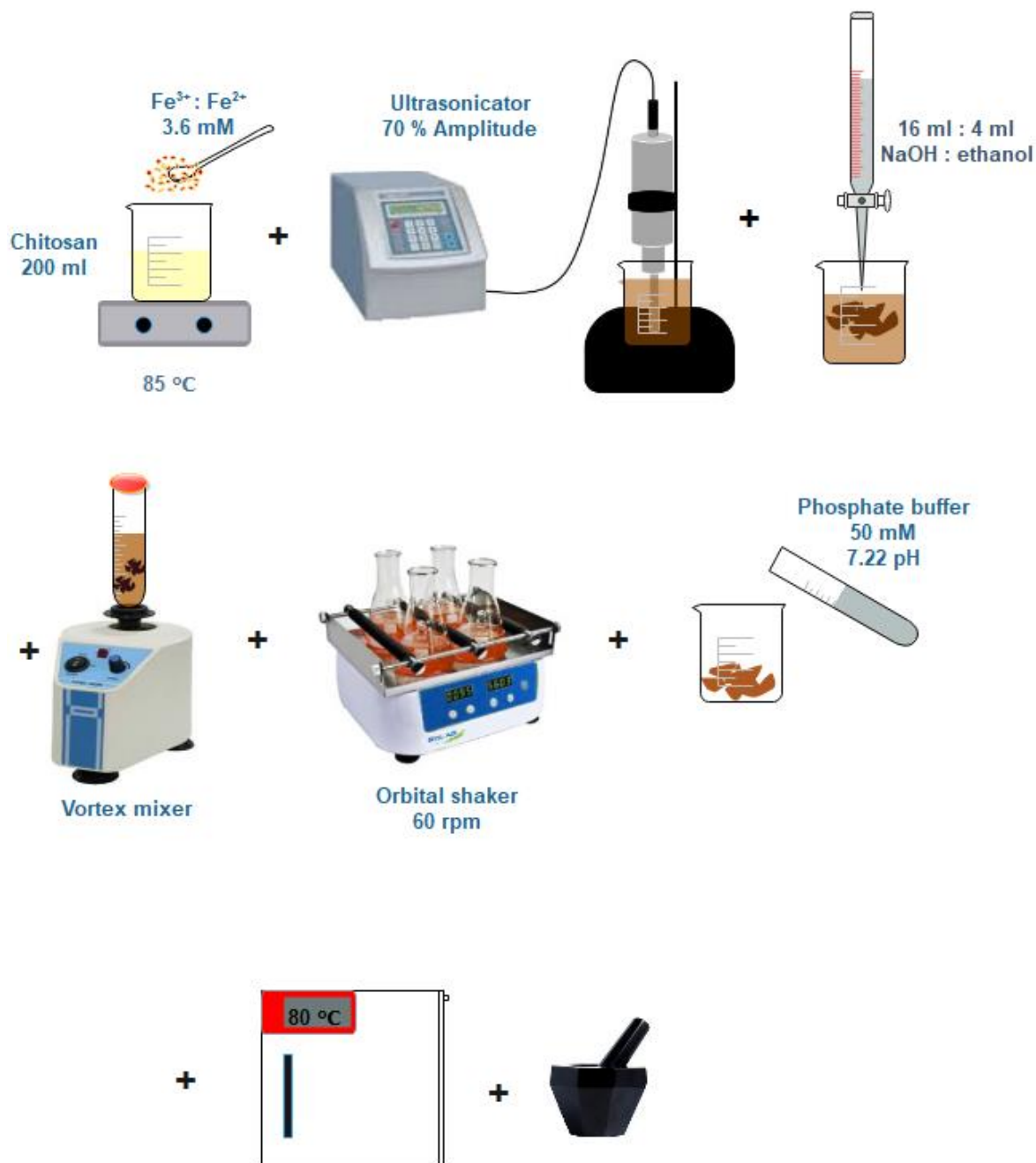


Figure 3.20: Representation diagram of experimental steps for preparing FeNPs sample S_7 .

Sample S_8 and S_9 were prepared in the same method of S_7 with varying concentrations of Fe, as presented in **Table 3.3**.

Table 3.3: Quantity of chemical reactant for iron preparation method ($S_7 - S_9$).

Samples	Chitosan	(2:1) Molar Ratio of ($Fe^{3+} : Fe^{2+}$)	NaOH and Ethanol (4:1) Molar Ratio
S_7	200 ml	3.6 mM	20 ml
S_8	200 ml	4.6 mM	20 ml
S_9	200 ml	5.6 mM	20 ml

*Figure 3.21: Measurement samples of iron nanoparticles.*

3.2.2b Preparation of Cobalt Nanoparticles with Different Concentrations of Sodium Hydroxide

Cobalt salt was dissolved in distilled water with (0.25 M). To prepare cobalt nanoparticles S_{10} , cobalt solution was adjusted at 11.385 pH by ammonia solution (while adjusting, the color changed from red to black). After that, the solution was

heated at 75°C for about 80 minutes. Follow that, 5 ml of hydrazine hydrate added to the solution; the color turned to bluish violet. Before adding 3 ml of NaOH 0.5 M drop-by-drop, the solution was heated and stirred for 30 min. The solution continued stirred for a further 40 min to complete reaction. For this sample, UV-Visible and TEM were measured. Nanoparticle solution was centrifuged at (14,000 rpm) for 20 minutes to obtain powder nanoparticles followed by re-dispersion in ethanol then in distilled water. Finally, the precipitate dried at 80°C for 21 h. After that, X-ray and FTIR measured. The experimental steps for preparation cobalt nanoparticles illustrated in **Figure 3.22**.

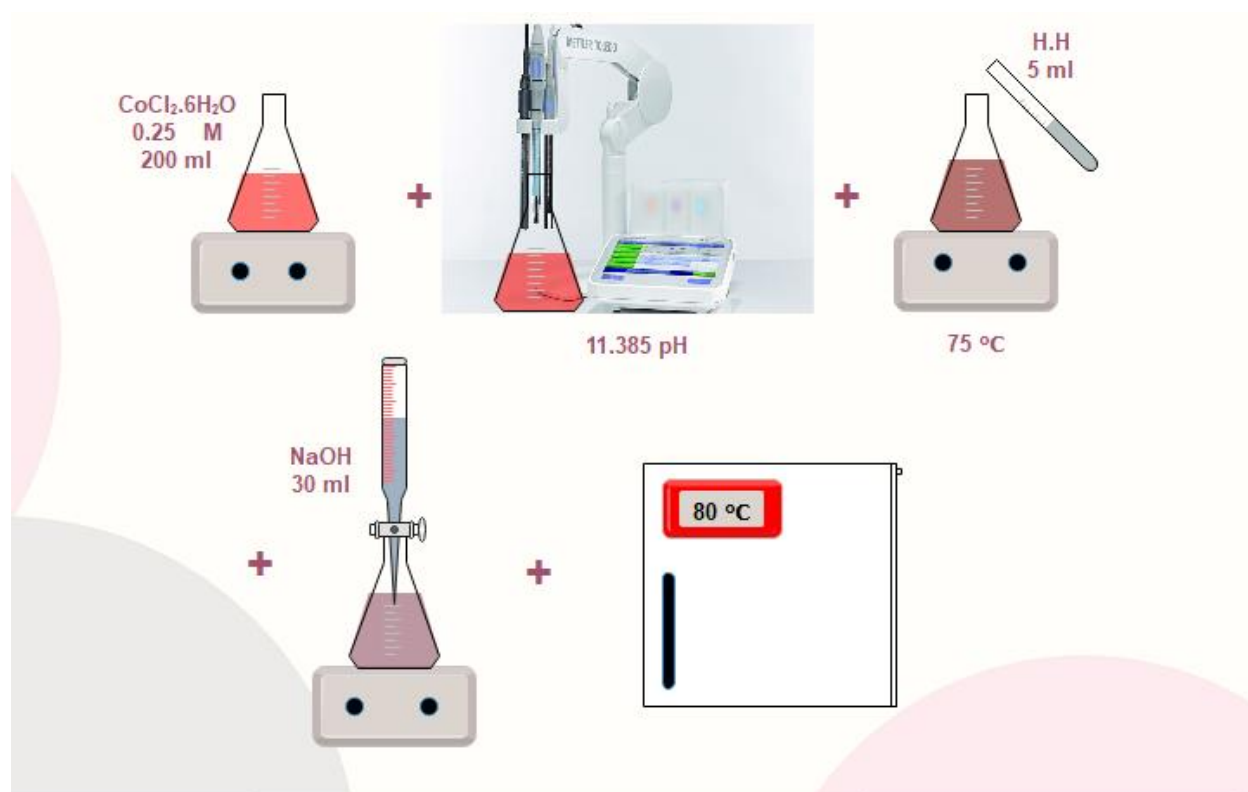


Figure 3.22: Representation diagram of experimental steps for preparing CoNPs sample S_{10} .

Sample S_{11} and S_{12} were prepared by the same method of S_{10} except NaOH concentration was changed, as presented in **Table 3.4**. Prepared and measurement samples of cobalt nanoparticles could be found in **Figure 3.23**.

Table 3.4: Quantity of chemical reaction for cobalt preparation method (S_{10} – S_{12}).

Samples	$CoCl_2 \cdot 6H_2O$ (0.25 M)	Hydrazine Hydrate	The Concentration of (NaOH) 30 ml
S_{10}	200 ml	5 ml	0.5 M
S_{11}	200 ml	5 ml	1.5 M
S_{12}	200 ml	5 ml	2.5 M



Figure 3.23: Prepared and measurement samples of cobalt nanoparticles.

3.3 Instrumentation Techniques

3.3.1 Ultraviolet/Visible Spectrophotometer Technique (UV-Vis)

UV-visible spectroscopy is a type of analytical technique used to study the optical properties of materials and electronic transition of molecules. The electronic transition depending on measuring the absorbance intensity of monochromatic light by colorless compounds [103]. **Figure 3.24** outline what this technique consists of:

- 1- Light Source** the classical spectroscopy employs Deuterium D₂ lamp or Hydrogen H₂ lamp for ultraviolet spectrometer, which has radiation emission between (160 nm – 375 nm). On the other hand, tungsten filament lamp is commonly used in visible light, which has a range between (350 nm – 2500 nm). The electric excitation of both Deuterium and Hydrogen arc produces continuous spectra of UV at low pressure. On the contrary, the emission energy of tungsten filament light proportional to the fourth power of operating voltage [103].
- 2- Monochromator** is a device used to resolve wide band of entrance polychromatic light radiation into narrow band of monochromatic radiation; through passing from filters, grating, or prism [103].
- 3- Sample Holder** is the container of sample and reference solvent; it should be transporting the light radiation which passes through them. To be specific, quartz or fused silica cuvette is used as a sample holder for both UV and visible spectroscopy, while a cuvette manufactured from silicate glass can be used just for radiation between (350 nm – 2000 nm) [103].
- 4- Detector** is the part that converts light energy into electrical signals and displayed on a readout device. It should be quantitative response to wide

spectrum of radiation; it also has high sensitivity and low noise level. There are three types of detectors; photomultiplier tube detector (PMT), photodiode detector array (PDA), and charged coupled device (CCD) [90, 103].

- a) The photomultiplier tube detector (PMT) are sensitive to UV-visible radiation; it consists of a photosensitive cathode, and several dynodes a collection anode. A piece of light comes in photon and hits a photocathode causing emission of several electrons [103, 104].
- b) The photodiode array (PDA) responds for both visible and ultraviolet radiation; it consists of number of silicon photosensitive diodes on a single silicon chip. Each diode measures the intensity of specific wavelength. PDA considered as a fast detector due to scanning monochromator usage [90, 103].
- c) Charged coupled device spectrometers (CCD) is a light-sensitive integrated circuit that has two dimensions to detect elements in pixels. In addition, it has better performance than photomultiplier tube. CCD is similar to PDA, but instead of using diode in PDA, it uses photo capacitor in CCD [90, 103].

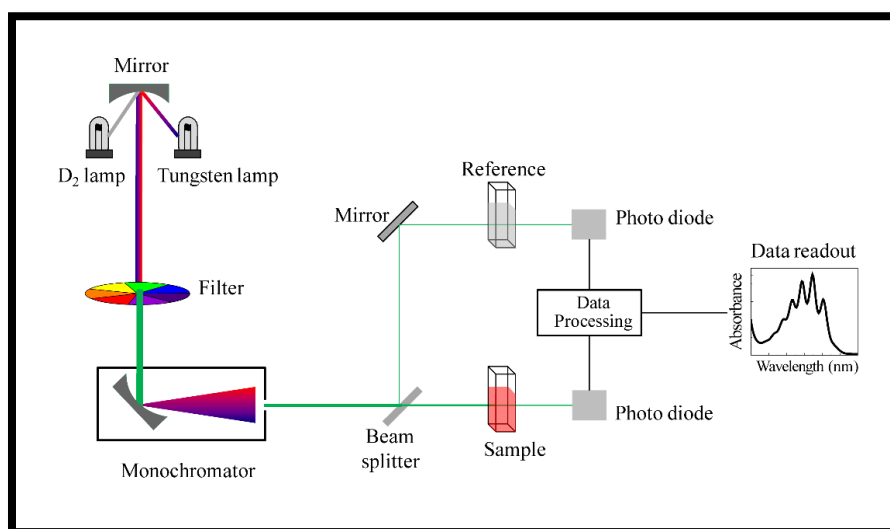


Figure 3.24: Representation diagram of UV-Vis spectroscopy technique.

As motioned above, beam of light from UV-visible source separated into several wavenumbers using filter, grating, or prism to obtain monochromator light; each monochromatic light split into parallel beams using mirror or chopper for double-beam spectrometer. One of the splitting beams passes through reference cuvette while another one passes through the sample cuvette. The intensity of light beams is measured and compared by detector and then amplified to monitor [90, 103].

In our work, all samples were measured as a colloidal sample dissolved in distilled water, so we use the reference as a distilled water.

3.3.2 High-Resolution Transmission Electron Microscopy (HR-TEM)

Transmission Electron Microscopy is a microscopy technique in which a beam of electron moves through a column vacuum chamber passing through multiple lenses to showing the shadow of a specimen sample as represented in **Figure 3.26** [90]. The vacuum chamber in TEM consists of:

- 1- Electron Gun** it designed to create a beam of electrons via thermionic emission process, which has high kinetic energy to make a beam pass through specimen. The electron gun consists of cathode, which is a source of electron that has a high negative potential [105]. The theoretical basic of TEM was explained in details in chapter 2 under subtitle (2.3.1)
- 2- Condenser Lenses** is a set-up of different coils that apply uniform magnetic fields; it used to focus the electrons in a horizontal direction with a very thin beam [105].
- 3- Specimen Stage** TEM specimen is used circular diameter with 3 mm (copper grid), as shown in **Figure 3.25**, which is perpendicular to disk. The specimen

sample must be very thin to make electron beams able to transmit through it. Furthermore, the copper grid, which has a sample fixed on a stationary holder [105].

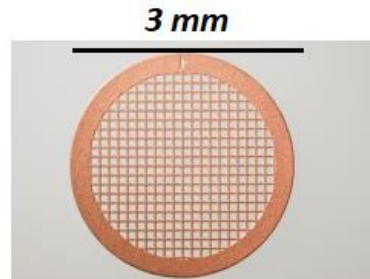


Figure 3.25: Illustration of TEM copper grid.

- 4- **Objective Lenses** are used to form magnified image of an illuminated area that transmitted from specimen stage. It also used to move a beam in a small spot [105, 106].
- 5- **Monitor** the image or diffraction pattern, is viewed on a fluorescent screen or CCD camera, giving a shadow of a sample [105].

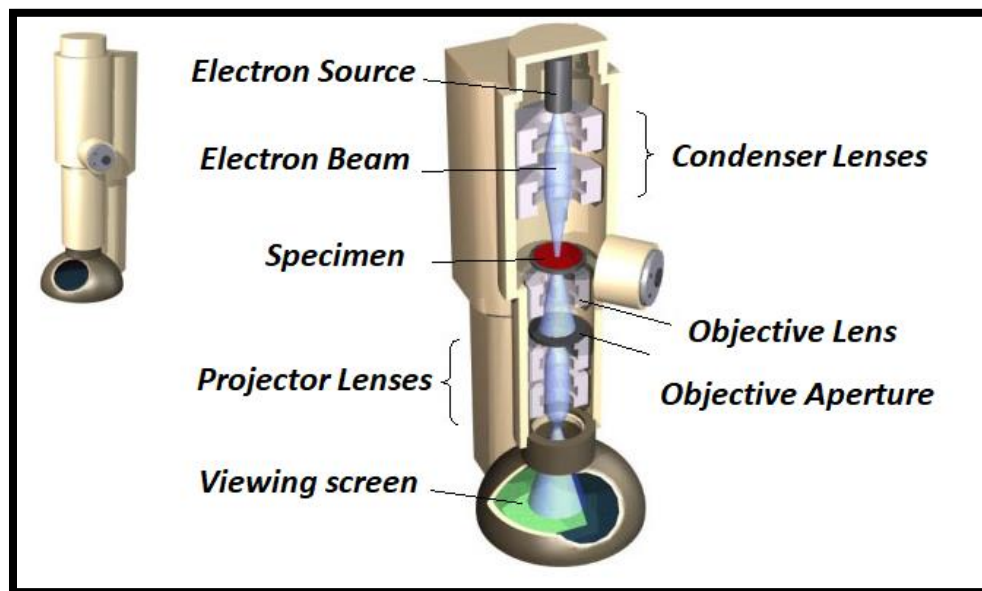


Figure 3.26: Illustration of an electron beam path in TEM.

The cathode in an electron gun connected with a high-tension power supply to emit a beam of electrons into a magnetic lens. The lens system act as a controlling and focusing beam to pass through specimen sample. After that, the transmitted beam passes through objective lenses which select the image and then projected onto a fluorescent screen or CCD camera as photograph image [90, 105].

To obtain TEM measurements with homogeneous distribution of nanoparticle in copper grid, disperse nanoparticle in solution for about 5 minutes using ultrasonication device, then placing droplet from suspension on copper grid immediately. After that, quite the grid to dry at room condition.

For our samples, the TEM was measured as a solution without drying. To be noted, Iron samples were measured twice first as a solution before dried while the second one it measured after dried and dissolving in distilled water again.

3.3.3 X-Ray Diffraction Spectrometer Technique (XRD)

XRD is a powerful nondestructive method of analysis of crystalline materials and determines the orientation of single crystal or grain [107]. As shown in **Figure 3.27**, x-ray spectrometer consists of:

- 1- X-ray Tube** the production source is a large vacuum tube containing a heated cathode of tungsten filament, which accelerated towards a metal target as copper Cu and molybdenum Mo (anode) [106].
- 2- Monochromator** commonly used to disperse various undesirable spectral of incident beam and passed required radiation. There are two types of monochromator in x-ray; viz filter and crystal monochromator [108].

- 3- **Collimator** is a device used to get a narrow beam of x-rays. The x-ray pass through a collimator, which consists of two closely placed metal plates separated by a small gap [109, 110].
- 4- **Detector** is available for monitoring and measures the diffraction intensity of the photons of various spectral lines as singled out by monochromator. The detector in x-ray divided into two types, either photographic or counter [108].

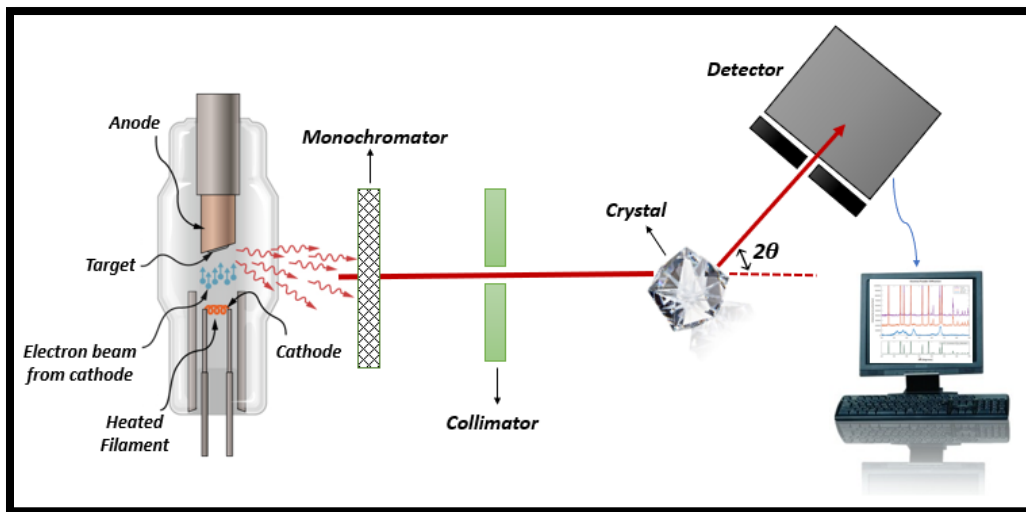


Figure 3.27: Scheme of x-ray diffraction instrument.

X-ray generated in a cathode by heating the filament to produce electrons with focusing emission from filament into anode; the accelerated electron strikes the target material atoms dislodging inner shell electron of target atom. As a result, electrons on outer shell jump down to fill the gap in inner shell. Because the inner shell has lower energy than outer shell, when an outer shell electron jumps into inner shell, it emits radiation in form of x-rays, as shown in **Figure 3.28** [108].

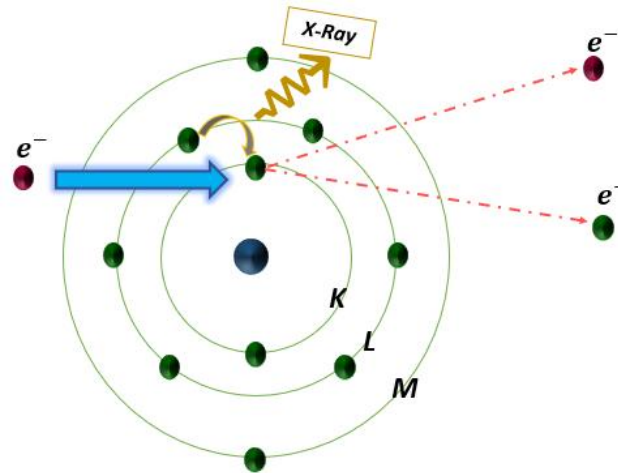


Figure 3.28: Illustration of induced emission of characteristic x-ray from an atom with an electron beam.

The x-ray diffraction based on constructive interference of diffraction monochromatic light produced by x-ray tubes. The radiation collimated and filtered to be concentrated and directed toward the sample. The basic concept of interference light could observe via Bragg's law to characterize crystal or polycrystalline material. The intensity of reflected x-rays is recorded at detector as soon as the sample rotating. After that, detector process what recorded signals then converted into monitor or computer device [107, 111].

To prepare our work, the samples were dried then agate mortar was used for iron samples to measure as a powder.

3.3.4 Fourier Transform Infrared Spectroscopy (FTIR)

Most FTIR spectroscopy uses a Michelson interferometer as the basis of IR analysis. Michelson interferometer, as depicted in **Figure 3.29**, is a beam of infrared radiation split into two paths, and then its relative path could be varying with respect to others [112]. A common instrumentation system of FTIR consist of:

- 1- **Interferometer** the interferometer divides the radiant beam then recombines them to produce repetitive interference signals “encoded”, it consists of three active components; moving mirror, fixed mirror, and beam splitter [112].
- 2- **Detector** the majority type of IR detector categorized into three parts; which is photon detector, thermal detector, and radiation field detector.
 - a) Photon detector which absorbs photons through an electronic transition to produce electrical output signals proportional to the number of absorbed photons. For instance, photoconductive detector; has a high sensitivity of IR detection [113].
 - b) Thermal detector, this detector based on measuring temperature rises that resulted from absorption light of incident radiation. Plotted signals depend on material temperatures. Thermal detector is frequently used in a wide spectral region even though in far-infrared radiation, unfortunately, this type is less sensitive than photodetector [113].
 - c) Radiation field detector, which is a very small detector and it neither depends on thermal effects nor charge carrier generation, but it depends on responding radiation field directly [113].

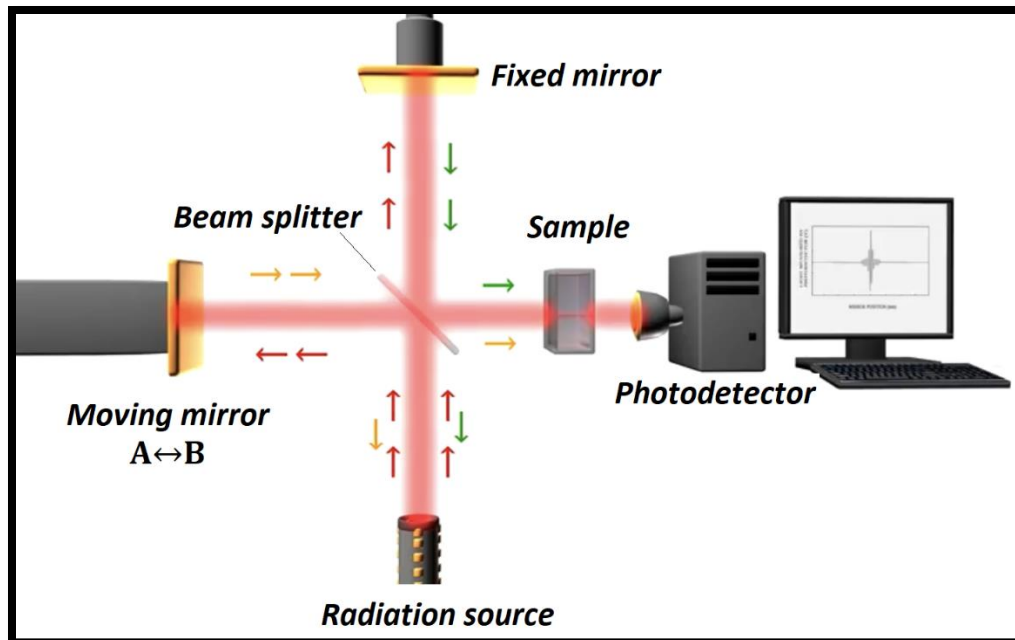


Figure 3.29: Schematic diagram of a conventional Michelson interferometer.

Monochromatic infrared radiation coming from light source reaches to splitter, which is at the center of device, some of radiation pass through splitter while the other part reflected. These two beams reach to mirror then reflected back to splitter. At a splitter, both beams are split again, then the passing radiation recombine and sent toward the sample and the sample will absorb onto detector. On the contrary, other parts of radiation reflected by mirror then go to radiation source again. According to moving mirror from point to other ($A \leftrightarrow B$), detector will give interferograms by computing constructive and destructive interference by measuring the intensity of interferogram reaches to detector; this interferogram converted into spectrum to process known as Fourier transform [90, 112].

To prepare our sample for IR measurement, 0.002 g of prepared sample (powder) was mixed with 0.198 g of KBr in agate mortar then compact powder into a disc as a sandwich. After that, take IR radiation to pass through a disc.

Chapter 4

Results

and

Discussion

Chapter 4

Results and Discussion

4.1 Ultraviolet-Visible Spectroscopy

4.1.1 Ultraviolet-Visible Spectra of Gold Nanoparticles Prepared at Different Concentrations of Lemon

Figure 4.1 shows the ultraviolet-visible spectra of gold samples which prepared at a constant concentration of $HAuCl_4.H_2O$ ($5.589 \times 10^{-3} M$) with different molar ratios of lemon fruit extract where S1 (4 ml), S2 (5 ml), and S3 (6 ml). From this Figure, it is clear that an absorption band was appeared at wavelengths 564 nm, 556 nm, and 548 nm for S1, S2, and S3, respectively. These bands are indicating of AuNPs formation and this bands are due to the collective of excitation electrons at the surface of AuNPs that assigned a surface plasmonic resonance (SPR).

As a general, the phenomena of SPR is referring to the excitation of free-electrons in noble metal nanoparticles at the surface due to the interaction of electromagnetic waves [114, 115]. The surface plasmon resonance occurs when the wavelength of the incident light is higher than the nanoparticle size, which is less than 50 nm [116].

The electric field probe in electromagnetic radiation able to move the whole electron cloud at the surface particle in the same direction to be polarized, and the surface charged appear at the opposite end of the particle, as shown in **Figure 4.2**. The field in resonance with the surface plasmonic oscillation causes free-electrons to oscillate. The oscillation of polarized particles creates another electric field against direction of excitation field, causing restoring force, which leads to

absorbing and scattering light waves, as depicted in **Figure 4.2**. For gold nanoparticles, the resonance condition achieved at a visible frequency of spectrum light [116, 117].

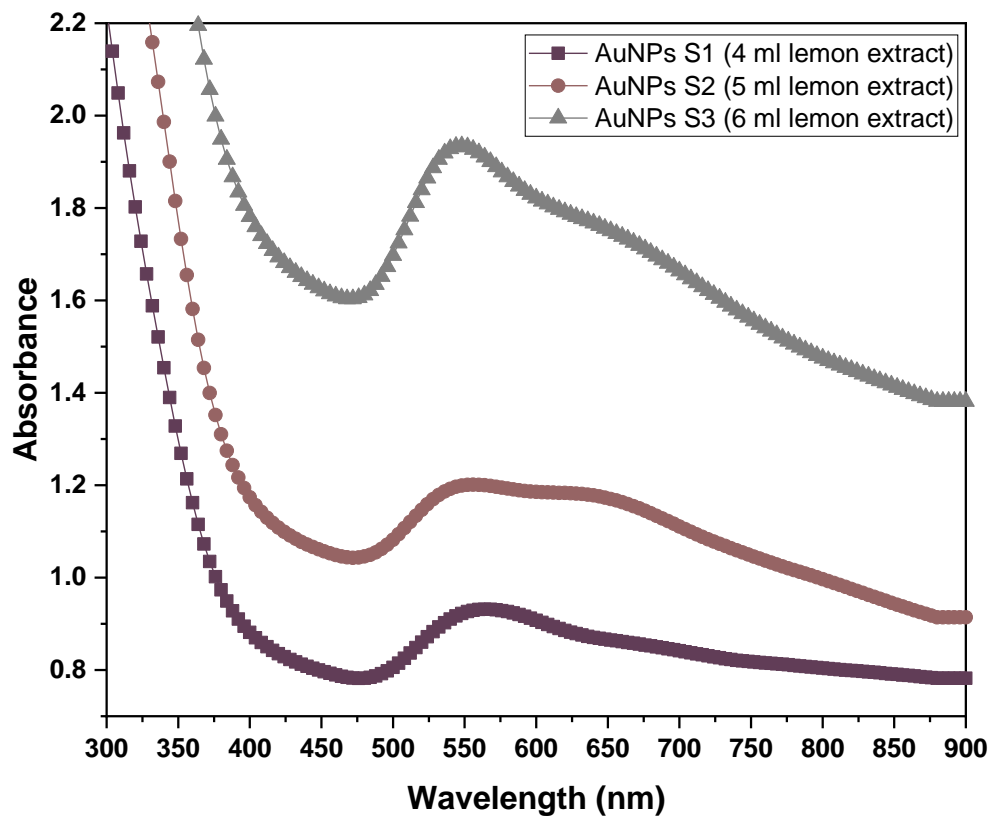


Figure 4.1: Ultraviolet-visible spectra of gold nanoparticles prepared by adding 10 ml with concentration ($5.589 \times 10^{-3} M$) of gold salt with a different molar ratio of lemon extract; S1 (4 ml), S2 (5 ml), and S3 (6 ml).

Surface plasmonic resonance oscillation is not dependent only on the size and shape of gold nanoparticles but also about dielectric materials and the surrounding or solvent medium [114, 117].

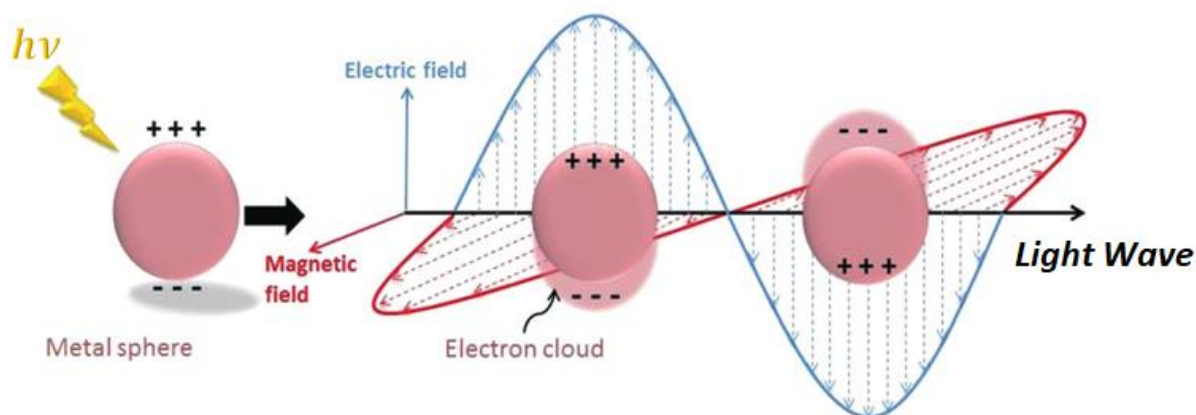


Figure 4.2: Schematic illustration of a localized surface plasmon resonance [118].

From an illustrated **Figure 4.1**, it has found that the SPR bands were shifted to lower wavelengths in whole gold samples with increasing the quantity of lemon extract that used as a reducing and stabilizing agent. This result what indeed reported by Sujitha et al., [83]. Moreover, the SPR band becomes sharper with increases lemon extract due to the enhancing nanoparticle formation.

Interestingly, the peak position of absorption band is blue-shifted for S1, S2, and S3 when the lemon extract increased as plotted in **Figure 4.3**. The blue shift phenomena obtained when the orbitals of electron become further to each other, which lead to absorb high energy with small particle size. Therefore, the wavelength peaks shifted is depend on the size [119, 120].

SPR band that appears at a higher wavelength (red-shifted) for sample (S1) has broadened peaks due to their overlapping orbitals. Besides, the particle size of the red-shifted wavelength band specialized as a large size. Furthermore, the large bandwidth caused to loss of coherent electron [119, 120].

The absorption of AuNPs S1 appeared at 564 nm corresponds with absorbance intensity 0.931612, while the intensity of S2 is 1.20119, and S3 appears at 1.93451.

As this result has shown, the increasing in lemon extract as shown in **Table 3.1** lead to increase the intensity; this increase in intensity follows Beer-Lambert law $A = \log_{10} \left(\frac{I_0}{I} \right) = \varepsilon cl$.

For all samples (S1 – S3), the particle size was decreased with increasing lemon extract; this might because the increase in extract lead to an increase in viscosity of the solvent medium around the Au^0 which impedes its movement and decrease their agglomerations, then its particle size will decrease as a consequence. The low band intensity (hump) appeared at approximately 650 nm in S2 and S3 may be due to nonuniform formation of nanogold.

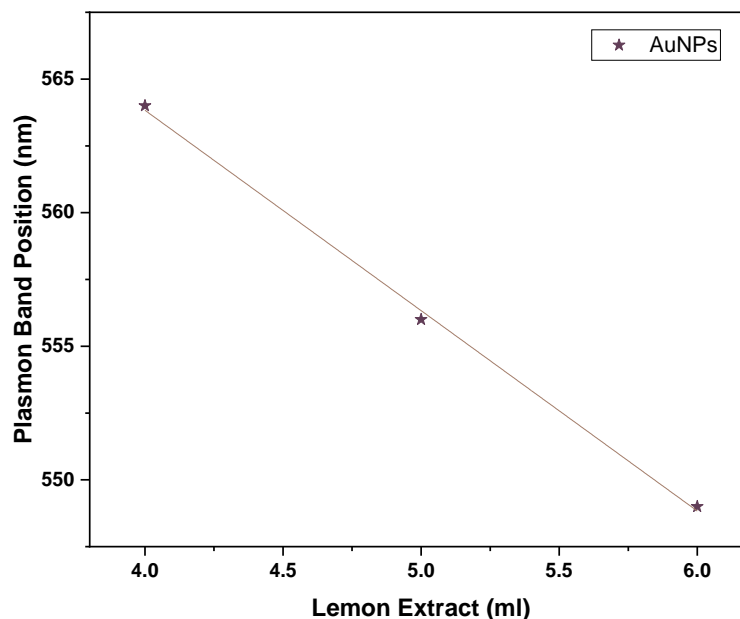


Figure 4.3: Plot illustrates the gold nanoparticle at maximum band position (SPR) against lemon extract concentration for S1, S2, and S3.

4.1.2 Ultraviolet-Visible Spectra of Silver Nanoparticles Prepared at Different Molar Ratio of Silver Nitrate

The silver samples were monitored after changing its color and the colloidal solution was measured by UV-Vis spectrum, as shown in **Figure 4.4**. The silver samples prepared at a fixed value of lemon extract which used as reducing agents and different concentrations of $AgNO_3$ as reported in **Table 3.2**. The illustrated Figure represents the absorption bands at different wavelength.

By comparing the absorption of prepared samples S4, S5, and S6, it had noticed that the wavelength band of S4 spanned at 432 nm, and the wavelength of S5 was 452 nm, while S6 has 448 nm as presented in **Figure 4.4**. These bands is due to silver nanoparticle formation the excitation of surface plasmon vibration in AgNPs, as explained under **Title 4.1.2**. SPR peak has a sensitive manner to nanoparticle size, shape, concentration of lemon, and silver nitrate ratio.

It is clear from **Figure 4.4** that, the SPR band in S4 has 432 nm, and S5 has 452 nm which increase with increasing the ratio of $AgNO_3$ precursor and then decrease again in S6 to 448 nm wavelength. The interpretation of mentioned phenomena is the silver nanoparticles aggregate Ag atom by reducing silver nitrate ions Ag^+ into silver at the nanoscale, which is higher wavelength with more broadening in peaks; this indicates of obtaining larger nanoparticle size in solvent. Furthermore, silver nanoparticle increases its size with increasing the ratio of $AgNO_3$ from (3 mM) to (4 mM). The aggregation shifted to red absorption band (high wavelength); this reason is due to electric dipole interaction and coupling between plasmons oscillation of neighboring particles.

Sample S6 has 5 mM of silver nitrate which is the highest amount, shows particular results represented in sharper with lower wavelength; Because the precursor was added step by step to reducing agents; with some precursor added at the beginning of synthesis, the silver ions complete its nucleation phase while the precursor is continually adding, it then would be larger particles. The extra amount of precursor may also form some new nucleation centers, which would appear as really small metal NPs and could cause a blue shift in spectra.

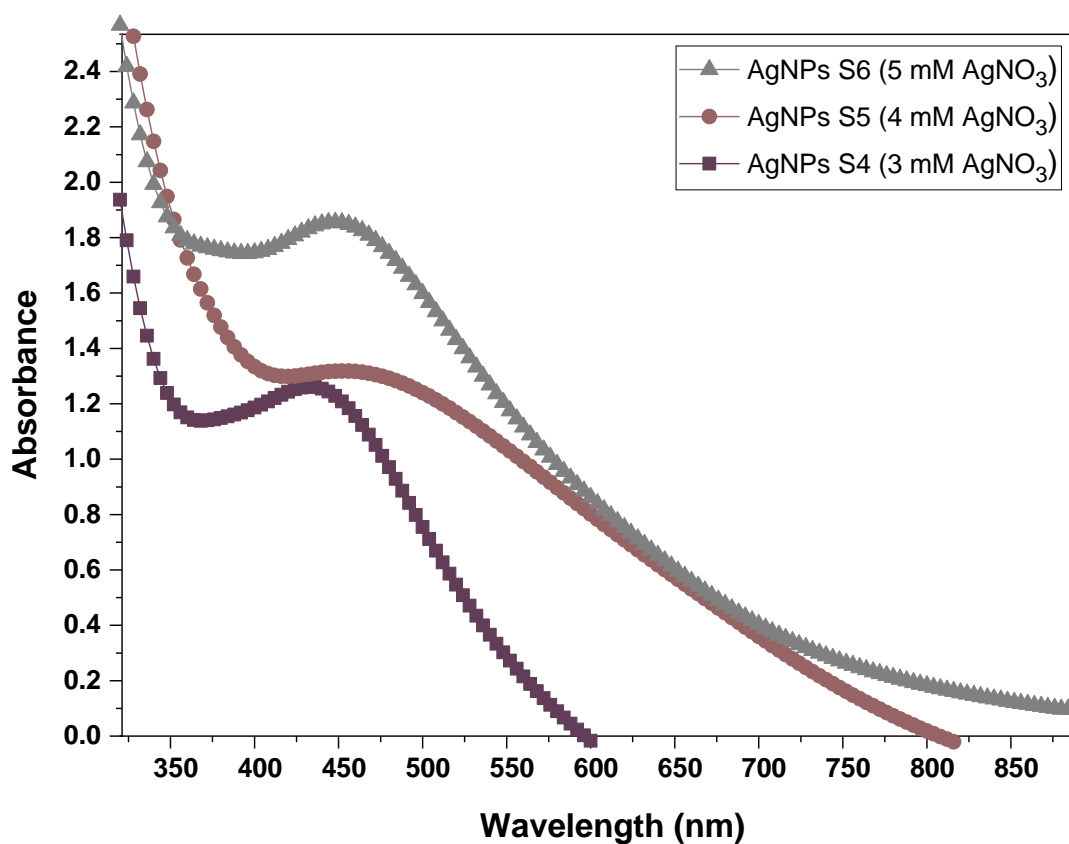


Figure 4.4: Ultraviolet-visible spectra of silver nanoparticles prepared by adding 200 ml with a different molar ratio of silver salt; S4 (3 mM), S5 (4 mM), and S6 (5 mM) with 40 ml lemon.

4.1.3 Ultraviolet-Visible Spectra of Iron Nanoparticles Prepared at Different Molarity of Iron Salt

Figure 4.5 shows the ultraviolet-visible spectra of iron samples prepared by using an equivalent amount of chitosan, *NaOH*, and ethanol with varying the molarity of iron salt ($Fe^{3+}: Fe^{2+}$) as a precursor, according to **Table 3.3**.

From depicted **Figure 4.5**, it is clear that the absorption peak of S7 appears at 336 nm, S8 has 340 nm, and S9 at 344 nm. The absorption peaks and changing in color indicate nanoparticle formation. This band is due to iron nanoparticle formation, which describes a resonance effect created as a result of interaction between incident photon and electron on the surface of iron nanoparticles. In these samples (S7 - S9) the band position was shifted to higher wavelength value with rising precursor amount ($Fe^{3+}: Fe^{2+}$), and the particle size becomes larger due to increasing ions in solution; this allows for more nucleation.

The decreasing in particle size with different concentrations of precursor, responsible for increasing optical band gap E_g , that means there are inversely relationship between bandgap E_g and particle size. Moreover, the absorbance intensity increased with increasing the ratio of ($Fe^{3+}: Fe^{2+}$), this increase follows Beer-Lambert $A = \epsilon cl$

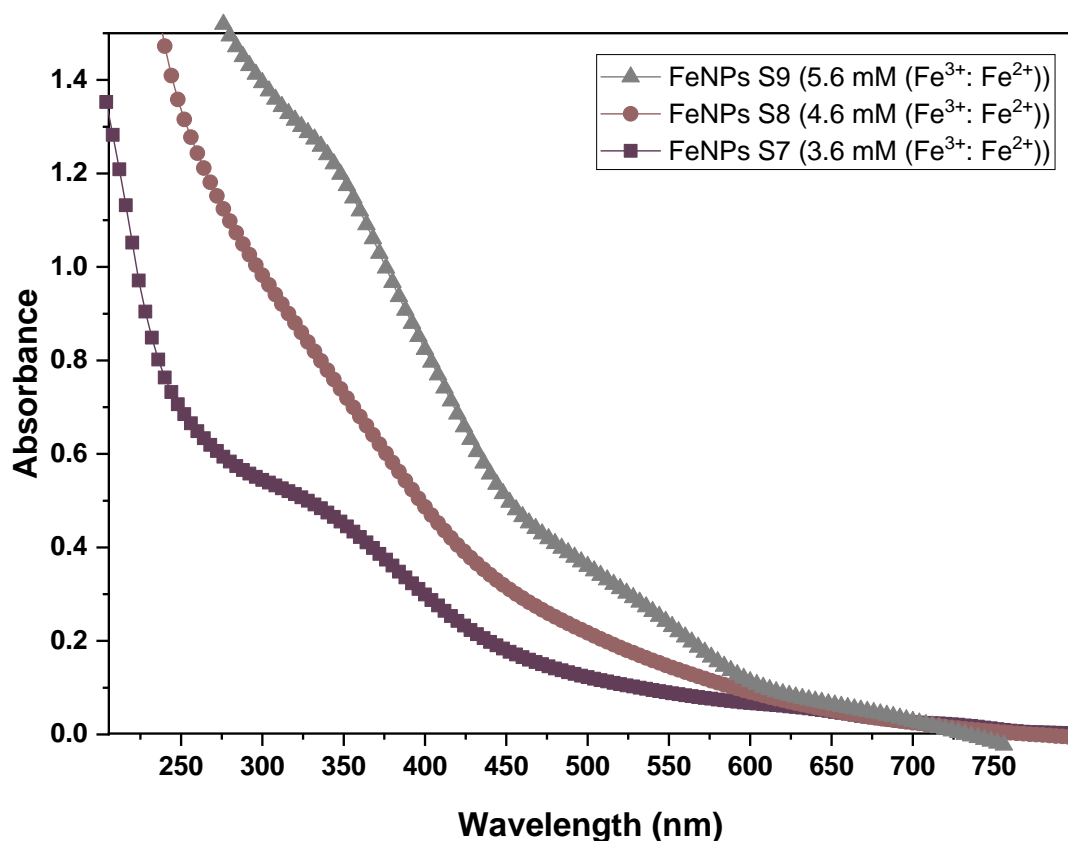


Figure 4.5: Ultraviolet-visible spectra of iron nanoparticles synthesized by adding a different molar ratio of iron salt ($Fe^{3+}: Fe^{2+}$); S7 (3.6 mM), S8 (4.6 mM), and S9 (5.6 mM) to 200 ml of prepared chitosan.

4.1.4 Ultraviolet-Visible Spectra of Cobalt Nanoparticles Prepared at Different Concentrations of Sodium Hydroxide

Figure 4.6 shows the absorption spectra of cobalt samples synthesized at a constant concentration of cobalt salt contrasting various ratios of sodium hydroxide where S10 (0.5 M), S11 (1.5 M), and S12 (2.5 M), as outlined in **Table 3.4**.

The absorbance spectra band that appears in the range of (520 nm – 550 nm) where S10 has 520 nm, S11 has 548 nm, and S12 appears at 528 nm; these bands

are confirmed cobalt nanoparticles formation which describes the surface plasmon resonance of CoNPs.

The observation of illustrated **Figure 4.6** shows the absorbance of cobalt nanoparticle solution in different intensity values scored as 0.185201, 0.63877, and 0.978720 for S10, S11, and S12, respectively. The rising in sodium hydroxide molarity has an influence increase in absorbance intensity, known as Beer-Lambert law. Briefly, there is a proportional relationship between concentration and intensity, as mentioned above.

Sample 10, which has 520 nm, displays the smallest nanoparticle size with a lower wavelength as a consequence of SPR that means it required high energy to complete excitation. Besides, the samples could obtain more and more redshift with an increase in *NaOH* ratio. However, an extra increase in reducing agents causes a decrease in wavelength intensity, the decreasing is due to convert nanoparticles into nanorod or nanofiber as S12 shows. Another wavelength that appeared after 550 nm is probably due to nonuniform shape formation.

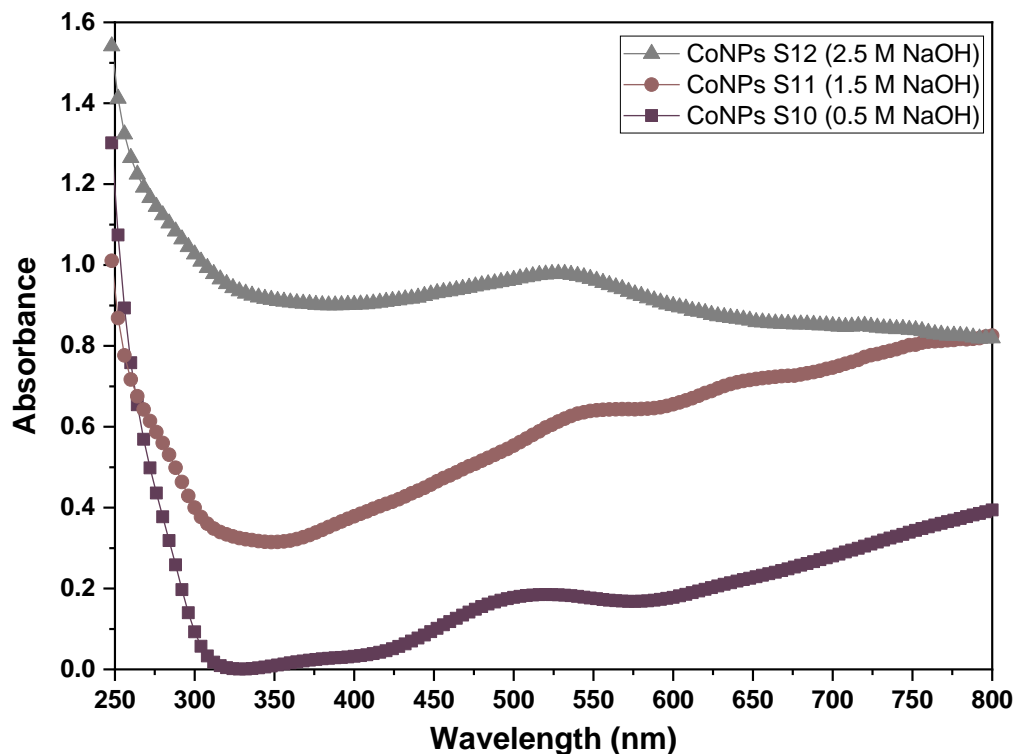


Figure 4.6: Ultraviolet-visible spectra of cobalt nanoparticles prepared by adding 200 ml with concentration (0.25 M) of cobalt salt in different molar ratio of NaOH; S10 (0.5 M), S11 (1.5 M), and S12 (2.5 M).

4.2 High-Resolution Transmission Electron Microscopy

4.2.1 HR-Transmission Electron Microscopy of Gold Nanoparticles Prepared at Different Concentrations of Lemon Extract

Figure 4.7 visualizes HR-TEM results of gold nanoparticles which synthesized via adding a different quantity of lemon extract 4 ml, 5 ml, and 6 ml for samples S1, S2, and S3, respectively with a fixed concentration of gold salt $\text{HAuCl}_4 \cdot \text{H}_2\text{O}$, as shown in **Table 3.1**.

From **Figure 4.7**, it is clear that the morphology of S1 consists of a mixture shape, for example, triangle, hexagonal, trapezoid, and spherical particles with some

aggregation of nanoparticle also appeared. The nanosphere was measured in range 40 ~ 80 nm with average particle size 54 nm, according to Gaussian distribution illustrated at opposite HR-TEM image of S1.

The transmission electron microscope result of S2 as shown in **Figure 4.7** which represent a random distribution of gold nanoparticle with various geometrical shape comprise from prism, hexagonal, rectangular, sphere, small rod, and oval. The most frequent were shaped spherically with an average diameter of 22 nm; the particle size fluctuates around 16 ~ 34 nm according to Gaussian distribution plotted at opposite of HR-TEM image of S2.

Figure 4.7 depicts the visual representation of HR-TEM for S3. It is clear from the result that AuNPs have a spherical shape with other nonuniform particles such as a prism, small rod, hexagonal, and pentagon. The average size of spherical particle is 28 nm with a fluctuant diameter of around 20 ~ 37 nm according to Gaussian distribution depicted at opposite of HR-TEM image of S3.

Overall, the result of HR-TEM of gold nanoparticle samples (S1 - S3) has a compatible visualization image with a similar geometric shape. Especially relevant, the average particle size was calculated from the relation between abundant sphere particle in image. The HR-TEM of gold nanoparticles samples notified that the result of S1 and S3 agrees with UV results except S2; This may be owing to the different shapes of the image beside the spherical shape for S2.

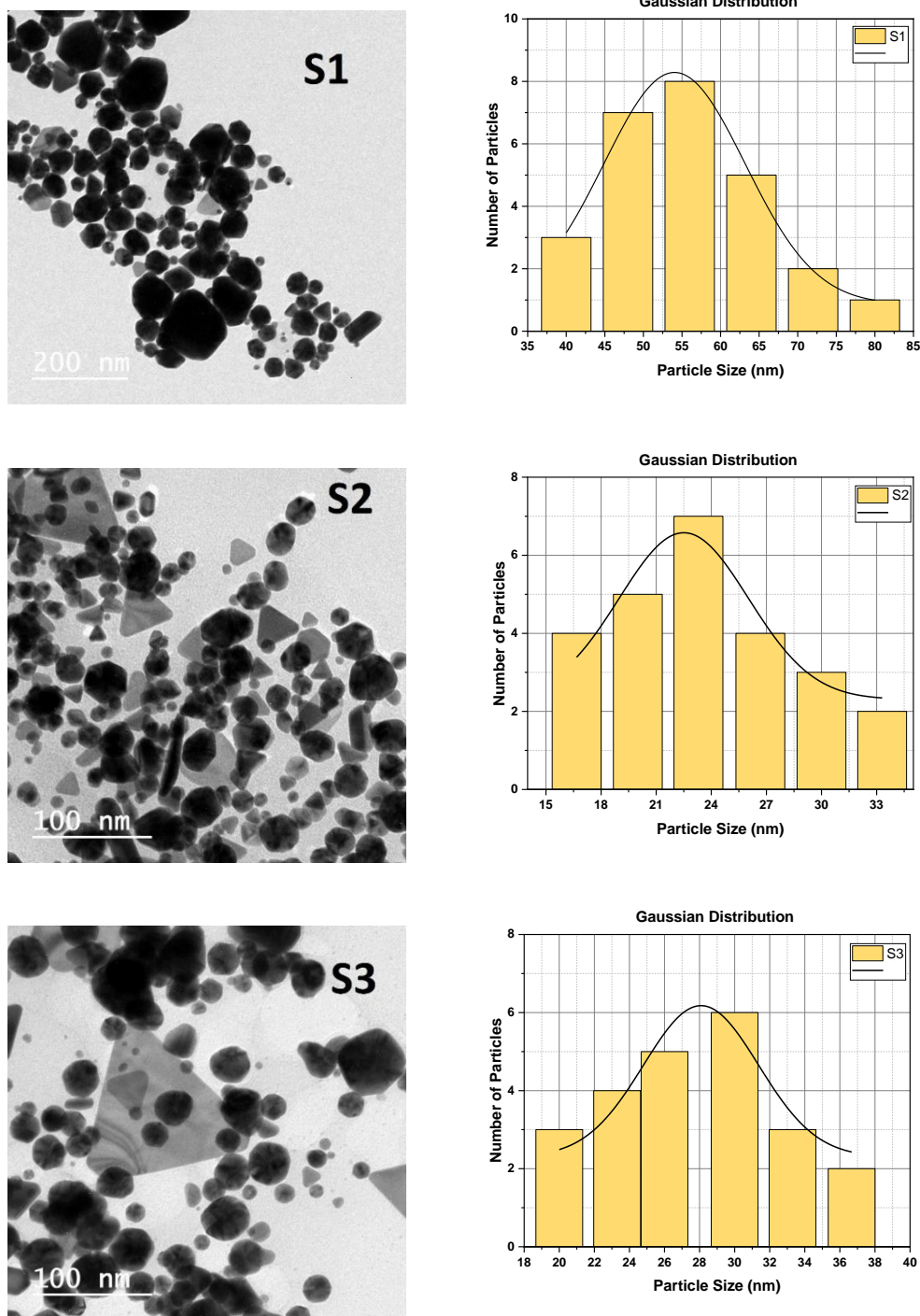


Figure 4.7: High-Resolution transmission electron microscopy images of gold nanoparticles prepared by adding 10 ml with concentration ($5.589 \times 10^{-3} M$) of gold salt to a different molar ratio of lemon extract S1 (4 ml), S2 (5 ml), and S3 (6 ml) and their Gaussian distribution particle size.

4.2.2 HR-Transmission Electron Microscopy of Silver Nanoparticles Prepared at Different Molar Ratio of Silver Nitrate

Figure 4.8 illustrates visualization image of HR-TEM for silver nanoparticles prepared at different concentrations of silver nitrate and constant concentrations of both sodium dodecyl sulphate and lemon; where the amount $AgNO_3$ were 3 mM for S4, 4 mM for S5, and 5 mM for S6, as outlined in **Table 3.2**.

Sample S4 which has 3 mM, shows the average diameter of spherical AgNPs was about 23 ~ 43 nm as plotted in Gaussian distribution at opposite of HR-TEM of S4. It can be seen from **Figure 4.8** that the image displays the most particles as a spherical shape with smooth edges and an average size of about 31 nm. Also, it has some ellipsoidal with compact aggregation.

It is clear that from **Figure 4.8**, sample S5 (4 mM) has a random distribution of silver nanoparticles; it also has a spherical shape and some oval with smooth edges. The particle size in this sample fluctuated around 8 ~ 20 nm with a 15 nm average size as represented in Gaussian distribution Figure at opposite HR-TEM image of S5.

HR-TEM image of sample S6, which has 6 mM illustrated in **Figure 4.8**, has spherical, hexahedral, and ellipsoidal silver nanoparticles. The majority of AgNPs were in the range between 13 ~ 37 nm with an average size of 28 nm as shown in Gaussian distribution Figure at opposite of HR-TEM image of S6.

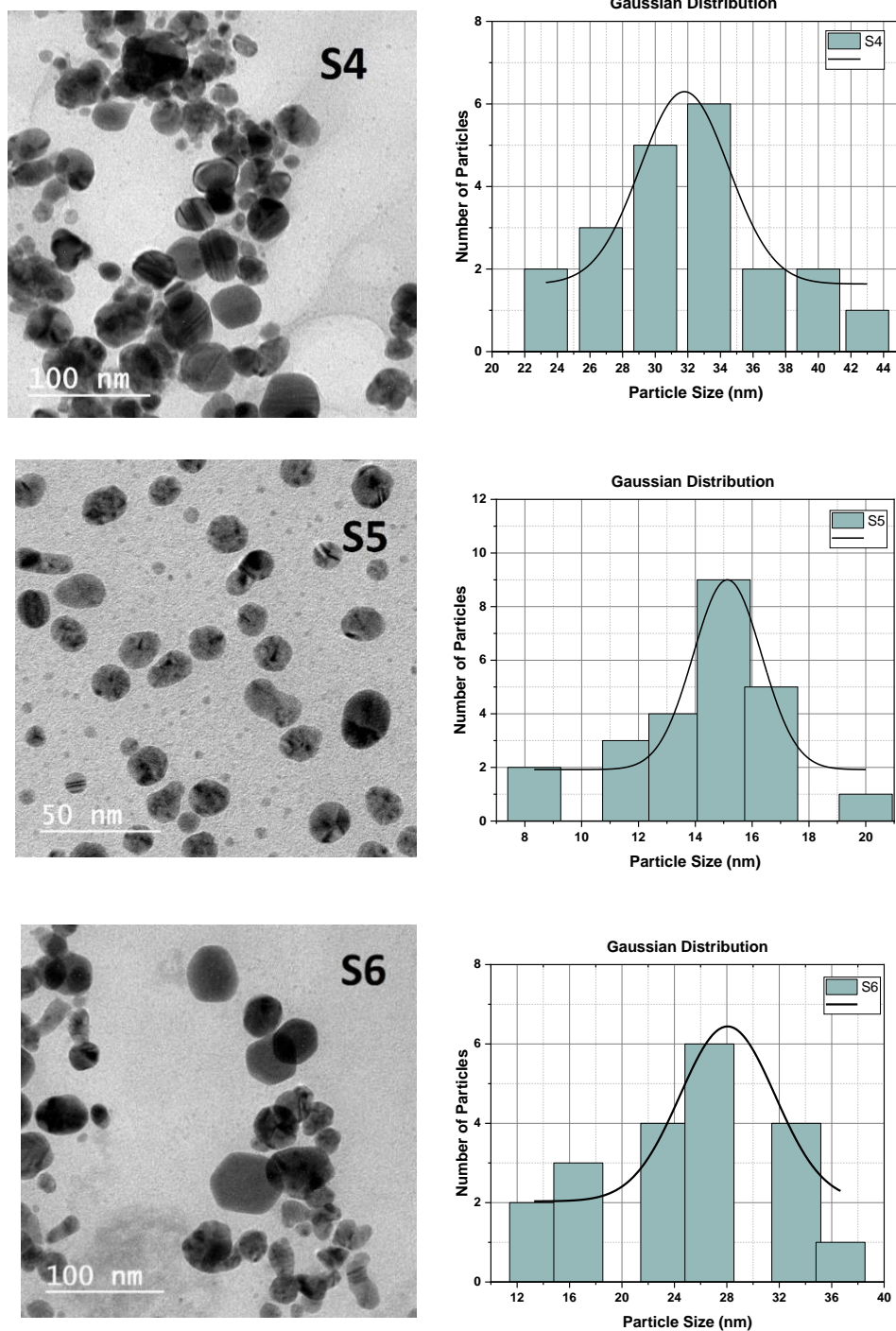


Figure 4.8: High-Resolution transmission electron microscopy images of silver nanoparticles prepared by adding 200 ml with a different molar ratio of silver salt; S4 (3 mM), S5 (4 mM), and S6 (5 mM) with 40 ml lemon extract and their Gaussian distribution particle size.

In conclusion, HR-TEM analysis demonstrated the silver nanoparticle result in **Figure 4.8**; it displays the most of anisotropic nanostructure has spherical shape comparing with other geometrical shapes. First and foremost, the average size of particle was calculated from the relationship between repeated sphere particles in the same size of sample. Moreover, The result of HR-TEM is incompatible with surface plasmon band position of UV-Vis data may be due to some aggregation was happened in AgNPs during TEM measurement.

4.2.3 HR-Transmission Electron Microscopy of Iron Nanoparticles Prepared at Different Molarity of Iron Salt

Figure 4.9 summarizes all measurement results of HR-TEM analysis for chitosan-coated magnetic nanoparticles for (S7a - S9a) after drying which had synthesized by co-precipitation of iron salt (Fe^{3+} : Fe^{2+}) in chitosan polymer with $NaOH$ and ethanol according to **Table 3.3**

The morphology of sample S7a was demonstrated in **Figure 4.9** shows that the particle shape looked like a collective with some spherical and other irregular shapes. The average particle size estimated at 22 nm, with a range of 12 ~ 31 nm, as illustrated in Gaussian histogram distribution at opposite of HR-TEM image of S7a.

On the other hand, sample S8a in **Figure 4.9** represents a random distribution of FeNPs with a different shape. For instance, rectangle, sphere, and other non-uniform shapes were observed. This sample has a fluctuated diameter of around 4 ~ 31 nm, with an average size of about 17 nm, as shown in Gaussian histogram distribution at opposite of HR-TEM image of S8a.

It is clear that from **Figure 4.9** sample S9a that FeNPs show homogenous particles with few spherical shapes in some regions and aggregation in other

domains. The average particle size that calculated from Gaussian distribution of this sample was observed at 32 nm with a range of 24 ~ 43 nm according to Gaussian histogram distribution located at opposite of HR-TEM image of S9a.

Last of all, most of these samples of FeNPs present agglomeration in some regions and homogenous nanoparticles in other regions. Besides, the spherical shape is seen at Gaussian histogram distribution. Should be noted, Gaussian histogram distribution of mentioned samples was measured using Image J program.

Figure 4.10 represents HR-TEM of magnetic iron nanoparticles capped by chitosan for samples (S7b - S9b) before drying which synthesized by coprecipitation of iron salts ($Fe^{3+}: Fe^{2+}$) in chitosan polymer with *NaOH* and ethanol according to **Table 3.3**.

It is clear from illustrated **Figure 4.10** that the FeNPs sample S7b (3.6 mM) of ($Fe^{3+}: Fe^{2+}$) has a random distribution for particles with various sizes and shapes. The average diameter of spherical shape was found at about 10 nm, with a range of 5 ~ 18 nm as represented in Gaussian histogram distribution at opposite of HR-TEM of S7b.

Samples S8b which has 4.6 mM of ($Fe^{3+}: Fe^{2+}$) in **Figure 4.10** presents FeNPs as agglomeration particles in different groups including different shapes such as rectangular, spherical, and irregular nanostructures. Moreover, the particle size fluctuated around 5 ~ 20 nm with an average of 9 nm, as observed in Gaussian histogram distribution at opposite of HR-TEM image of S8b.

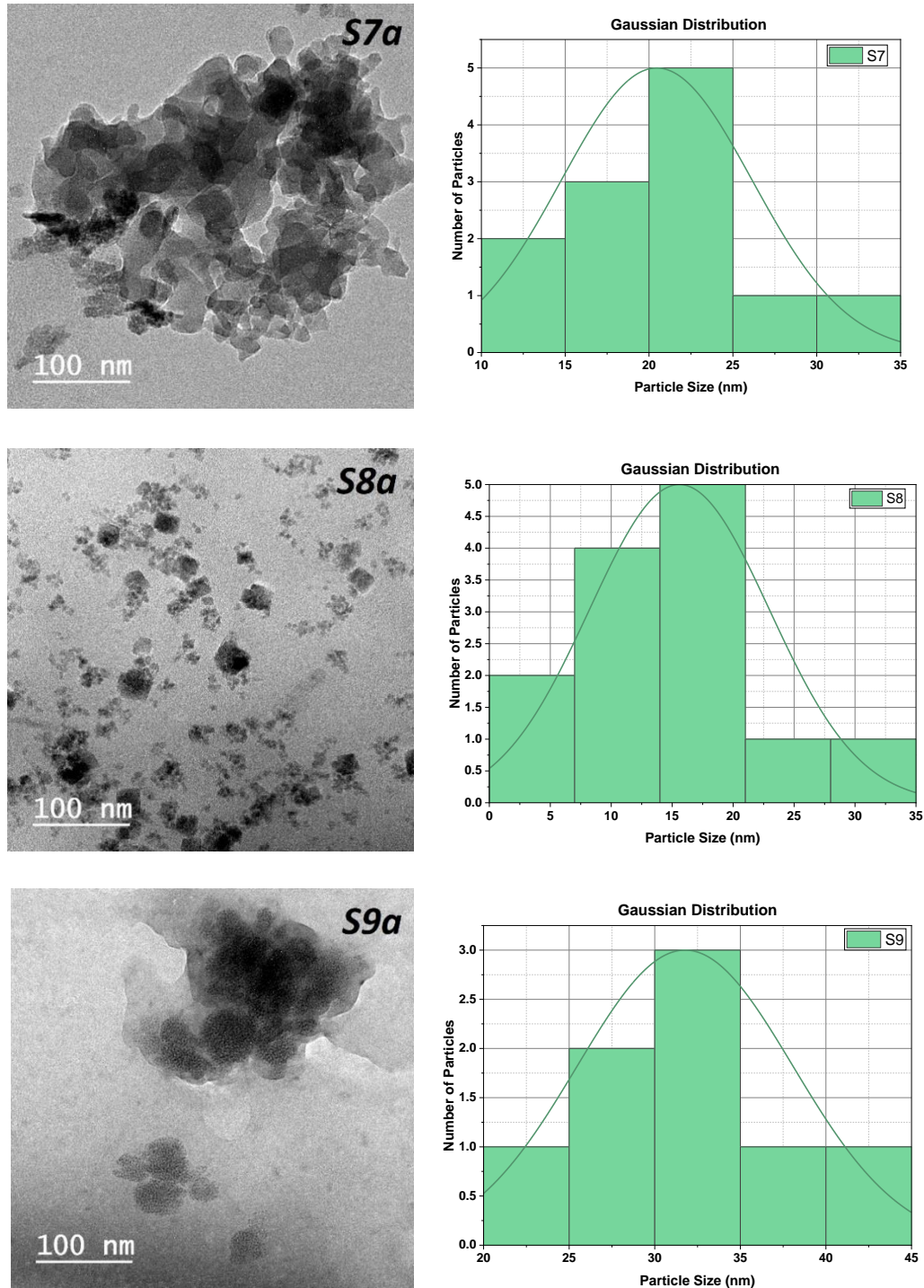


Figure 4.9: High-Resolution transmission electron microscopy images of iron nanoparticles synthesized by adding a different molar ratio of iron salt (Fe^{3+} : Fe^{2+}) after drying; S7a (3.6 mM), S8a (4.6 mM), and S9a (5.6 mM) into 200 ml of prepared chitosan and their Gaussian histogram distribution particle size.

The visualization result depicted in **Figure 4.10** of sample S9b represents iron nanoparticle which has 5.6 mM of (Fe^{3+} : Fe^{2+}). As seen in this Figure, the sample has spherical particles with other nonuniform formation in the middle of image. Furthermore, the average particle size was determined and found to be 18 nm with fluctuation between 11 ~ 27 nm, according to Gaussian histogram distribution at opposite of HR-TEM of S9b.

However, FeNPs samples (S7b - S9b) has spherical nanoparticle shape it also has irregular nanostructure form. The average diameter of spherical shape was observed in Gaussian histogram distribution of the same image. Important to note, the Gaussian histogram distribution of all above samples was measured via Image J program.

By comparing the TEM image of iron nanoparticles before and after drying, it noted that the particle size was increased after drying this probably due to the aggregation of some iron NPs after heating has happened.

4.2.4 HR-Transmission Electron Microscopy of Cobalt Nanoparticles Prepared at Different Concentrations of Sodium Hydroxide

Figure 4.11 visualizes HR-TEM image of cobalt nanoparticles, which synthesized at a constant concentration of cobalt salt with varying sodium hydroxide ratio as 0.5 M, 1.5 M, and 2.5 M for S10, S11, and S12 respectively, as outlined in **Table 3.4**.

From **Figure 4.11**, it is clear that the morphology of CoNPs S10 comprises of mixture geometrical shapes such as ellipsoidal, pentagonal, spherical, and hexagonal with some agglomeration particles. The majority of CoNPs in spherical shapes were fluctuated in a range of 15 ~ 37 nm with an average particle size 27 nm according to Gaussian distribution, as shown on the right side.

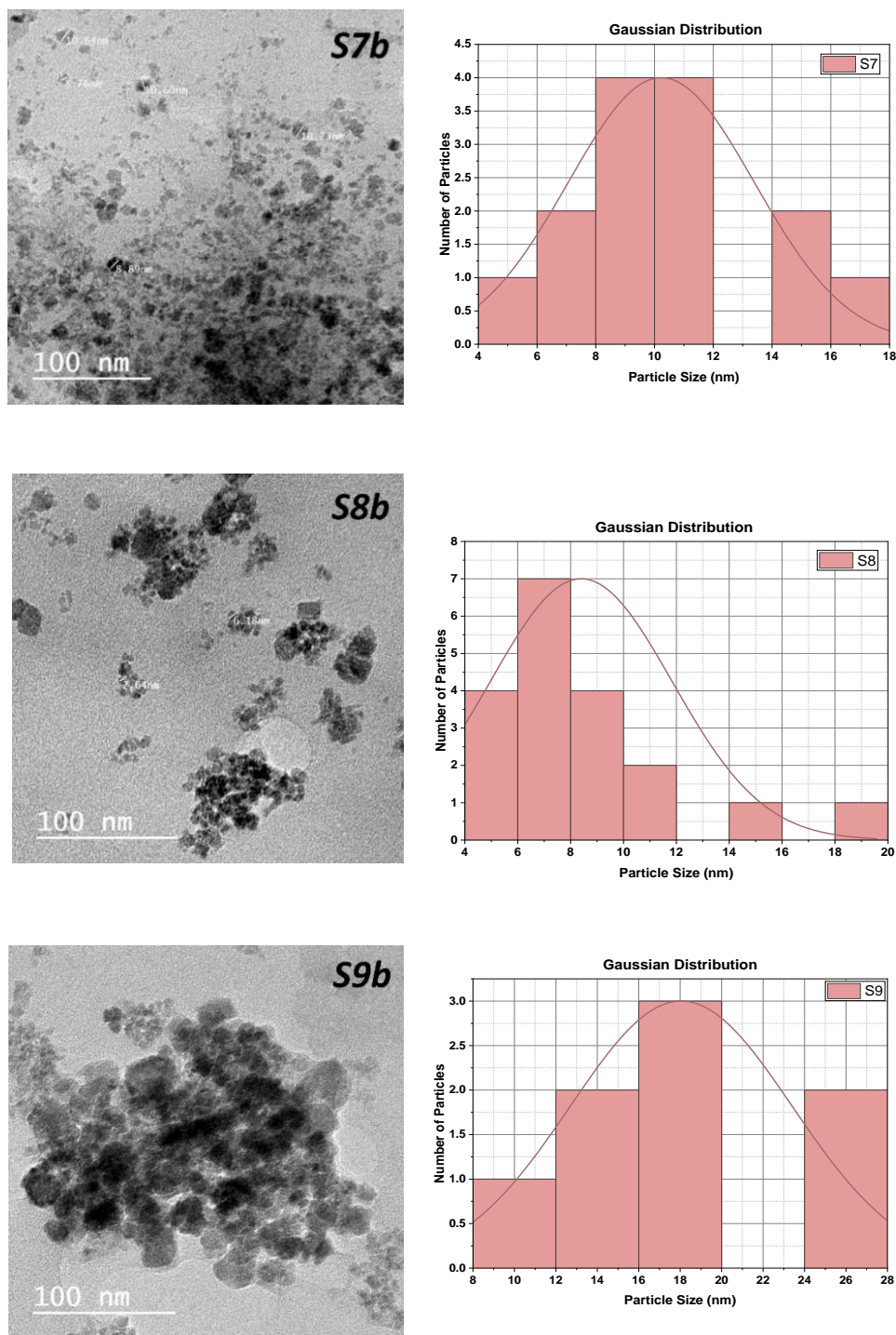


Figure 4.10: High-Resolution transmission electron microscopy images of iron nanoparticles synthesized by adding a different molar ratio of iron salt (Fe^{3+} : Fe^{2+}) before drying; S7b (3.6 mM), S8b (4.6 mM), and S9b (5.6 mM) into 200 ml of prepared chitosan and their Gaussian histogram distribution particle size.

As can be seen from **Figure 4.11** of CoNPs, S11 has formed as a nanorod with other ambiguous particles. The nanorod has an aspect ratio between 5.2 ~ 8.5 nm. On the contrary, CoNPs S12 appeared almost as nanofiber and some nanorod with an aspect ratio between 5.6 ~ 8.33 nm. To sum up, it is clear that the sample S10 has various geometric shapes comparing with sample S11 and S12; it almost does not have spherical shapes that why the Gaussian distribution ignored in both samples.

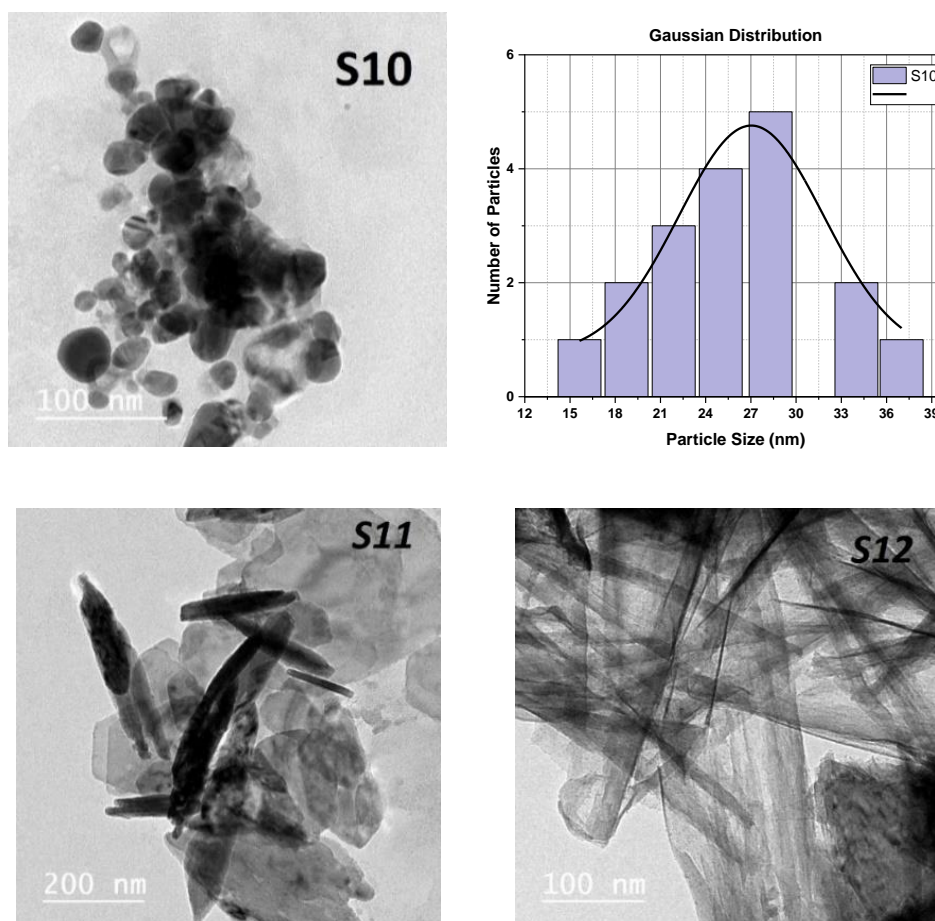


Figure 4.11: High-Resolution transmission electron microscope images of cobalt nanoparticles prepared by adding 200 ml (0.25 M) of cobalt salt with a different molar ratio of NaOH; S10 (0.5 M) and its Gaussian distribution, S11 (1.5 M), and S12 (2.5 M).

4.3 X-Ray Diffraction Pattern

4.3.1 X-Ray Diffraction for Iron Nanoparticle Prepared at Different Concentrations of Iron Salt

Figure 4.12 shows XRD pattern of iron nanoparticles sample (S7 - S9) that formed by using a various amount of iron salt (Fe^{3+} : Fe^{2+}) and an equivalent amount of chitosan polymer, $NaOH$, and ethanol, according to **Table 3.3**. All samples were measured in $2\theta^\circ$ with a range between ($25^\circ \sim 60^\circ$).

From illustrated **Figure 4.12** it can be seen that the sample S7 (3.6 mM of iron salt) has a Bragg diffraction peak at 35.73° , 41.1° , and 54.6° in $2\theta^\circ$ angle with relative planes assigned at (220), (311), and (422), respectively. This result is agreement with data mentioned in card (JCPDS card No. 65-3107) [121]. The average crystalline size was calculated via Scherrer's equation **Eq. 2.19** which is

$$D = \frac{k\lambda}{\beta \cos \theta}$$

Where D represents the average crystal size, k is Scherrer constant for spherical particles equal (0.9), λ is x-ray wavelength (0.1540562 nm), while β refers to the full width at half maximum (FWHM) of diffraction peaks [98, 99].

The estimated value of crystal size found to be 41.7 nm, 28.3 nm, and 44.6 nm for $2\theta^\circ$ at 35.73° , 41.1° , and 54.6° with an average crystal size of 38.2 nm.

On the other hand, sample S8 (4.6 mM of iron salt) has diffraction peaks that appeared at 35.35° , 41° , and 54.35° in $2\theta^\circ$ angle with different intensities and matched planes at (311), (400), and (422). The crystalline size was calculated for the three peaks and determined as 23.8 nm, 33.9 nm, and 44.6 nm at the same angle of $2\theta^\circ$, respectively with an average crystal size 34.1 nm.

It is clear that sample S9 (5.6 mM of iron salt) has a Bragg diffraction peaks with different intensities assigned at 31.2° , 36.1° , and 41.25° in $2\theta^\circ$ degree which corresponds to the planes (220), (311), and (400); its relevant particle size found to be 82.4 nm, 41.7 nm, and 24.2 nm with 49.5 nm of average crystal size.

Overall, the diffraction pattern result characterized all above samples as a major of Fe_3O_4 and minor Fe_2O_3 with cubic structure, as reported by Díaz-Hernández et al. [69]; besides, it shows an agreement with card (JCPDS file No. 65-3107) as demonstrated in [121]. By comparing the diffraction pattern of S7 and S8 with S9, which plotted in **Figure 4.12**, it can be noted that S9 has clear and sharp peaks with more intensity; it might be due to the difference in crystalline size which caused by increasing the iron salt. Notwithstanding, the peaks that have a plane (422) in S9 is not much clear as S7 and S8 it probably owing to the sharp peak in some region of S9. Strongly enough, sample S9 had the largest size either in TEM or in XRD than other samples.

4.3.2 X-Ray Diffraction of Cobalt Nanoparticles Prepared at Different Concentrations of Sodium Hydroxide

Figure 4.13 represents x-ray diffraction pattern of cobalt nanoparticle prepared at a fixed amount of cobalt salt and varying concentration of sodium hydroxide as listed in **Table 3.4**. All samples were measured in $2\theta^\circ$ with a range between ($30^\circ \sim 60^\circ$).

It is clear from depicted **Figure 4.13** that, the diffraction pattern of sample S10 (0.5 M $NaOH$) has four recorded peaks at $2\theta^\circ = 32.5^\circ$, 38° , 51.4° , and 58.05° which correspond to (100), (101), (102), and (110) diffraction planes. The obtained peak is well-matched with standard JCPDS card No. 30-0443 for $Co(OH)_2$ as reported by Si et al., [122]. The crystal size of NPs was determined by using

Scherrer's formula $D = 0.9\lambda/\beta\cos\theta$ and it found to be 39.5 nm, 30.96 nm, 26.8 nm, and 34.2 nm in $2\theta^\circ$ angle with an average crystalline size 32.9 nm.

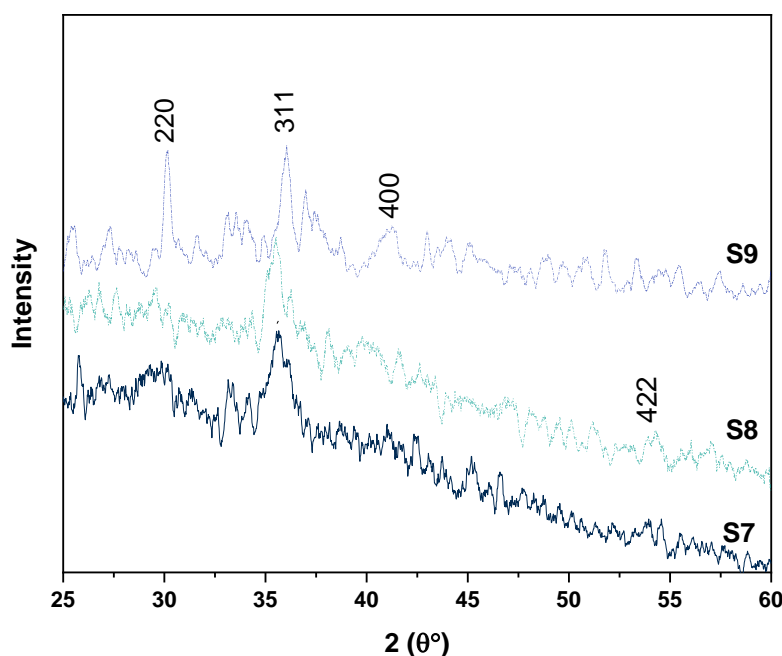


Figure 4.12: X-ray diffraction pattern for iron nanoparticles synthesized by adding a different molar ratio of iron salt ($Fe^{3+} : Fe^{2+}$); S7 (3.6 mM), S8 (4.6 mM), and S9 (5.6 mM) to 200 ml of prepared chitosan.

Figure 4.13 demonstrates sample S11 (1.5 M of $NaOH$), as seen in Figure has five diffraction peaks in $2\theta^\circ$ appeared at 32.6° , 34.6° , 38° , 51.5° , and 58.04° in different intensities. It's related to diffraction planes (100), (220), (101), (102), and (110), respectively. The diffraction pattern was similar to the Bragg reflection of $Co(OH)_2$ it also compatible with JCPDS card No. 30-0443. The crystalline sizes of $Co(OH)_2$ were obtained as 40.9 nm, 26.5 nm, 30.1 nm, 24.7 nm, and 34.2 nm with an average crystal size 31.3 nm.

The X-ray diffraction pattern of sample S12 which has (2.5 M of $NaOH$) as plotted in **Figure 4.13**, shown that the cobalt nanoparticle has several peaks with different intensities assigned at $2\theta^\circ$ which are 32.6° , 34.7° , 38.09° , 51.5° , and 58.1°

with corresponding index (100), (220), (101), (102), and (110). The particle size of FeNPs estimated as 57.6 nm, 20.6 nm, 47.1 nm, 42.7 nm, and 39.5 nm, respectively. It has 41.5 nm average crystalline size.

Briefly, **Figure 4.13** suggests that the cobalt nanoparticle has several sharp peaks in different intensities at $2\theta^\circ$ angle in a range of $30^\circ \sim 60^\circ$. Furthermore, all samples are confirmed by JCPDS card No. 30-0443, as reported by Si et al., [122]. The X-ray result proposed that, S10 have a low-intensity peak in $2\theta^\circ = 35^\circ$ despite S11 has diffraction peak in the same region and then in S12 the peak appears as more sharp and obvious; it could be interpreted as an increase in sodium hydroxide concentration lead to peak appear more and sharper. Furthermore, there is a slightly shifted peak in cobalt nanoparticle sample such as in S10 ($2\theta^\circ = 51.44^\circ$), S11($2\theta^\circ = 51.48^\circ$), and in S12 ($2\theta^\circ = 51.44^\circ$) and so on.

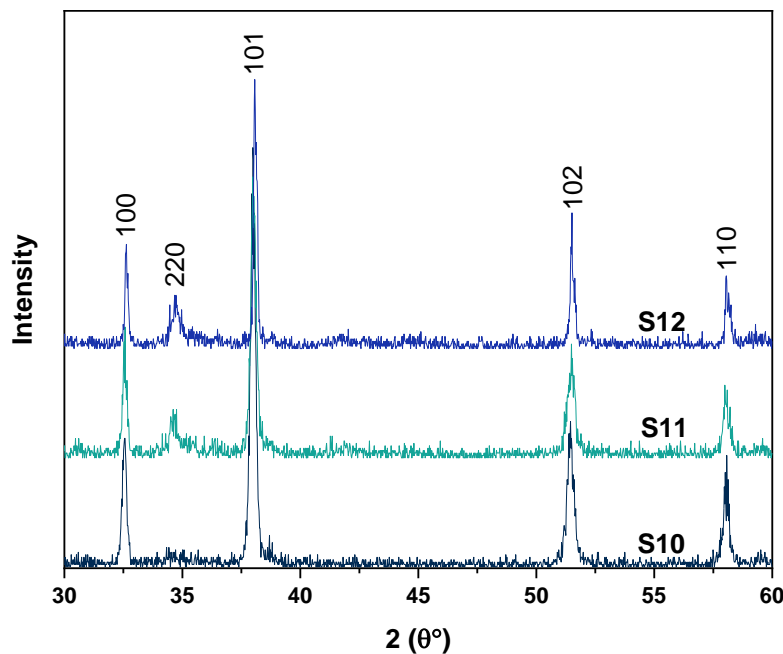


Figure 4.13: X-ray diffraction pattern of cobalt nanoparticles prepared by adding 200 ml with concentration (0.25 M) of cobalt salt with a different molar ratio of NaOH; S10 (0.5 M), S11 (1.5 M), and S12 (2.5 M).

4.4 Fourier Transform Infrared Spectroscopy

4.4.1 Fourier Transform Infrared Spectroscopy of Gold Nanoparticle Capped with Different Concentrations of Lemon Extract

The FTIR of lemon extract was measured in the wavenumber range from 4000 cm^{-1} to 400 cm^{-1} by Acheampong, Okyem et al. [123]. The absorbance with broadening band observed at 3332 cm^{-1} represents the stretching vibration of hydroxide group O – H in lemon extract, as shown in **Figure 4.14** it could be also interpreted as O – H for water that absorbed from air of spectrum measurement. The peak at 2924 cm^{-1} is assigned to symmetric and asymmetric stretching vibrations of C – H group. Moreover, the band at wavenumber 1621 cm^{-1} is represented C = O while the band at 1237 cm^{-1} is explained C – O stretching vibration. Eventually, the located peak at wavenumber 1017 cm^{-1} is referring to C – C stretching vibration.

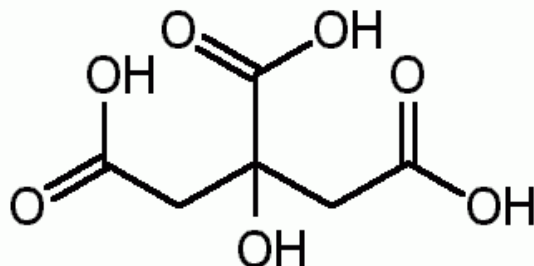


Figure 4.14: Chemical structure of lemon extract.

Figure 4.15 illustrates FTIR of gold nanoparticle prepared at a constant concentration of gold salt and varying quantity of lemon extract where S1(4 ml), S2 (5 ml), and S3 (6 ml) according to **Table 3.1**. The IR spectra were recorded in range 4000 cm^{-1} – 400 cm^{-1} .

From depicted **Figure 4.15**, it noted that absorption with a strong and broadening band was appeared at about wavenumber 3433 cm^{-1} . This band is related

to O – H stretching vibration of in lemon extract, as shown in structure **Figure 4.14**; it also indicates of presence amount of water molecules in the samples during measurement [124]. The located band at around 2924 cm⁻¹ and 2840 cm⁻¹ could be assigned to asymmetric and symmetric C – H stretching vibration bond [123].

Furthermore, the typical peak at about 1633 cm⁻¹ attributed to C = O stretching of a carbonyl group in citrus lemon [125]. By comparing the C = O band position of our prepared samples with Acheampong et al. [123], it can be noted that this band was shifted to higher wavenumber in our samples. This might be owing to AuNPs could be coordinated with oxygen atom in C = O due to the lone pair of electrons in oxygen atoms. Besides, the band at 1047 cm⁻¹ may be appeared due to C – C or C – O stretching [123]. An observed peak at around 500 cm⁻¹ is relative to gold-oxygen stretching vibration of AuNPs [126]. **Table 4.1** outlines the absorbance bands and their assignments of samples (S1 – S3).

The stretching vibration of Au – O was theoretically calculated and it could be 757.04 cm⁻¹ using $\bar{\nu} = \frac{1}{2\pi c} \sqrt{\frac{k}{\mu}}$. This law was explained in detail in section (2.5.3). The slight difference in theoretical and practical results could interpreted as consequence of presence gold nanoparticles to be coordinated with other functional groups in the sample.

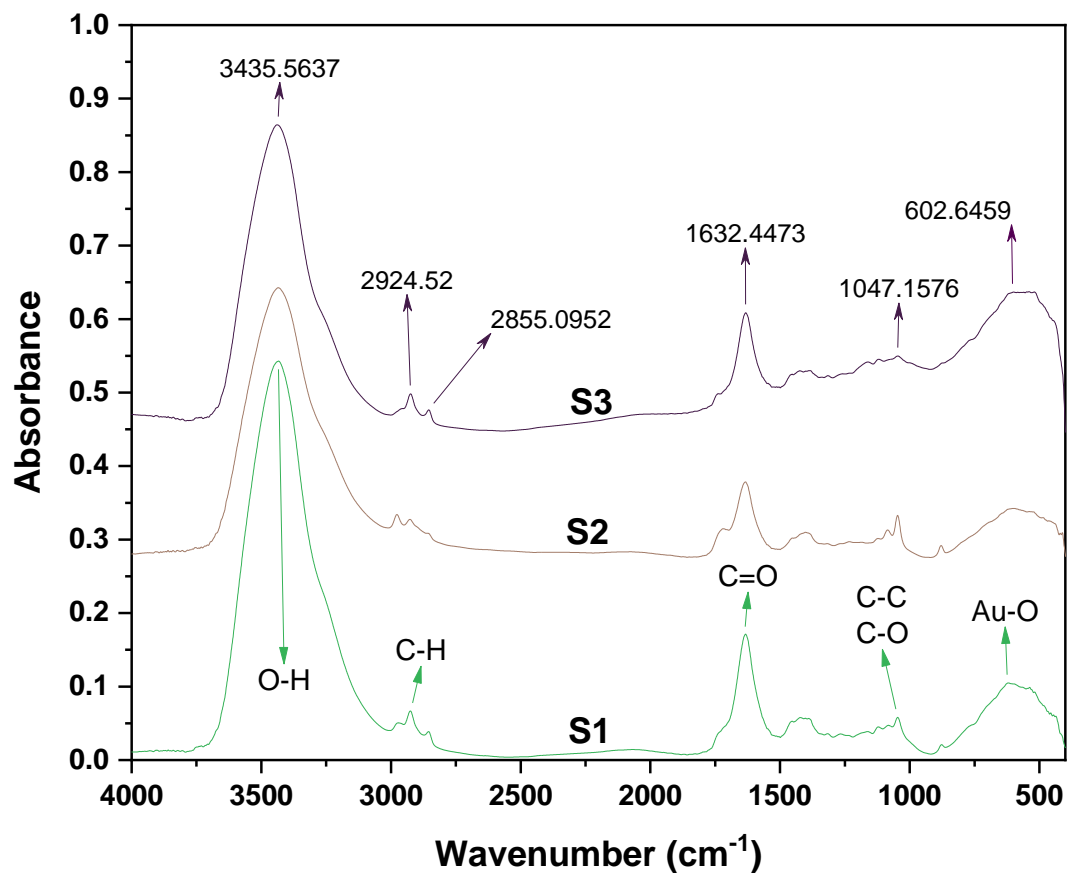


Figure 4.15: Fourier transforms infrared spectroscopy (FTIR) of gold nanoparticles prepared by adding 10 ml with concentration ($5.589 \times 10^{-3} M$) of gold salt with a different molar ratio of lemon extract; S1 (4 ml), S2 (5 ml), and S3 (6 ml).

Table 4.1: Positions of FTIR absorption peaks and their assignment functional groups for gold nanoparticle capped by lemon extract samples (S1 – S3).

Wavenumber (cm ⁻¹)			Assignments
S1	S2	S3	
3433	3435	3435	O – H stretching vibration
2925	2977	2924	C – H asymmetrical stretching vibration
2855	2927	2855	C – H symmetrical stretching vibration
1632	1633	1632	C = O Carbonyl group
1046	1047	1047	C – O, C – C stretching vibration
621	609	602	Au – O stretching vibration

4.4.2 Fourier Transform Infrared Spectroscopy of Silver Nanoparticle Capped by Lemon Extract

The absorbance spectrum of lemon extract, which explained in first part of section (4.4.1), was compared with FTIR spectra of silver nanoparticle capped by lemon prepared at different concentrations of silver nitrate according to **Table 3.2**, as illustrated in **Figure 4.16**.

It is clear from **Figure 4.16** that the absorption band appeared at about 3332 cm⁻¹ that assigned to O – H of lemon was shifted to low wavenumber in silver nanoparticle capped lemon samples, which is 3403 cm⁻¹ in S4, 3415 cm⁻¹ in S5, and

3402 cm^{-1} in S6. The bands are increasing or decreasing due to the hydroxyl group in a component of lemon and water humidity in samples or may be due to the change of electrostatic negativity in C – OH. Moreover, the previous peak in sample S4 has a sharper peak with more intensity band and split into two peaks, which is 3470 cm^{-1} and 3403 cm^{-1} as a consequence of decreasing silver nitrate ratio.

The characteristic band of C – H asymmetric stretching that noted at exactly 2924 cm^{-1} in lemon FTIR has no longer shifted in sample S5, and S6 appeared at 2923 cm^{-1} for both samples. However, it shifted to higher wavenumber in S4, noticed at 2931 cm^{-1} . On the other hand, the C – H symmetric stretching band that recorded at 2853 cm^{-1} shown slightly shifted in the whole silver nanoparticle samples, which is 2854 cm^{-1} for S4, 2857 cm^{-1} for S5, and 2856 cm^{-1} for S6. The symmetric and asymmetric band is proved that the sample indeed has a C – H stretching vibrations bond. All these changes and shifts of the O – H group and C – H bands may be owing to the change of the AgNO_3 ratio that made small affected on the electrostatic negativity in the structure of our prepared samples.

The absorption band which appeared at 1730 cm^{-1} for lemon is corresponding to C = O stretching vibration related to carbonyl group while in sample S4, S5, and S6; this band is shifted to 1642 cm^{-1} , 1633 cm^{-1} , and 1648 cm^{-1} , respectively. These change into lower wavenumber is due to silver nanoparticles may be contributed with an oxygen atom in C = O carbonyl group. The band appeared at about 1387 cm^{-1} , 1391 cm^{-1} , and 1392 cm^{-1} for samples S4, S5, and S6, respectively is assigned to C – H bending vibration. There are absorption bands about 500 cm^{-1} , probably explained Ag – O peaks in a compound. **Table 4.2** summarizes the absorbance bands and their assignments of samples (S4 – S6).

The stretching vibration of Ag – O was theoretically calculated and it could be 778.86 cm^{-1} . The slight difference in theoretical and experimental results could be interpreted as a consequence of presence silver nanoparticles to be coordinated with other functional groups in the sample.

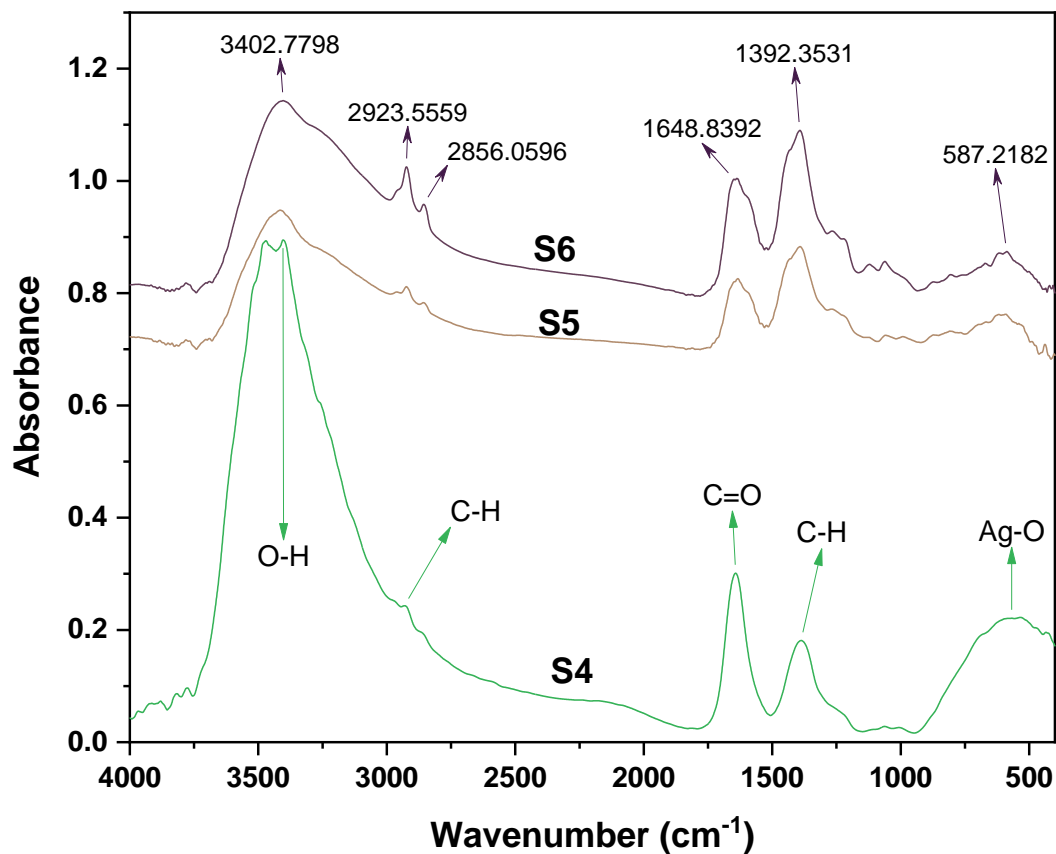


Figure 4.16: Fourier transforms infrared spectroscopy (FTIR) of synthesized silver nanoparticles by adding 200 ml with a different molar ratio of silver salt; S4 (3 mM), S5 (4 mM), and S6 (5 mM) with 40 ml lemon extract.

Table 4.2: Positions of FTIR absorption peaks and their assignment functional groups for silver nanoparticle capped by lemon extract samples (S4 – S6).

Wavenumber (cm ⁻¹)			Assignments
S4	S5	S6	
3470 3403	3415	3402	O – H stretching vibration
2931	2923	2923	C – H asymmetrical stretching
2845	2857	2856	C – H symmetrical stretching
1642	1633	1648	C = O carbonyl group
1387	1391	1392	C – H bending vibration
567	592	587	Ag – O stretching vibration

4.4.3 Fourier Transform Infrared Spectroscopy of Iron Nanoparticle Prepared at Different Concentrations of Ion Salt

Figure 4.17 displays FTIR spectra of iron nanoparticle encapsulated with chitosan synthesized at different concentrations of iron salt (Fe^{3+} : Fe^{2+}) according to **Table 3.3** in the range 4000 cm⁻¹ to 400 cm⁻¹.

The absorption bands appeared at 3433 cm⁻¹, 3432 cm⁻¹, and 3433 cm⁻¹ for samples S7, S8, and S9, respectively. These peaks related to stretching vibration of O – H group in chitosan and (OH) in water existing in samples. The observed peaks in the range (3000 cm⁻¹ – 2800 cm⁻¹) is assigned to C – H and N – H stretching

vibration, the slightly shifted in band 2925 cm^{-1} , 2927 cm^{-1} , and 2928 cm^{-1} may be due to change of iron molarity which coordinates in nitrogen atom in amine group of chitosan.

Moreover, the located bands at 1635 cm^{-1} , 1636 cm^{-1} , and 1638 cm^{-1} assigned to N – H bending vibration in amine group of chitosan this band appeared as a shoulder in S7 and completely band with some increase in intensity for S8 and S9 as discussed above this change probably due to coordination of iron atom with chitosan in amine group. The bands appeared at 1577 cm^{-1} for S7, 1563 cm^{-1} for S8, and 1562 cm^{-1} for S9 is assigned to C – H bending vibration. In contrast, the band at 1412 cm^{-1} , 1414 cm^{-1} , and 1414 cm^{-1} for samples S7, S8, and S9, respectively are corresponding to C – C in the skeleton of chitosan.

Generally, FeNPs has opportunity to coordinate either with N atom in amine group or with an oxygen atom in C – O group. A change was seen in the C – O – C of chitosan in samples S7, S8, and S9 with relevant peak appeared at 1062 cm^{-1} , 1083 cm^{-1} , 1082 cm^{-1} , respectively. Moreover, an observed peak at around 600 cm^{-1} correspondings to iron-oxygen stretching vibrations of iron nanoparticles. **Table 4.3** outlines the absorbance bands and their assignments of samples (S7 – S9).

The stretching vibration of C – O, N – H, and Fe – O was theoretically found, and it could be 1109.17 cm^{-1} , 3063.25 cm^{-1} , and 824.33 cm^{-1} . The slight difference in theoretical and practical results could be interpreted as a consequence of presence iron nanoparticles coordinate with other functional groups in the sample.

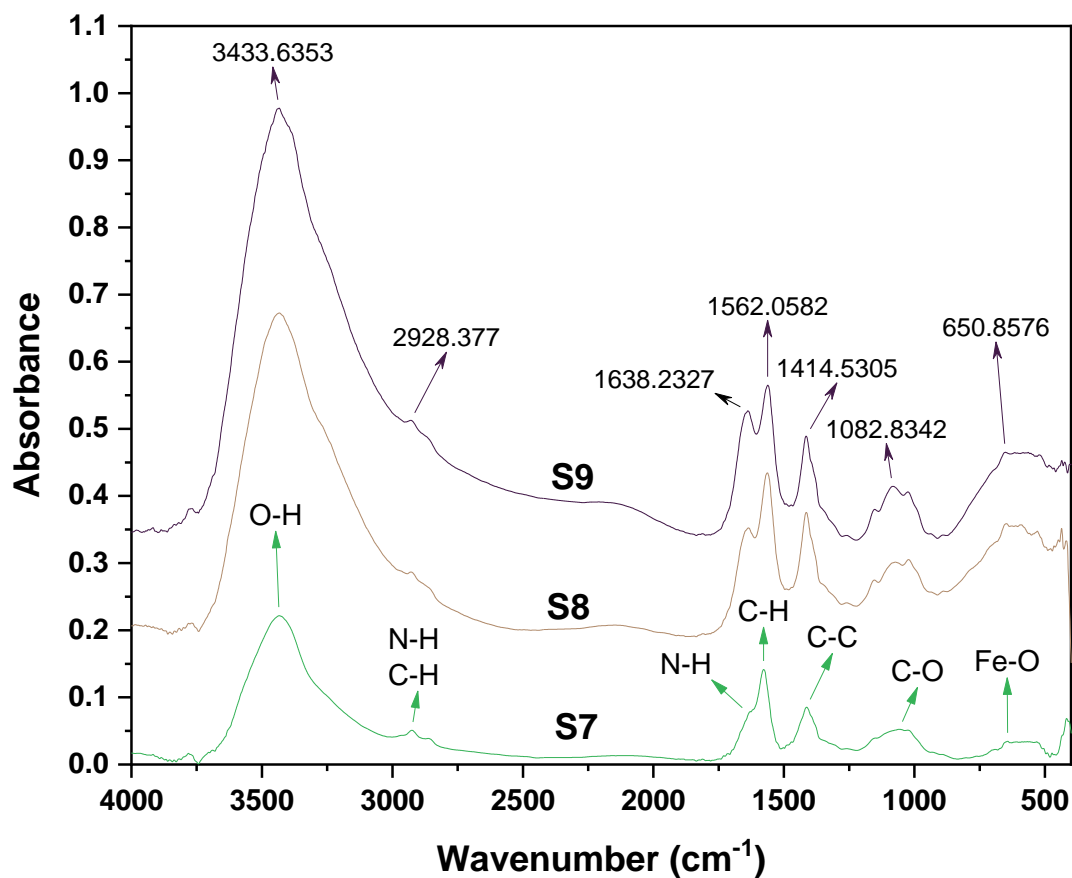


Figure 4.17: Fourier transforms infrared spectroscopy (FTIR) for iron nanoparticles synthesized by adding a different molar ratio of iron salt (Fe^{3+} : Fe^{2+}); S7 (3.6 mM), S8 (4.6 mM), and S9 (5.6 mM) to 200 ml of prepared chitosan.

Table 4.3: Positions of FTIR absorption peaks and their assignment functional groups for iron nanoparticle capped by chitosan samples (S7 – S9).

Wavenumber (cm ⁻¹)			Assignments
S7	S8	S9	
3433	3432	3433	O – H stretching vibration
2925	2927	2928	N – H and C – H stretching vibration
2861	2859	2861	
1635	1636	1638	N – H bending vibration
1577	1563	1562	C – H bending vibration
1412	1414	1414	C – C stretching vibration
1062	1083	1082	C – O stretching vibration
642	647	650	Fe – O stretching vibration

4.4.4 Fourier Transform Infrared Spectroscopy of Cobalt Nanoparticles Prepared at Different Concentrations of Sodium Hydroxide

Figure 4.18 represents FTIR spectra of cobalt nanoparticle prepared at a different molar ratio of sodium hydroxide, according to **Table 3.4** in the wavenumber range 4000 cm⁻¹ to 400 cm⁻¹.

Our samples were prepared at different concentrations of sodium hydroxide with a constant concentration of cobalt salt and hydrazine. It can be observed that the absorbance peaks appeared at approximately 3619 cm⁻¹ – 3300 cm⁻¹ is assigned

for O – H stretching vibration that existing in water and sodium hydroxide. In contrast, the weak band located at about 1628 cm^{-1} may be corresponding to O – H bending vibration. The strong absorption bands appeared at 1549 cm^{-1} , 1552 cm^{-1} , and 1554 cm^{-1} for samples S10, S11, and S12, respectively, is may be assigned to asymmetric vibration of Co_3O_4 .

Furthermore, the absorbance band that appeared at 1352 cm^{-1} , 1353 cm^{-1} , and 1353 cm^{-1} and at the next band appeared at 835 cm^{-1} , 834 cm^{-1} , and 832 cm^{-1} for sample S10, S11, and S12, respectively, is related to stretching and bending vibration Co – OH. According to the previous work done by Allaedini and Muhammad [127], these two bands approve to a phase purity of monodisperse one in the face-centered cubic structure of the cobalt nanoparticle samples.

The analysis results also had an absorbance peak at 512 cm^{-1} for S10, 528 cm^{-1} for S11, and 532 cm^{-1} for S12. These absorbance bands correspond to Co – O stretching vibration. **Table 4.4** summarizes the absorbance peaks and their assignments of all samples (S10 – S12).

The stretching vibration of Co – O was theoretically found and it could be 819.43 cm^{-1} . The slight difference in theoretical and experimental results could be interpreted as consequence of presence cobalt nanoparticles to be coordinated with other functional groups in the sample.

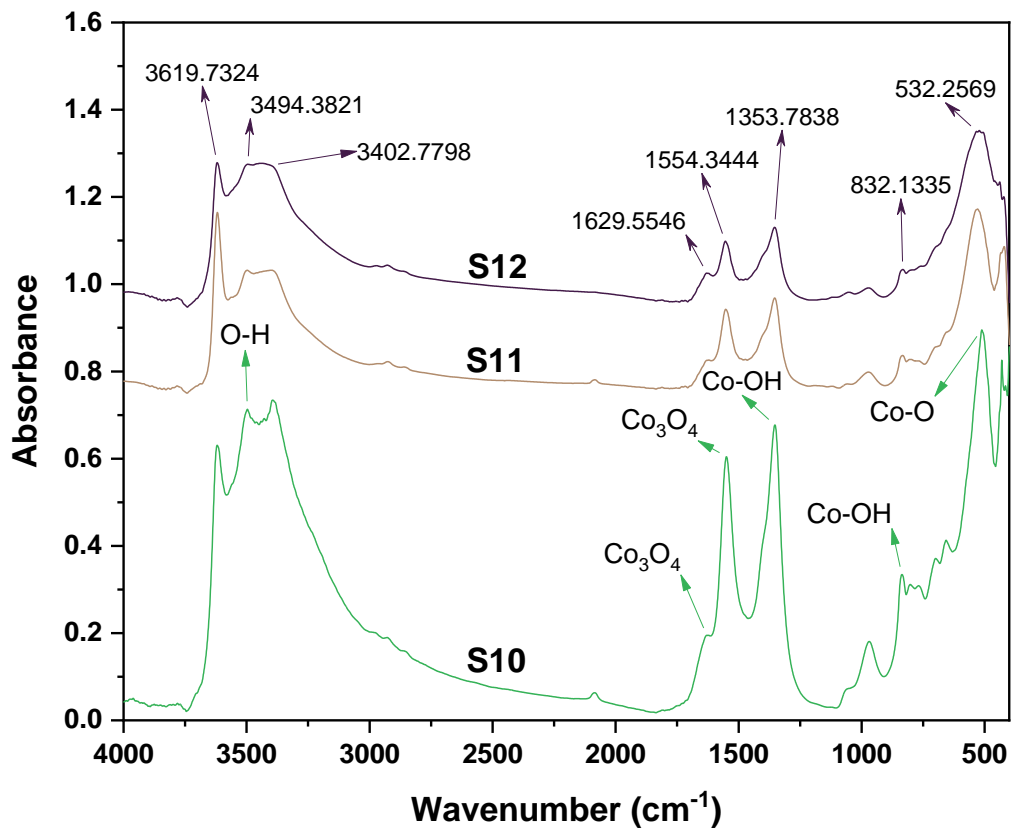


Figure 4.18: Fourier transform infrared spectroscopy (FTIR) of synthesized cobalt nanoparticle by adding 200 ml with concentration (0.25 M) of cobalt salt with a different molar ratio of NaOH; S10 (0.5 M), S11 (1.5 M), and S12 (2.5 M).

Table 4.4: Positions of FTIR absorption peaks and their assignment functional groups for cobalt nanoparticle prepared at different concentrations of sodium hydroxide samples (S10 – S12).

Wavenumber (cm ⁻¹)			Assignments
S10	S11	S12	
3619	3618	3619	O – H stretching vibration
3496	3497	3494	
3394	3400	3402	
1628	1626	1629	Co ₃ O ₄ bending and stretching vibration
1549	1552	1554	
1352	1353	1353	Co – OH stretching and bending vibration
835	834	832	
512	528	532	Co – O stretching vibration

4.5 Applications of Nanoparticles in Water Purification

4.5.1 UV-Visible Spectroscopy with Different Concentrations of Nickel Nitrate

Figure 4.19 shows the ultraviolet-visible spectra of nickel nitrate hexahydrate solution dissolved in distilled water at a different concentration which is ($1 \times 10^{-1} M$), ($2 \times 10^{-1} M$), ($3 \times 10^{-1} M$), and ($4 \times 10^{-1} M$). From this Figure, it is clear that the absorption bands were seen at 300 nm and 396 nm as well as two low-intensity bands at 656 nm and 720 nm, respectively. As mentioned earlier, the

electronic transition occurs when the molecular ions absorb radiation and causing absorption bands in a range of wavelengths [92]. The two sharp bands appeared at 300 nm, and 396 nm can be assigned to electronic transition of nickel ions that existing in nickel nitrate hexahydrate dissolved in water, which refers to uncomplexed nitrate, while the two low bands appeared at 656 nm and 720 nm may be assigned to d-d transitions [128]. It notes that the absorption of the whole band was increased by increasing the concentration of nickel nitrate hexahydrate. The relationship between increasing absorbance of two bands at 300 nm and 396 nm was demonstrated in **Figure 4.20**. Generally, the fluctuation in intensity follows Beer-Lambert law $A = \log_{10} \left(\frac{I_0}{I} \right) = \epsilon cl$, that illustrate increase absorbance with increasing concentration this law was explained in detail in section (2.2.2).

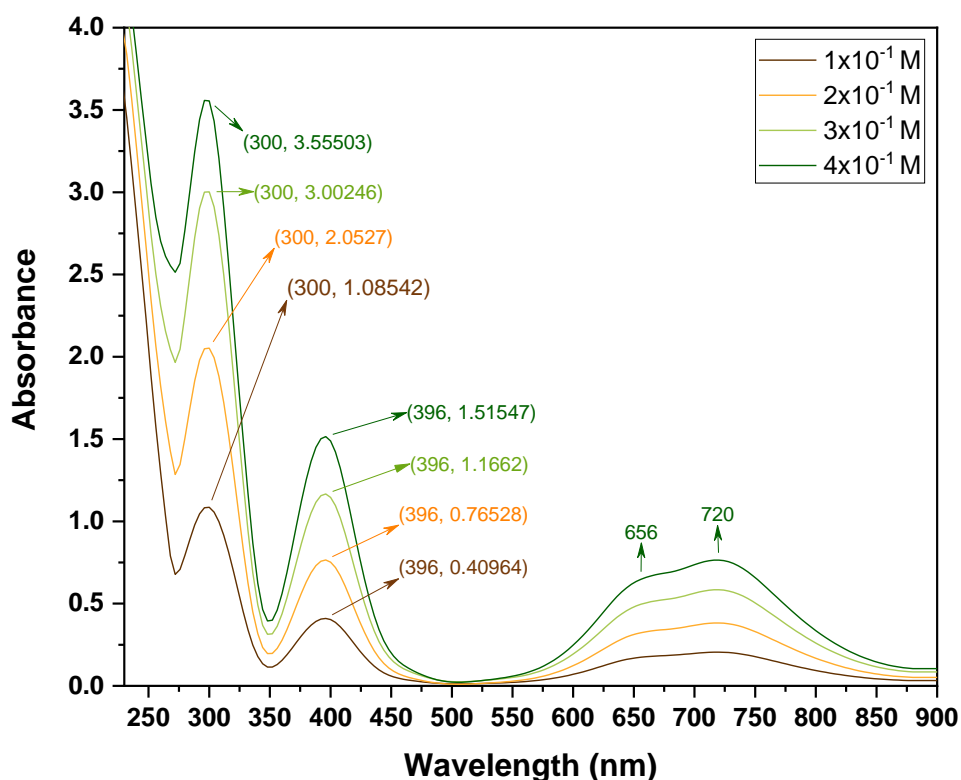


Figure 4.19: UV-Vis absorbance spectra of nickel salt solution with different concentrations.

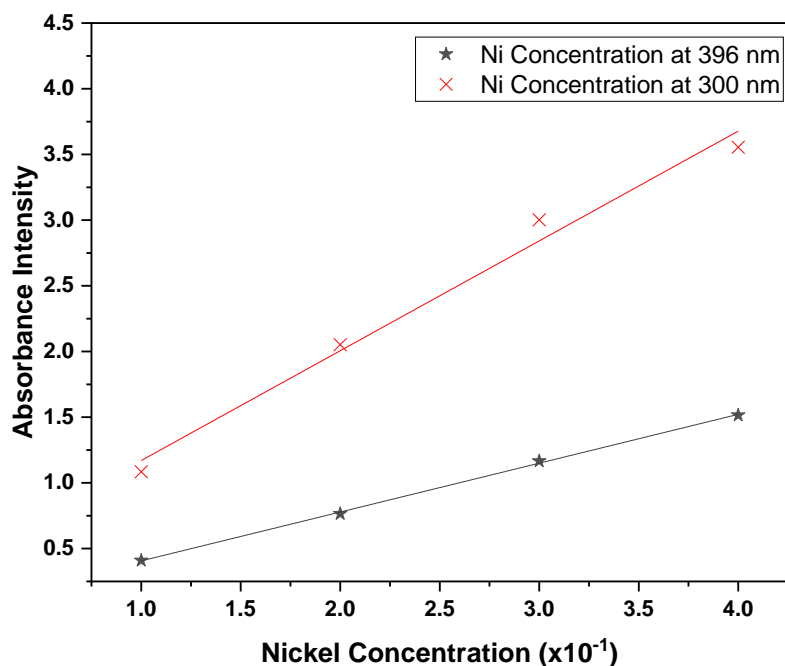


Figure 4.20: Relationship between the absorbance intensity of nickel electronic transition bands with concentrations at 300 nm and 396 nm.

4.5.2 Study the Alternating in Nickel Salt Concentrations Dissolved in Water After Passing through Imbibed Filter by Gold Nanoparticles

To study the effecting of AuNPs impregnated in filter on nickel nitrate hexahydrate concentrations dissolved in water as represented in **Figure 4.21**, such that 5 ml of AuNPs with size 28 nm was imbibed into WILKERSON filter element. After that, the impregnated filter was placed on oven at 40 °C to dry. Different concentrations of nickel nitrate with followed concentrations ($1 \times 10^{-1} M$, $2 \times 10^{-1} M$, $3 \times 10^{-1} M$, $4 \times 10^{-1} M$) was utilized in order to pass through the impregnated filter. Subsequently, the filtered solution was investigated via UV measurement, as shown in **Figure 4.22**. From this Figure, it noted that the absorbance increases with increasing nickel concentration. **Figure 4.23** and **Figure 4.24** displays the absorbance intensity of the Ni concentrations solution before and after passing through an imbibed filter at 300 nm and 396 nm, respectively. Plotted

Figures shows that, Ni concentration was decreased by using AuNPs as impregnation into filter, which means it could be used AuNPs as enhancing in water desalination.



Figure 4.21: Illustration image of filter element including nano samples (AuNPs, AgNPs, FeNPs, or CoNPs).

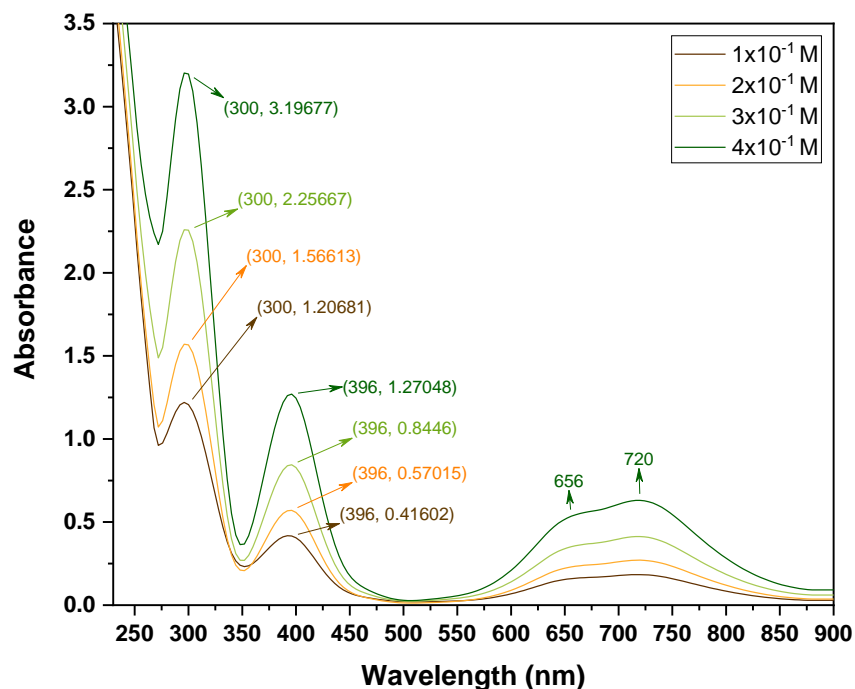


Figure 4.22: UV-Vis absorbance spectra of Ni solution with different concentrations after passing through filter impregnated by gold nanoparticle size 28 nm.

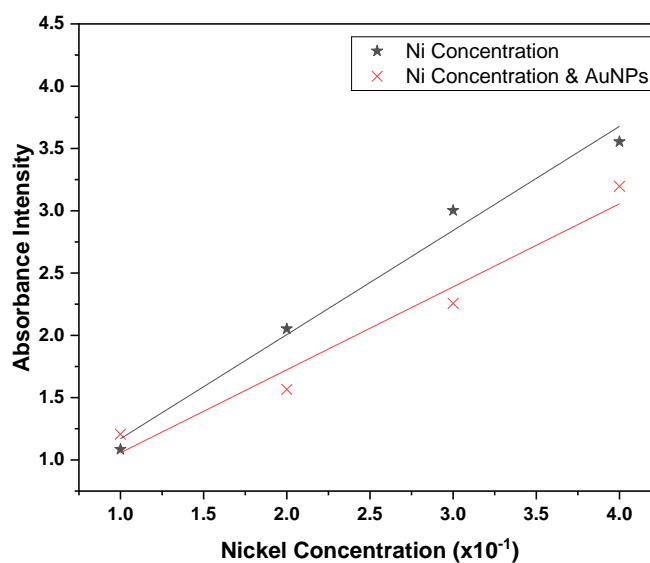


Figure 4.23: Relationship between the absorbance intensity values at 300 nm with change in nickel concentration before and after passing through an imbibed filter with AuNPs 28 nm.

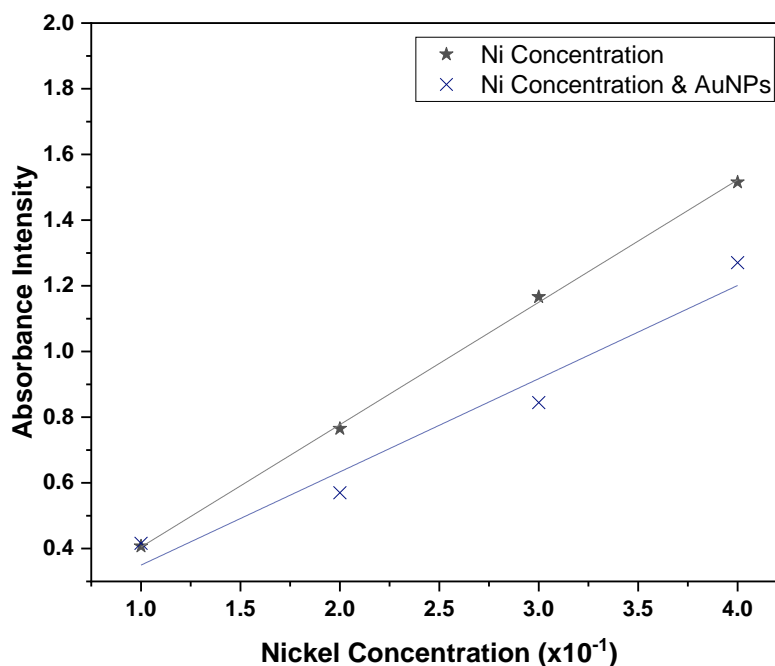


Figure 4.24: Relationship between the absorbance intensity values at 396 nm with change in nickel concentration before and after passing through an imbibed filter with AuNPs 28 nm.

4.5.3 Study the Alternating in Nickel Salt Concentrations Dissolved in Water After Passing through Imbibed Filter by Silver Nanoparticles

The effecting of AgNPs on nickel nitrate hexahydrate concentrations, which dissolved in water, was studied by imbibed 5 ml of AgNPs with average particle size 28 nm into filter element as depicted in **Figure 4.21**. Follow that, heating the filter at 40 °C in oven to dry. After that, the dissolved nickel nitrate solution with different concentrations was used to pass through the filter, and the filtered solution was measured by UV-Vis immediately the result was illustrated in **Figure 4.25**.

From the illustrated Figure, it can be seen that the filtered solution has four absorption bands observed at around 300 nm, 396 nm, 656 nm, and 720 nm with difference in intensity. The intensity was varying as a consequence of changing

nickel concentration in solution; the intensity of the first two bands was evident in **Figure 4.26** and **Figure 4.27**.

It is clear that the filter membrane, which impregnated by silver nanoparticles, is no active at low concentrations of nickel. Nevertheless, it is succeeded at high concentration; this may be due to electronegativity of silver element wherefore AgNPs membrane is preferred to utilize at high concentration of nickel element.

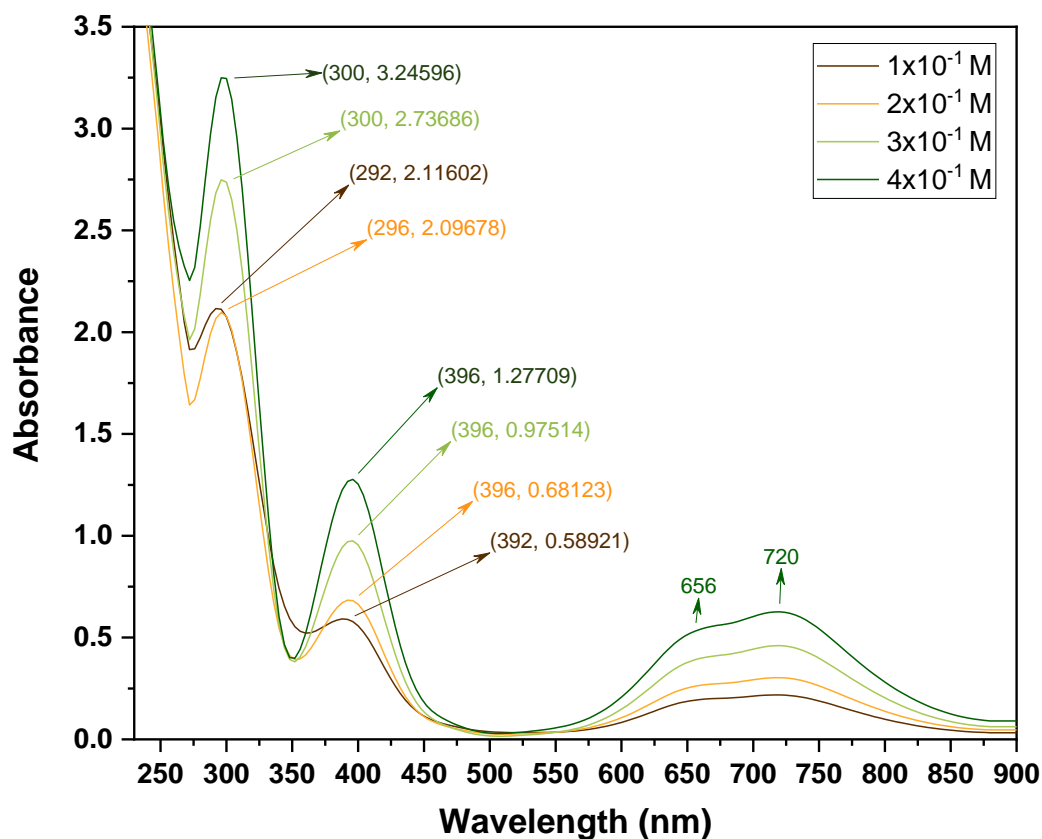


Figure 4.25: UV-Vis absorbance spectra of Ni solution with different concentrations after passing through filter impregnated by silver nanoparticle size 28 nm.

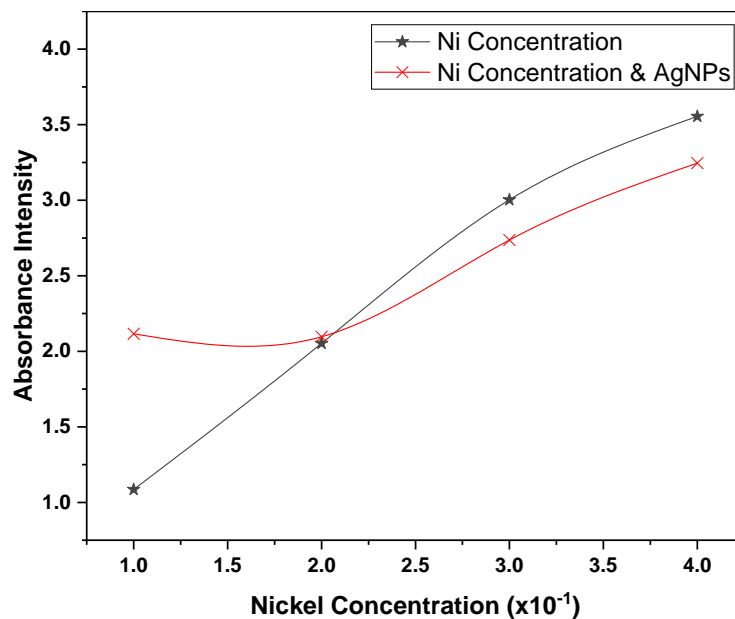


Figure 4.26: Relationship between the absorbance intensity values at 300 nm with change in nickel concentration before and after passing through an imbibed filter with AuNPs 28 nm.

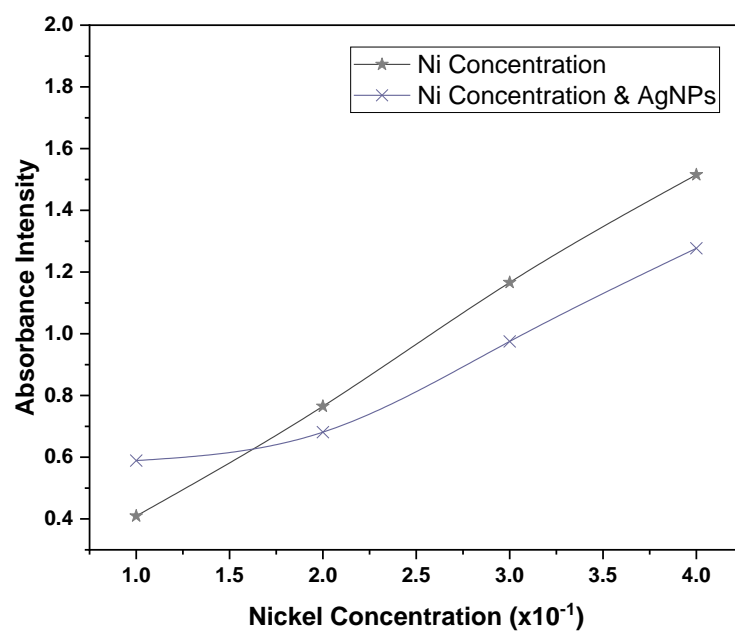


Figure 4.27: Relationship between the absorbance intensity values at 396 nm with change in nickel concentration before and after passing through an imbibed filter with AgNPs 28 nm.

4.5.4 Study the Alternating in Nickel Salt Concentrations Dissolved in Water After Passing through Imbibed Filter by Iron Nanoparticles

As discussed before, to study the effecting of FeNPs on nickel nitrate hexahydrate concentrations dissolved in water, it can be done by impregnate 5 ml of FeNPs with 18 nm average particle size into WILKERSON filter element, as shown in **Figure 4.21**. Then, the impregnated filter was placed on the oven at 40 °C to dry. Four different concentrations of nickel nitrate were utilized to pass through the impregnated filter. After that, the filtered solution was examined by ultraviolet-visible spectroscopy, as represented in **Figure 4.28**.

From depicted Figure, it is clear that the iron nanoparticle has a distinctive result of nickel filtration than that illustrated result in **Figure 4.19**. This result confirms that nanoparticle matter has influence result in groundwater enhancement. In addition, it was noticed that the absorbance intensity shows compatible results with concentrations of nickel solution, as when the concentration increase, the intensity will increase. **Figure 4.29** and **Figure 4.30** show the spectrum data at two different position bands of a filtered and unfiltered nickel solution, which precisely located at 300 nm and 396 nm.

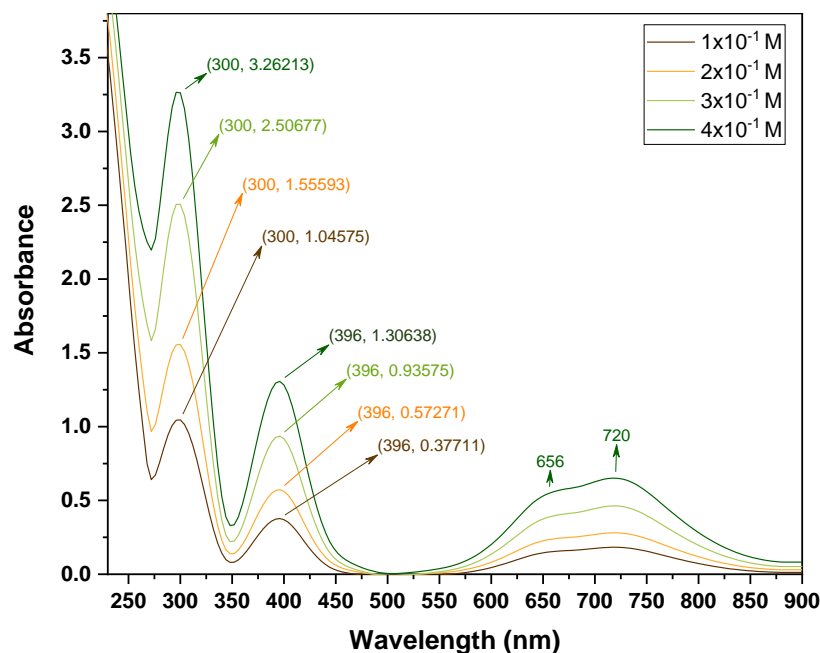


Figure 4.28: UV-Vis absorbance spectra of Ni solution with different concentrations after passing through filter impregnated by iron nanoparticle size 18 nm.

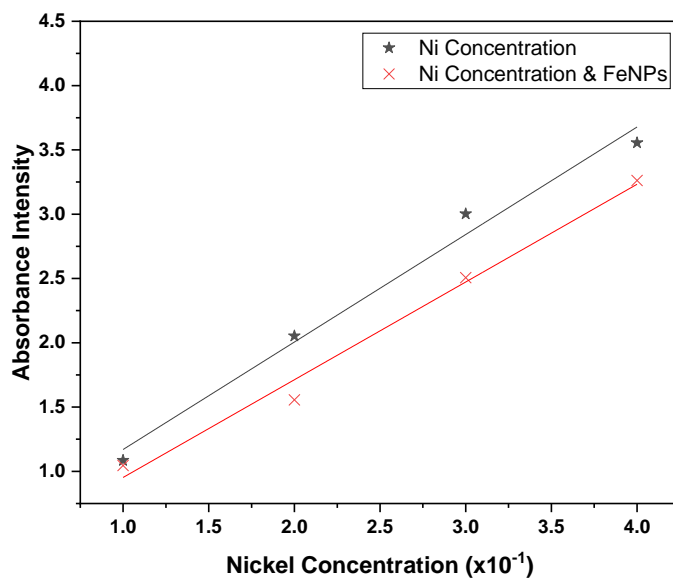


Figure 4.29: Relationship between the absorbance intensity values at 300 nm with change in nickel concentration before and after passing through an imbibed filter with FeNPs 18 nm.

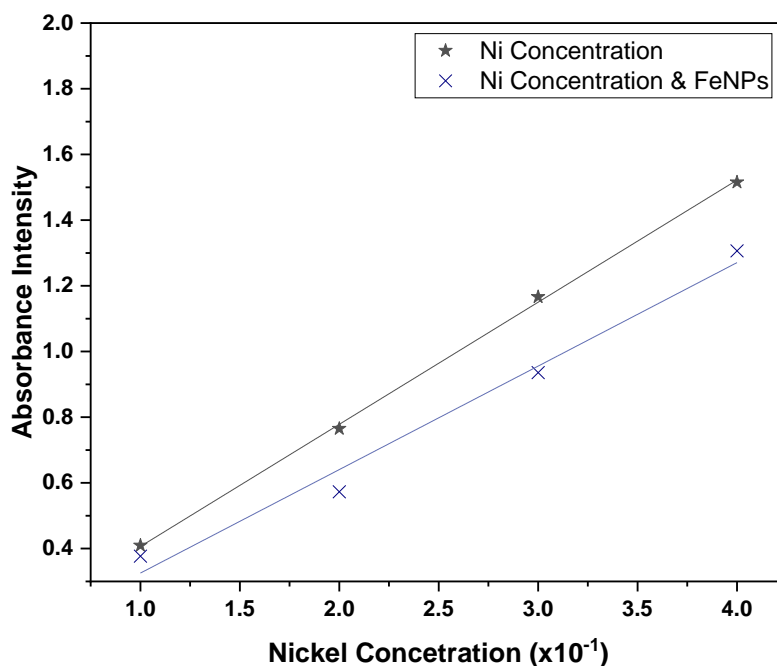


Figure 4.30: Relationship between the absorbance intensity values at 396 nm with change in nickel concentration before and after passing through an imbibed filter with FeNPs 18 nm.

4.5.5 Study the Alternating in Nickel Salt Concentrations Dissolved in Water After Passing through Imbibed Filter by Cobalt Nanoparticles

The effecting of CoNPs on concentrations of nickel nitrate hexahydrate dissolved in water was studied by impregnating 5 ml of CoNPs sample (S12) into filter elements as represented in **Figure 4.21**. Then, filter element was heated in oven calibrated at 40 °C in order to dry. Subsequently, the dissolved nickel nitrate solution with four different concentrations was used to pass through the filter follow that measuring solution via UV-Vis spectroscopy, as shown in **Figure 4.31**.

From the illustrated Figure, it noted that the absorbance increases with increasing nickel concentration as a general behavior that follows Beer-lambert's law. Moreover, the absorbance intensity could show more decreasing in

concentration as a consequence of applying filter element impregnated with CoNPs as plotted in **Figure 4.32** and **Figure 4.33** at near 300 nm and 396 nm, respectively. The increment of absorbance intensity of nickel concentration ($1 \times 10^{-1} M$) before and after using imbibed filter show exceptional result; it could be owing to the electronegativity of cobalt nanoparticle this mean CoNPs is failed at low concentration while it shows great result at high concentrations of nickel.

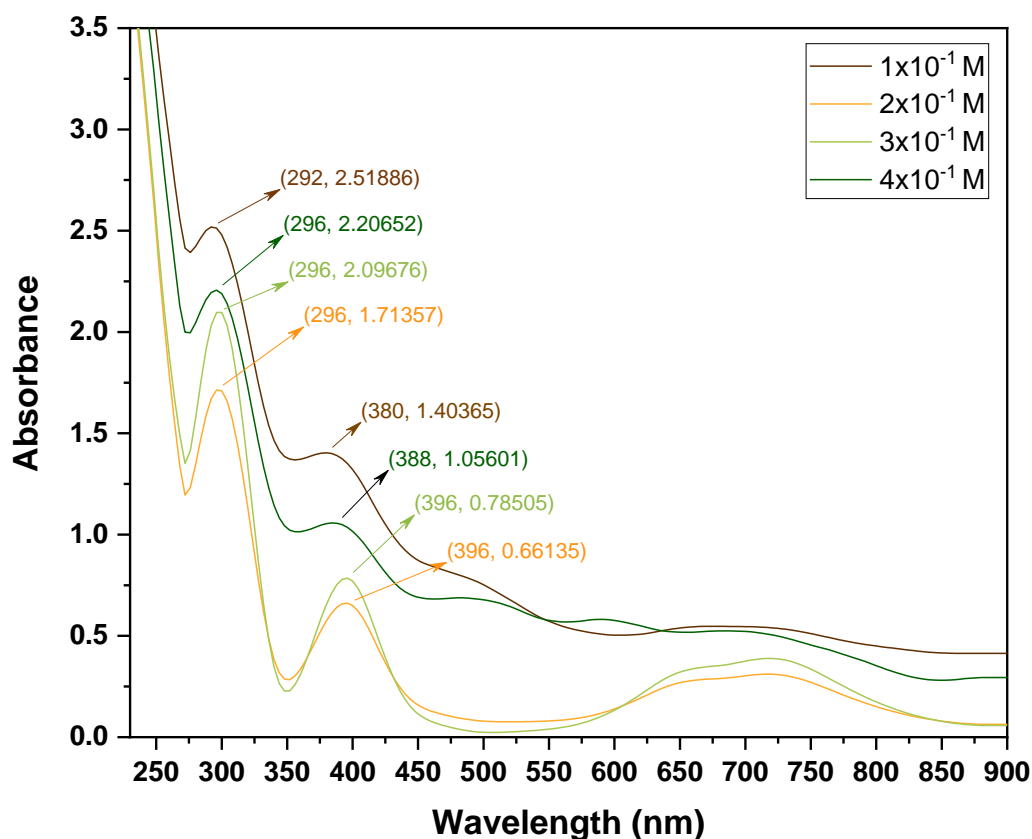


Figure 4.31: UV-Vis absorbance spectra of Ni solution with different concentrations after passing through filter impregnated by cobalt nanoparticle.

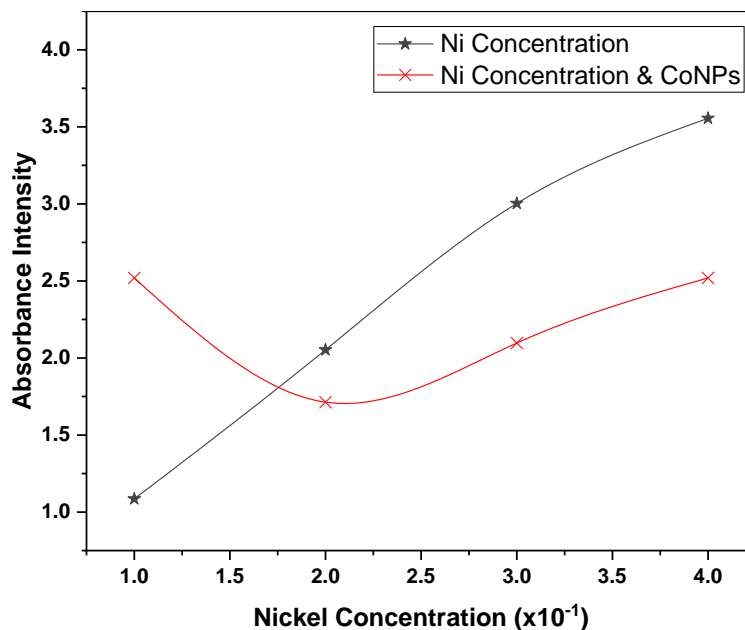


Figure 4.32: Relationship between the absorbance intensity values at near 300 nm with change in nickel concentration before and after passing through an imbided filter with CoNPs.

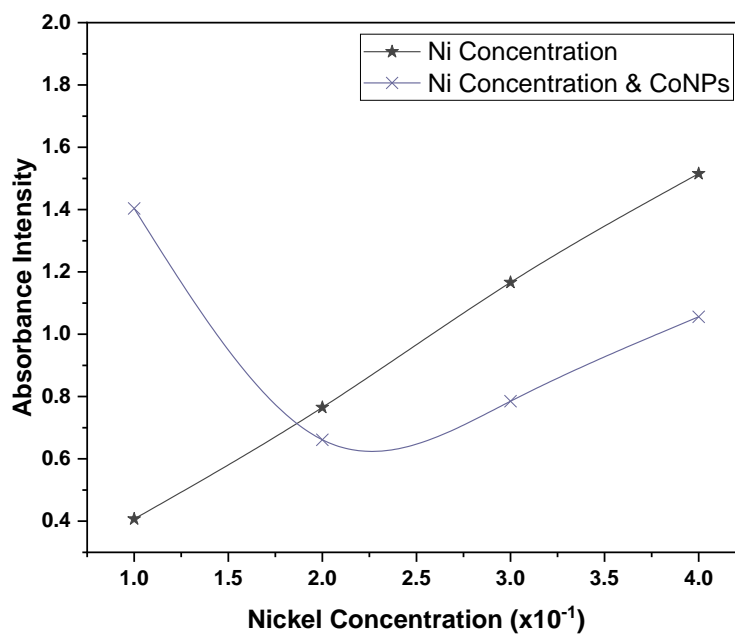


Figure 4.33: Relationship between the absorbance intensity values at near 396 nm with change in nickel concentration before and after passing through an imbided filter with CoNPs.

To sum up, there is a direct relationship between the absorbance intensity and concentration, as the concentration increases the absorbance intensity increase in solution according to Beer-Lambert law. Besides, the absorbance intensity of the nickel solution decrease after using nanoparticle as impregnated onto the membrane filter. The absorbance intensity of both bands, 300 nm and 396 nm of whole samples were summarized in **Figure 4.34** and **Figure 4.35**.

By comparing the absorbance values at low concentration $1 \times 10^{-1} M$ before and after filtration, it is known that the absorbance before filtering has high intensity. At the same time, it decreased after filtration process regardless of the exceptional result that appeared in AgNPs and CoNPs samples, which is owing to the electronegativity of elements. Moreover, all samples show excellent results at high concentrations of nickel solution as represented in Figure.

What shown above suggest that the prepared nanoparticles have a high influence effect in dilute nickel concentration existing in solution; this means it could be utilized in groundwater purification and desalination, which contributes as a cooperative in environment application. More than anything else, the Figure clarify that at high concentration of nickel solution which is $3 \times 10^{-1} M$ and $4 \times 10^{-1} M$, the CoNPs is more effectual than AuNPs, FeNPs, and AgNPs, respectively. Hence of that, the cobalt nanoparticles is preferred to use in groundwater purification.

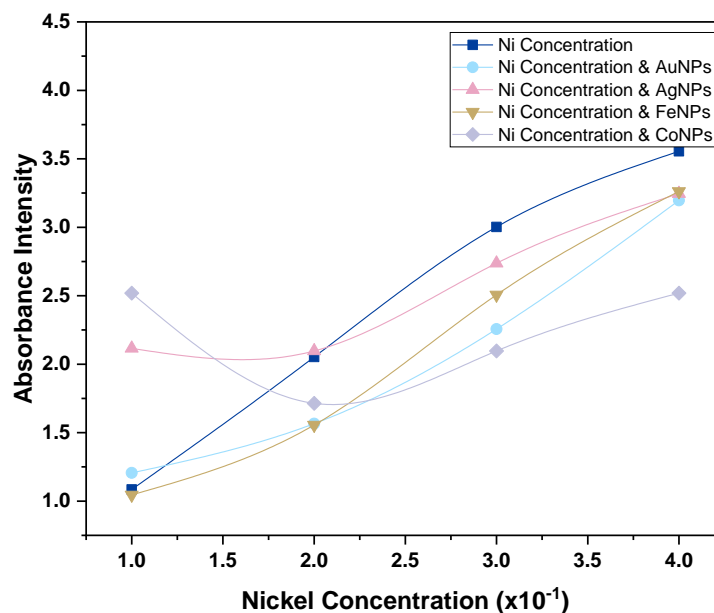


Figure 4.34: Relationship between the absorbance intensity of unfiltered and filtered Ni solution with some prepared nanoparticles samples at 300 nm electronic transition against concentrations.

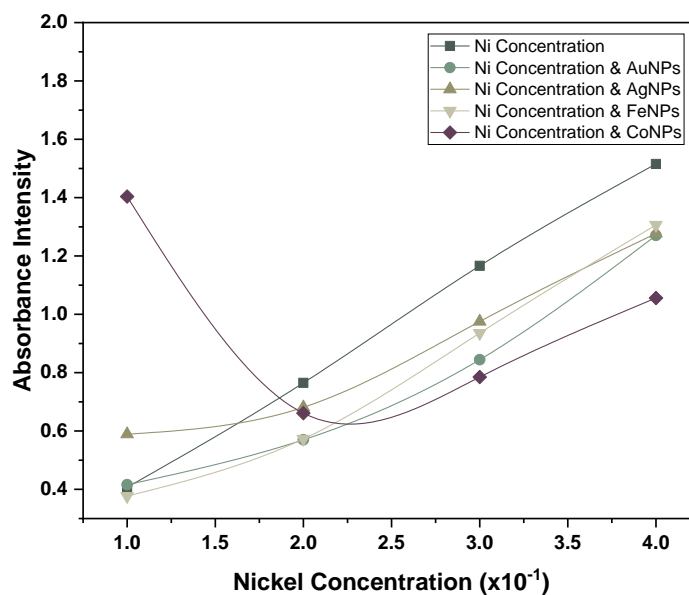


Figure 4.35: Relationship between the absorbance intensity of unfiltered and filtered Ni solution with some prepared nanoparticles samples at 396 nm electronic transition against concentrations.

Conclusion

Conclusions

This thesis has shown the preparation method of nanoparticles, such as AuNPs, AgNPs, FeNPs, and CoNPs. Each material was prepared at three different conditions. Besides, numerous methods to synthesize nanoparticles were reported in literature, tacking the additional consideration in study. This part of the thesis has clearly shown that any varying in preparation conditions could give a difference in particle size.

The effect of different preparation conditions was studied using ultraviolet spectroscopy, and their surface plasmonic resonance was measured. This result found that, with increasing lemon extract in gold nanoparticles, the surface plasmonic bands shifted to lower wavelength, which indicates of creating smaller particle size.

The morphology and distribution of prepared nanoparticles were discussed by using a high-resolution transmission electron microscope, and the average of spherical particle size was estimated. Therefore, it possible to conclude that the shape of the particles on visualization images could affect on the average particle size of nano. Moreover, the average particle size of Gaussian distribution for iron nanoparticles after drying is larger than before drying.

By using X-ray diffraction pattern, the crystallinity was studied, and the average crystalline size was calculated through Scherrer's equation. This study has shown that there is a direct relationship between increasing sodium hydroxide concentration and peak intensity in cobalt nanoparticles.

Fourier transform infrared investigate the chemical interaction of prepared nanoparticles and its surfactant materials. Also, the assignments' functional groups

were specified, as well as the wavenumber of theoretical and practical results was compared. The result has been demonstrated that every sample had different peaks relating to their functional groups existing in capping of materials except the hydroxyl group; it exists in the whole samples, which refer to presented water in samples. In addition, there is a difference in theoretical and practical wavenumber results, and the reason for this alteration is the nanoparticles could be coordinated with other functional groups in samples.

The effect of prepared nanoparticle samples in decreasing nickel concentration in water was studied by applying them into WILKERSON filter element. It noted that there is a relationship between absorbance intensity and nickel concentration. Besides, the absorbance intensity of nickel solution decrease after using nanoparticles as impregnated onto membrane filter. Furthermore, at a low concentration of nickel elements, the nanoparticles are not active as much as at high concentrations. Therefore, the findings suggest that the prepared nanoparticles are applicable to purify water from heavy metals.

References

References

- [1] B. Bhushan, *Springer handbook of nanotechnology*. Springer, 2017.
- [2] J. Hulla, S. Sahu, and A. Hayes, "Nanotechnology: History and future," *Human & experimental toxicology*, vol. 34, no. 12, pp. 1318-1321, 2015.
- [3] M. Boholm, "The use and meaning of nano in American English: Towards a systematic description," *Ampersand*, vol. 3, pp. 163-173, 2016.
- [4] J. R. Lead and E. Valsami-Jones, *Nanoscience and the Environment*. Elsevier, 2014.
- [5] D. Kennedy, "Tiny Nanoparticles-A Big Battlefield Impact?," DEFENSE ACQUISITION UNIV FT BELVOIR VA2014.
- [6] A. Sengupta and C. K. Sarkar, *Introduction to nano: basics to nanoscience and nanotechnology*. Springer, 2015.
- [7] K. Winkelmann and B. Bhushan, *Global perspectives of nanoscience and engineering education*. Springer, 2016.
- [8] W. S. Khan and R. Asmatulu, *Nanotechnology Safety: Chapter 1. Nanotechnology Emerging Trends, Markets, and Concerns*. Elsevier Inc. Chapters, 2013.
- [9] C. Zhang, B. Xie, Y. Zou, D. Zhu, L. Lei, D. Zhao, and H. Nie, "Zero-dimensional, one-dimensional, two-dimensional and three-dimensional biomaterials for cell fate regulation," *Advanced drug delivery reviews*, vol. 132, pp. 33-56, 2018.
- [10] D.-K. Kim, Y. J. Hwang, C. Yoon, H.-O. Yoon, K. S. Chang, G. Lee, S. Lee, and G.-R. Yi, "Experimental approach to the fundamental limit of the extinction coefficients of ultra-smooth and highly spherical gold

- nanoparticles," *Physical Chemistry Chemical Physics*, vol. 17, no. 32, pp. 20786-20794, 2015.
- [11] Z. Abdullaeva, *Nano-and Biomaterials: Compounds, Properties, Characterization, and Applications*. John Wiley & Sons, 2017.
- [12] J. Yao, C. W. Bastiaansen, and T. Peijs, "High strength and high modulus electrospun nanofibers," *Fibers*, vol. 2, no. 2, pp. 158-186, 2014.
- [13] S. Simões, F. Viana, and M. F. Vieira, "Reactive commercial Ni/Al nanolayers for joining lightweight alloys," *Journal of materials engineering and performance*, vol. 23, no. 5, pp. 1536-1543, 2014.
- [14] J. L. Liu and S. Bashir, *Advanced nanomaterials and their applications in renewable energy*. Elsevier, 2015.
- [15] C. R. Morfa, M. M. de Farias, I. P. P. Morales, E. O. I. de Navarra, and R. R. Valera, "Virtual modeling of polycrystalline structures of materials using particle packing algorithms and Laguerre cells," *Computational Particle Mechanics*, vol. 5, no. 2, pp. 213-226, 2018.
- [16] P. Navya and H. K. Daima, "Rational engineering of physicochemical properties of nanomaterials for biomedical applications with nanotoxicological perspectives," *Nano Convergence*, vol. 3, no. 1, p. 1, 2016.
- [17] K. E. Jasim, "Quantum dots solar cells," *Solar Cells-New Approaches and Reviews*, 2015.
- [18] E. Samimi, P. Karami, and M. Ahar, "A Review on Aptamer-Conjugated Quantum Dot Nanosystems for Cancer Imaging and Theranostic," *J Nanomed Res*, vol. 5, no. 3, p. 00117, 2017.
- [19] G. Grosso and G. P. Parravicini, "Chapter 12 - Optical Properties of Semiconductors and Insulators," in *Solid State Physics (Second Edition)*, G.

- Grosso and G. P. Parravicini, Eds. Amsterdam: Academic Press, 2014, pp. 529-576.
- [20] S. Ghorai, "Chemical, physical and mechanical properties of nanomaterials and its applications," 2013.
- [21] D. Guo, G. Xie, and J. Luo, "Mechanical properties of nanoparticles: basics and applications," *Journal of physics D: applied physics*, vol. 47, no. 1, p. 013001, 2013.
- [22] "Chapter 4 - Fundamentals of Materials Science," in *Craig's Restorative Dental Materials (Thirteenth Edition)*, R. L. Sakaguchi and J. M. Powers, Eds. Saint Louis: Mosby, 2012, pp. 33-81.
- [23] J. A. von Fraunhofer, "Adhesion and cohesion," *International journal of dentistry*, vol. 2012, 2012.
- [24] H. Zeng, *Polymer adhesion, friction, and lubrication*. John Wiley & Sons, 2013.
- [25] V. K. Khanna, "Integrated Nanoelectronics," *Integrated Nanoelectronics: Nanoscale CMOS, Post-CMOS and Allied Nanotechnologies, NanoScience and Technology*, ISBN 978-81-322-3623-8. Springer India, 2016, 2016.
- [26] C. Buzea and I. Pacheco, "Nanomaterials and their Classification," in *EMR/ESR/EPR Spectroscopy for Characterization of Nanomaterials*: Springer, 2017, pp. 3-45.
- [27] A. Akbarzadeh, M. Samiei, and S. Davaran, "Magnetic nanoparticles: preparation, physical properties, and applications in biomedicine," *Nanoscale research letters*, vol. 7, no. 1, p. 144, 2012.
- [28] T. D. Clemons, R. H. Kerr, and A. Joos, "Multifunctional magnetic nanoparticles: Design, synthesis, and biomedical applications," in

- Comprehensive nanoscience and nanotechnology: Volume 3: Biological nanoscience*: Elsevier BV, 2019, pp. 193-210.
- [29] V. Marghussian, "4 - Magnetic Properties of Nano-Glass Ceramics," in *Nano-Glass Ceramics*, V. Marghussian, Ed. Oxford: William Andrew Publishing, 2015, pp. 181-223.
- [30] C. Jiang, "Synthesis, assembly, and integration of magnetic nanoparticles for nanoparticle-based spintronic devices," *HKU Theses Online (HKUTO)*, 2017.
- [31] T. Edvinsson, "Optical quantum confinement and photocatalytic properties in two-, one- and zero-dimensional nanostructures," *Royal Society open science*, vol. 5, no. 9, p. 180387, 2018.
- [32] B. P. Isaacoff and K. A. Brown, "Progress in top-down control of bottom-up assembly," ed: ACS Publications, 2017.
- [33] G. Pandey, D. Rawtani, and Y. K. Agrawal, "Aspects of nanoelectronics in materials development," in *Nanoelectronics and Materials Development*: IntechOpen, 2016.
- [34] V. Arole and S. Munde, "Fabrication of nanomaterials by top-down and bottom-up approaches-an overview," *Journal of Materials Science*, vol. 1, pp. 89-93, 2014.
- [35] D. Sumanth Kumar, B. Jai Kumar, and H. M. Mahesh, "Chapter 3 - Quantum Nanostructures (QDs): An Overview," in *Synthesis of Inorganic Nanomaterials*, S. Mohan Bhagyaraj, O. S. Oluwafemi, N. Kalarikkal, and S. Thomas, Eds.: Woodhead Publishing, 2018, pp. 59-88.
- [36] D. Andrews, T. Nann, and R. H. Lipson, *Comprehensive Nanoscience and Nanotechnology*. Academic Press, 2019.
- [37] P. Khadka, J. Ro, H. Kim, I. Kim, J. T. Kim, H. Kim, J. M. Cho, G. Yun, and J. Lee, "Pharmaceutical particle technologies: An approach to improve drug

- solubility, dissolution and bioavailability," *Asian journal of pharmaceutical sciences*, vol. 9, no. 6, pp. 304-316, 2014.
- [38] B. Mu and A. Wang, "Fabrication and Applications of Carbon/Clay Mineral Nanocomposites," in *Nanomaterials from Clay Minerals*: Elsevier, 2019, pp. 537-587.
- [39] Q. Zhang, D. Sando, and V. Nagarajan, "Chemical route derived bismuth ferrite thin films and nanomaterials," *Journal of Materials Chemistry C*, vol. 4, no. 19, pp. 4092-4124, 2016.
- [40] H. Aminirastabi, G. Ji, H. Xue, and D. Peng, "Sol-Gel Process and Engineering Nanostructure," in *Sol-Gel Method-Design and Synthesis of New Materials with Interesting Physical, Chemical and Biological Properties*: IntechOpen, 2018.
- [41] X. Wang, M. Ahmad, and H. Sun, "Three-dimensional ZnO hierarchical nanostructures: Solution phase synthesis and applications," *Materials*, vol. 10, no. 11, p. 1304, 2017.
- [42] A. R. Sadrolhosseini, M. A. Mahdi, F. Alizadeh, and S. A. Rashid, "Laser Ablation Technique for Synthesis of Metal Nanoparticle in Liquid," in *Laser Technology and its Applications*: IntechOpen, 2018.
- [43] J. Mitra, G. J. Abraham, M. Kesaria, S. Bahl, A. Gupta, S. M. Shivaprasad, C. S. Viswanadham, U. D. Kulkarni, and G. K. Dey, "Role of substrate temperature in the pulsed laser deposition of zirconium oxide thin film," in *Materials Science Forum*, 2012, vol. 710, pp. 757-761: Trans Tech Publ.
- [44] E. Omanović-Miklićanin and M. Maksimović, "Nanosensors applications in agriculture and food industry," *Bull Chem Technol Bosnia Herzegovina*, vol. 47, pp. 59-70, 2016.

- [45] N. Dasgupta, S. Ranjan, and C. Ramalingam, "Applications of nanotechnology in agriculture and water quality management," *Environmental Chemistry Letters*, vol. 15, no. 4, pp. 591-605, 2017.
- [46] R. Prasad, A. Bhattacharyya, and Q. D. Nguyen, "Nanotechnology in sustainable agriculture: recent developments, challenges, and perspectives," *Frontiers in microbiology*, vol. 8, p. 1014, 2017.
- [47] J. Gardner, "Nanotechnology in medicine and healthcare: possibilities, progress and problems: education and training," *South African Journal of Bioethics and Law*, vol. 8, no. 2, pp. 50-53, 2015.
- [48] S. Sarkar and S. C. Sarkar, "Chapter-4 Application of Nanotechnology in Medicine," *MED CAL SCIENCES*, vol. 117, p. 49, 2019.
- [49] S. A. Rizvi and A. M. Saleh, "Applications of nanoparticle systems in drug delivery technology," *Saudi Pharmaceutical Journal*, vol. 26, no. 1, pp. 64-70, 2018.
- [50] D. Das, "Nanotechnology: a revolution in targeted drug delivery," *International Journal of Basic & Clinical Pharmacology*, vol. 6, no. 12, p. 2766, 2017.
- [51] Y. Ge, S. Li, S. Wang, and R. Moore, *Nanomedicine: Principles and perspectives*. Springer, 2014.
- [52] D. Ghernaout, A. Alghamdi, M. Touahmia, M. Aichouni, and N. A. Messaoudene, "Nanotechnology phenomena in the light of the solar energy," *J Energ Environ Chem Eng*, vol. 3, pp. 1-8, 2018.
- [53] A. K. Hussein, "Applications of nanotechnology in renewable energies—A comprehensive overview and understanding," *Renewable and Sustainable Energy Reviews*, vol. 42, pp. 460-476, 2015.

- [54] S. Sharma, K. K. Jain, and A. Sharma, "Solar cells: in research and applications—a review," *Materials Sciences and Applications*, vol. 6, no. 12, p. 1145, 2015.
- [55] S. Baruah, M. N. Khan, and J. Dutta, "Perspectives and applications of nanotechnology in water treatment," *Environmental chemistry letters*, vol. 14, no. 1, pp. 1-14, 2016.
- [56] L. Madhura, S. Singh, S. Kanchi, M. Sabela, and K. Bisetty, "Nanotechnology-based water quality management for wastewater treatment," *Environmental Chemistry Letters*, vol. 17, no. 1, pp. 65-121, 2019.
- [57] G. Ghasemzadeh, M. Momenpour, F. Omid, M. R. Hosseini, M. Ahani, and A. Barzegari, "Applications of nanomaterials in water treatment and environmental remediation," *Frontiers of Environmental Science & Engineering*, vol. 8, no. 4, pp. 471-482, 2014.
- [58] A. Hu and A. Apblett, *Nanotechnology for water treatment and purification*. Springer, 2014.
- [59] H. Delprat, C. Hoang-Van, and P. Pichat, "Heterogeneous photocatalysis: use in water treatment and involvement in atmospheric chemistry," *Aquatic and Surface Photochemistry*, p. 369, 2018.
- [60] Y. J. Lee, E.-Y. Ahn, and Y. Park, "Shape-dependent cytotoxicity and cellular uptake of gold nanoparticles synthesized using green tea extract," *Nanoscale research letters*, vol. 14, no. 1, p. 129, 2019.
- [61] Z. Parang and D. Moghadamnia, "Synthesis of silver-cobalt nanoparticles by chemical reduction method and its effects on serum levels of thyroid hormones in adult male rats," *Nanomedicine Research Journal*, vol. 3, no. 4, pp. 236-244, 2019.

- [62] A. Bhattacharjee, T. Ghosh, and A. Datta, "Green synthesis and characterisation of antioxidant-tagged gold nanoparticle (X-GNP) and studies on its potent antimicrobial activity," *Journal of Experimental Nanoscience*, vol. 13, no. 1, pp. 50-61, 2018.
- [63] Y. Choi, S. Kang, S.-H. Cha, H.-S. Kim, K. Song, Y. J. Lee, K. Kim, Y. S. Kim, S. Cho, and Y. Park, "Platycodon saponins from *Platycodi Radix* (*Platycodon grandiflorum*) for the green synthesis of gold and silver nanoparticles," *Nanoscale research letters*, vol. 13, no. 1, p. 23, 2018.
- [64] F. K. Alsammarrarie, W. Wang, P. Zhou, A. Mustapha, and M. Lin, "Green synthesis of silver nanoparticles using turmeric extracts and investigation of their antibacterial activities," *Colloids and Surfaces B: Biointerfaces*, vol. 171, pp. 398-405, 2018.
- [65] J. U. Chandirika and G. Annadurai, "Biosynthesis and Characterization of Silver Nanoparticles Using Leaf Extract *Abutilon indicum*," *Global Journal of Biotechnology & Biochemistry*, vol. 13, no. 1, pp. 07-11, 2018.
- [66] P. Kaur, R. Thakur, H. Malwal, A. Manuja, and A. Chaudhury, "Biosynthesis of biocompatible and recyclable silver/iron and gold/iron core-shell nanoparticles for water purification technology," *Biocatalysis and Agricultural Biotechnology*, vol. 14, pp. 189-197, 2018.
- [67] H. M. Muhy and F. Duman, "Biosynthesis, Characterization and Removal Efficiency for Petroleum Leakage of the CoFe_2O_4 Nanoparticles," *Al-Mustansiriyah Journal of Science*, vol. 29, no. 3 ICSSSA 2018 Conference Issue, pp. 21-28, 2018.
- [68] A. Kangama, D. Zeng, X. Tian, and J. Fang, "Application of Chitosan Composite Flocculant in Tap Water Treatment," *Journal of Chemistry*, vol. 2018, 2018.

- [69] A. Díaz-Hernández, J. Gracida, B. E. García-Almendárez, C. Regalado, R. Núñez, and A. Amaro-Reyes, "Characterization of magnetic nanoparticles coated with chitosan: A potential approach for enzyme immobilization," *Journal of Nanomaterials*, vol. 2018, 2018.
- [70] B. Kumar, K. Smita, L. Cumbal, and A. Debut, "Green synthesis of silver nanoparticles using Andean blackberry fruit extract," *Saudi journal of biological sciences*, vol. 24, no. 1, pp. 45-50, 2017.
- [71] N. Jayaprakash, J. J. Vijaya, K. Kaviyarasu, K. Kombaiah, L. J. Kennedy, R. J. Ramalingam, M. A. Munusamy, and H. A. Al-Lohedan, "Green synthesis of Ag nanoparticles using Tamarind fruit extract for the antibacterial studies," *Journal of Photochemistry and Photobiology B: Biology*, vol. 169, pp. 178-185, 2017.
- [72] S. Raja, V. Ramesh, and V. Thivaharan, "Green biosynthesis of silver nanoparticles using *Calliandra haematocephala* leaf extract, their antibacterial activity and hydrogen peroxide sensing capability," *Arabian journal of chemistry*, vol. 10, no. 2, pp. 253-261, 2017.
- [73] M. Alymov, N. Rubtsov, B. Seplyarskii, V. Zelenskii, and A. Ankudinov, "Preparation and characterization of iron nanoparticles protected by an oxide film," *Inorganic Materials*, vol. 53, no. 9, pp. 911-915, 2017.
- [74] S. Ansari, R. Bhor, K. Pai, D. Sen, S. Mazumder, K. Ghosh, Y. Kolekar, and C. Ramana, "Cobalt nanoparticles for biomedical applications: facile synthesis, physiochemical characterization, cytotoxicity behavior and biocompatibility," *Applied Surface Science*, vol. 414, pp. 171-187, 2017.
- [75] C. Devatha, A. K. Thalla, and S. Y. Katte, "Green synthesis of iron nanoparticles using different leaf extracts for treatment of domestic waste water," *Journal of cleaner production*, vol. 139, pp. 1425-1435, 2016.

- [76] K. Lee, P. Nagajyothi, T. Sreekanth, and S. Park, "Eco-friendly synthesis of gold nanoparticles (AuNPs) using *Inonotus obliquus* and their antibacterial, antioxidant and cytotoxic activities," *Journal of Industrial and Engineering Chemistry*, vol. 26, pp. 67-72, 2015.
- [77] J. K. Patra and K.-H. Baek, "Novel green synthesis of gold nanoparticles using *Citrullus lanatus* rind and investigation of proteasome inhibitory activity, antibacterial, and antioxidant potential," *International journal of nanomedicine*, vol. 10, p. 7253, 2015.
- [78] H. M. Ibrahim, "Green synthesis and characterization of silver nanoparticles using banana peel extract and their antimicrobial activity against representative microorganisms," *Journal of Radiation Research and Applied Sciences*, vol. 8, no. 3, pp. 265-275, 2015.
- [79] M. Abdollahi, S. Zeinali, S. Nasirimoghaddam, and S. Sabbaghi, "Effective removal of As (III) from drinking water samples by chitosan-coated magnetic nanoparticles," *Desalination and Water Treatment*, vol. 56, no. 8, pp. 2092-2104, 2015.
- [80] S. Salman, T. Usami, K. Kuroda, and M. Okido, "Synthesis and characterization of cobalt nanoparticles using hydrazine and citric acid," *Journal of Nanotechnology*, vol. 2014, 2014.
- [81] A. S. Zola, R. U. Ribeiro, J. M. C. Bueno, D. Zanchet, and P. A. Arroyo, "Cobalt nanoparticles prepared by three different methods," *Journal of Experimental Nanoscience*, vol. 9, no. 4, pp. 398-405, 2014.
- [82] L. Li, C. Luo, X. Li, H. Duan, and X. Wang, "Preparation of magnetic ionic liquid/chitosan/graphene oxide composite and application for water treatment," *International journal of biological macromolecules*, vol. 66, pp. 172-178, 2014.

- [83] M. V. Sujitha and S. Kannan, "Green synthesis of gold nanoparticles using Citrus fruits (Citrus limon, Citrus reticulata and Citrus sinensis) aqueous extract and its characterization," *Spectrochimica Acta Part A: Molecular and Biomolecular Spectroscopy*, vol. 102, pp. 15-23, 2013.
- [84] C. Jayaseelan, R. Ramkumar, A. A. Rahuman, and P. Perumal, "Green synthesis of gold nanoparticles using seed aqueous extract of *Abelmoschus esculentus* and its antifungal activity," *Industrial Crops and Products*, vol. 45, pp. 423-429, 2013.
- [85] P. Logeswari, S. Silambarasan, and J. Abraham, "Ecofriendly synthesis of silver nanoparticles from commercially available plant powders and their antibacterial properties," *Scientia Iranica*, vol. 20, no. 3, pp. 1049-1054, 2013.
- [86] T. Prathna, N. Chandrasekaran, A. M. Raichur, and A. Mukherjee, "Biomimetic synthesis of silver nanoparticles by Citrus limon (lemon) aqueous extract and theoretical prediction of particle size," *Colloids and Surfaces B: Biointerfaces*, vol. 82, no. 1, pp. 152-159, 2011.
- [87] A. Bankar, B. Joshi, A. R. Kumar, and S. Zinjarde, "Banana peel extract mediated synthesis of gold nanoparticles," *Colloids and Surfaces B: Biointerfaces*, vol. 80, no. 1, pp. 45-50, 2010.
- [88] D. A. Elliott, N. Nabavizadeh, S. K. Seung, E. K. Hansen, and J. M. Holland, "13 - Radiation Therapy," in *Oral, Head and Neck Oncology and Reconstructive Surgery*, R. B. Bell, R. P. Fernandes, and P. E. Andersen, Eds.: Elsevier, 2018, pp. 268-290.
- [89] J. E. McMurry, *Organic Chemistry with Biological Applications*. Cengage Learning, 2014.
- [90] A. Müllertz, Y. Perrie, and T. Rades, *Analytical techniques in the pharmaceutical sciences*. Springer, 2016.

-
- [91] T. Spectronic, "Basic UV-Vis theory, concepts and applications," *Thermo Spectronic*, pp. 1-28, 2012.
- [92] G. Wypych, "1 - PHOTOPHYSICS," in *Handbook of Material Weathering (Sixth Edition)*, G. Wypych, Ed.: ChemTec Publishing, 2018, pp. 1-26.
- [93] Y. Sharma, *Elementary organic spectroscopy*. S. Chand Publishing, 2007.
- [94] L. Reimer, *Transmission electron microscopy: physics of image formation and microanalysis*. Springer, 2013.
- [95] C. B. Carter and D. B. Williams, *Transmission electron microscopy: Diffraction, imaging, and spectrometry*. Springer, 2016.
- [96] Y. Javed, K. Ali, K. Akhtar, M. I. Hussain, G. Ahmad, and T. Arif, "TEM for Atomic-Scale Study: Fundamental, Instrumentation, and Applications in Nanotechnology," in *Handbook of Materials Characterization*: Springer, 2018, pp. 147-216.
- [97] B. Fultz and J. M. Howe, *Transmission electron microscopy and diffractometry of materials*. Springer Science & Business Media, 2012.
- [98] N. Tamura and P. U. Gilbert, "X-ray microdiffraction of biominerals," in *Methods in enzymology*, vol. 532: Elsevier, 2013, pp. 501-531.
- [99] S. Pabisch, W. Wagermaier, T. Zander, C. Li, and P. Fratzl, "Imaging the nanostructure of bone and dentin through small-and wide-angle X-ray scattering," in *Methods in enzymology*, vol. 532: Elsevier, 2013, pp. 391-413.
- [100] B. C. Smith, *Infrared spectral interpretation: a systematic approach*. CRC press, 2018.
- [101] D. N. Sathyanarayana, *Vibrational spectroscopy: theory and applications*. New Age International, 2015.

- [102] S. Kumar, F. Ye, S. Dobretsov, and J. Dutta, "Chitosan Nanocomposite Coatings for Food, Paints, and Water Treatment Applications," *Applied Sciences*, vol. 9, no. 12, p. 2409, 2019.
- [103] G. V. a. D. M. Mishra, "DEVELOPMENT AND OPTIMIZATION OF UV-VIS SPECTROSCOPY- A REVIEW," *World Journal of Pharmaceutical Research*, vol. 7, no. 11, pp. 1170-1180, 2018.
- [104] J. A. Rouse, "Chapter Three - Three Dimensional Computer Modeling of Electron Optical Systems**Reprinted from Advances in Optical and Electron Microscopy, vol. 13 (1994) 1–121," in *Advances in Imaging and Electron Physics*, vol. 208, P. W. Hawkes, Ed.: Elsevier, 2018, pp. 129-241.
- [105] R. F. Egerton, *Physical principles of electron microscopy*. Springer, 2005.
- [106] W. Sigle, "Analytical transmission electron microscopy," *Annu. Rev. Mater. Res.*, vol. 35, pp. 239-314, 2005.
- [107] S. Rajeshkumar, L. V. Bharath, and R. Geetha, "Chapter 17 - Broad spectrum antibacterial silver nanoparticle green synthesis: Characterization, and mechanism of action," in *Green Synthesis, Characterization and Applications of Nanoparticles*, A. K. Shukla and S. Iravani, Eds.: Elsevier, 2019, pp. 429-444.
- [108] L. Zhang, "X-Ray Absorption Spectroscopy of Metalloproteins," in *Metalloproteins: Methods and Protocols*, Y. Hu, Ed. New York, NY: Springer New York, 2019, pp. 179-195.
- [109] O. Tache and O. Spalla, "Optical device for analyzing a specimen by the scattering of an X-ray beam and associated collimation device and collimator," ed: Google Patents, 2015.
- [110] S. M. FLETCHER, "X-ray beam collimator," ed: Google Patents, 2019.

- [111] R. Kohli, "Chapter 3 - Methods for Monitoring and Measuring Cleanliness of Surfaces," in *Developments in Surface Contamination and Cleaning*, R. Kohli and K. L. Mittal, Eds. Oxford: William Andrew Publishing, 2012, pp. 107-178.
- [112] R. M. Gendreau, *Spectroscopy in the biomedical sciences*. CRC Press, 2018.
- [113] P. Capper and C. Elliott, *Infrared detectors and emitters: materials and devices*. Springer Science & Business Media, 2013.
- [114] J. Jana, M. Ganguly, and T. Pal, "Enlightening surface plasmon resonance effect of metal nanoparticles for practical spectroscopic application," *RSC advances*, vol. 6, no. 89, pp. 86174-86211, 2016.
- [115] C. R. Zamarreño, P. J. Rivero, M. Hernaez, J. Goicoechea, I. R. Matías, and F. J. Arregui, "Chapter 18 - Optical Sensors for Corrosion Monitoring," in *Intelligent Coatings for Corrosion Control*, A. Tiwari, J. Rawlins, and L. H. Hihara, Eds. Boston: Butterworth-Heinemann, 2015, pp. 603-640.
- [116] C. Louis and O. Pluchery, *Gold nanoparticles for physics, chemistry and biology*. World Scientific, 2012.
- [117] V. Rivera, F. Ferri, and E. Marega Jr, "Localized surface plasmon resonances: noble metal nanoparticle interaction with rare-earth ions," *Plasmonics-Principles and Applications*, pp. 283-312, 2012.
- [118] S. Peiris, J. McMurtrie, and H.-Y. Zhu, "Metal nanoparticle photocatalysts: emerging processes for green organic synthesis," *Catalysis Science & Technology*, vol. 6, no. 2, pp. 320-338, 2016.
- [119] N. M. Saleh and A. A. Aziz, "Simulation of Surface Plasmon Resonance on Different Size of a Single Gold Nanoparticle," in *Journal of Physics: Conference Series*, 2018, vol. 1083, no. 1, p. 012041: IOP Publishing.

- [120] M. Ramakrishna, D. R. Babu, R. M. Gengan, S. Chandra, and G. N. Rao, "Green synthesis of gold nanoparticles using marine algae and evaluation of their catalytic activity," *Journal of Nanostructure in Chemistry*, vol. 6, no. 1, pp. 1-13, 2016.
- [121] A. Mishra and M. Sardar, "Isolation of Genomic DNA by Silane-Modified Iron Oxide Nanoparticles."
- [122] Y. Si, C. Guo, C. Xie, and Z. Xiong, "An Ultrasonication-Assisted Cobalt Hydroxide Composite with Enhanced Electrocatalytic Activity toward Oxygen Evolution Reaction," *Materials*, vol. 11, no. 10, p. 1912, 2018.
- [123] A. Acheampong, S. Okyem, C. O. Akoto, and K. A. Baah, "Antioxidant, antimicrobial and FTIR analysis of methanol root extract of *Cnestis ferruginea* and ethanol root extract of *Citrus limon*," *Journal of Pharmacognosy and Phytochemistry*, vol. 7, no. 4, pp. 2938-2946, 2018.
- [124] G. Sharifzade, A. Asghari, and M. Rajabi, "Highly effective adsorption of xanthene dyes (rhodamine B and erythrosine B) from aqueous solutions onto lemon citrus peel active carbon: characterization, resolving analysis, optimization and mechanistic studies," *RSC advances*, vol. 7, no. 9, pp. 5362-5371, 2017.
- [125] T. Ajayeoba, O. Atanda, A. Obadina, M. Bankole, and S. Brumbley, "The potential of lemon juice-ogi steep liquor mixtures in the reduction of *Listeria monocytogenes* contamination of ready-to-eat vegetables," *LWT*, vol. 74, pp. 534-541, 2016.
- [126] S. F. Shaikh, B. V. Jadhav, and R. P. Patil, "PHOTOCATALYTIC ACTIVITY OF ZN-CO-FERRITE NANOPARTICLE SYNTHESIZED USING LEMON AS GREEN BINDING AGENT BY SOL-GEL METHOD,"

- INDO AMERICAN JOURNAL OF PHARMACEUTICAL SCIENCES*, vol. 5, no. 1, pp. S89-S93, 2018.
- [127] G. Allaedini and A. Muhammad, "Study of influential factors in synthesis and characterization of cobalt oxide nanoparticles," *Journal of Nanostructure in Chemistry*, vol. 3, no. 1, p. 77, 2013.
- [128] M. Medvidovic-Kosanovic, A. Stankovic, M. Jozanovic, M. Drulak, and M. Ilic, "Electrochemical and UV/VIS Study of L-Histidine and Its Complexes with Cobalt and Nickel," *Croatica Chemica Acta*, vol. 91, no. 4, pp. 421-427, 2018.

Arabic Summary

تمت دراسة تأثير الجسيمات النانوية المحضرة على تركيز النيكل المذاب في الماء من خلال تطبيقها على مرشح ويلكرسون ومن ثم تمرير تركيزات مختلفة من محلول النيكل من خلال المرشح. ولاحظنا أن هناك علاقة بين شدة الامتصاص وتركيزه؛ حيث تزداد شدة الامتصاص مع زيادة تركيز النيكل المذاب في المحلول وفقًا لقانون بيرلامبرت. إلى جانب ذلك، انخفضت شدة امتصاص محلول النيكل بعد استخدام الجسيمات النانومترية على المرشح وتم تمرير هذا عليه. وقد أشارت الدراسة أن عند التركيزات المنخفضة لعنصر النيكل فإن جسيمات الفضة النانوية وجسيمات الكوبالت النانوي ليست نشطة مثل جسيمات الذهب والحديد النانوي وقد يرجع السبب إلى السالبة الكهربائية للعناصر. في المقابل، عند التركيزات العالية يكون تأثير الكوبالت النانوي أكثر كفاءة من جسيمات الذهب والحديد والفضة النانوية على التوالي. الفكرة العامة هي أن عند التركيزات المنخفضة لعنصر النيكل فإن الجسيمات النانوية ليست نشطة على خلاف التركيزات العالية فإن الجسيمات النانوية تكون أكثر فعالية؛ هذا يعني أنه يمكن الاستفادة من الجسيمات النانوية المحضرة في تنقية المياه من العناصر الثقيلة.

أظهرت نتائج توصيف حيود الأشعة السينية في المدى (25° ~ 60°) لعينات الحديد النانوية المحضرة أن شدة قمم الحيود للجسيمات تتغير مع تغير نسبة ملح الحديد حيث يصبح شدة الحيود أكثر وضوحاً بزيادة ملح الحديد. وقد تم حساب متوسط حجم البلورات لجسيمات الحديد النانوية باستخدام معادلة شيرير، ووجد أنها 38.2 نانومتر و34.1 نانومتر و49.5 نانومتر. كما تم قياس نمط حيود الأشعة السينية في نطاق يتراوح ما بين (30° ~ 60°) لجسيمات الكوبالت النانومترية وقد أظهرت النتائج أن هناك علاقة طردية بين التركيز والشدة حيث يزداد شدة نمط الحيود بزيادة تركيز هيدروكسيد الصوديوم. بالإضافة إلى ذلك تم حساب الحجم البلوري لجسيمات الكوبالت النانوي من خلال معادلة شيرير، ووجدت أنها تعادل 32.9 نانومتر و31.3 نانومتر و41.5 نانومتر.

أظهرت نتائج التحليل الطيفي للأشعة تحت الحمراء لعينات الذهب النانوية المغلفة بمستخلص عصير الليمون أشربة امتصاص عند 621 سم⁻¹ و609 سم⁻¹ و602 سم⁻¹ والتي تم تفسيرها بالنمط الإهتزازي للمجموعة الكيميائية Au – O. في حين أن جسيمات الفضة النانوية المغلفة بمستخلص عصير الليمون أظهرت أشربة امتصاص عند 567 سم⁻¹ و592 سم⁻¹ و587 سم⁻¹ وفسرت بأنها مخصصة لمجموعة Ag – O. كما أظهرت جسيمات الحديد النانوية المغلفة بالشيتوزان أشربة امتصاص عند 642 سم⁻¹ و647 سم⁻¹ و650 سم⁻¹ والتي فسرت بالنمط الفيزيائي للمجموعة الكيميائية Fe – O. بينما بيّنت نتائج التحليل الطيفي لجسيمات الكوبالت النانوية اشربة امتصاص عند 512 سم⁻¹ و528 سم⁻¹ و532 سم⁻¹ وهي مخصصة للمجموعة الوظيفية Co – O. وقد تم حساب الشد الإهتزازي للأعداد الموجية بالطريقة النظرية لعدد من عينات من الجسيمات النانوية المحضرة ووجدت أن لها الأعداد الموجية 757.04 سم⁻¹ و778.76 سم⁻¹ و824.33 سم⁻¹ و819.43 سم⁻¹ والتي خصصت للمجموعات الوظيفية Au – O و Ag – O و Fe – O و Co – O على التوالي. وأشارت تلك النتائج إلى أن هناك اختلافات بين النتائج النظرية والعملية وقد أعزى السبب إلى وجود مجموعات وظيفية أخرى من الناحية العملية ترتبط مع جزيء Au – O و Ag – O و Fe – O و Co – O كما ظهرت مجموعات وظيفية في العينات مثل C – H و N – H و C – C و C = O وقد أعزيت ظهور هذه المجموعات إلى المواد المغلفة للمواد النانومترية، وقد تشترك جميع العينات في أن لها اشربة امتصاص عند حوالي 3400 سم⁻¹ وهي مخصصة للمجموعة الوظيفية O – H والتي تتعلق بالمياه الموجودة في العينات.

تمت دراسة وتحديد اشكال العينات المحضرة عبر جهاز المجهر الالكتروني النافذ عالي الدقة HR-TEM مع تقدير متوسط حجم الجسيمات الكروية لها. وقد دلت الدراسة إلى أن جسيمات الذهب النانوية AuNPs المحضرة قد ظهرت بأشكال كروية مع أشكال هندسية مختلفة أخرى مثل ثلاثي الشكل وخماسي وسداسي وشبه منحرف ومستطيل وقضيب صغير وبيضاوي وقد تم حساب متوسط حجم جسيمات الذهب النانوية للأشكال الكروية وفقاً لتوزيع غاوس ووجد أن لها الحجم 54 نانومتر و22 نانومتر و28 نانومتر. أشارت هذه النتائج أن بعض من العينات تتوافق مع نتائج الأشعة المرئية والفوق البنفسجية والبعض الآخر قد لا يتفق، وأعزى السبب إلى وجود الأشكال غير المنتظمة بجانب الأشكال الكروية التي ظهرت في الصورة. كما اظهرت نتائج المجهر الالكتروني النافذ من أن جسيمات الفضة النانوية لها توزيعاً عشوائياً يغلب عليها الشكل الكروي ناعم الحواف والسطح، كما أن لها أشكالاً هندسية أخرى مثل الشكل البيضاوي والسداسي وقد تم حساب متوسط حجم جسيمات الفضة النانوية وفقاً للتوزيع الغاوسي للجسيمات الكروية في الصورة وتبين أن له الحجم 31 نانومتر و15 نانومتر و28 نانومتر. هذه النتائج غير متوافقة مع موضع نطاق البلازمون لبيانات الأشعة المرئية والفوق البنفسجية ويمكن أن تعزى إلى التجميع الذي حدث أثناء تصوير العينات. من ناحية أخرى، تم توصيف جسيمات الحديد النانوية بعد وقبل التجفيف عبر المجهر الالكتروني النافذ وقد أظهرت النتائج توزيعاً عشوائياً للجسيمات غير المنتظمة والمتجانسة إلى جانب الأشكال الكروية. وقد تم حساب متوسط حجم جسيمات الشكل الكروي وكان له الحجم 22 نانومتر و17 نانومتر و32 نانومتر للعينات بعد التجفيف و 10 نانومتر و9 نانومتر و18 نانومتر للعينات قبل التجفيف. لوحظ أن جسيمات الحديد النانوية بعد التجفيف تظهر بحجم جسيمات أكبر مما كانت عليه قبل التجفيف؛ ربما يرجع ذلك إلى تجمع الجسيمات النانوية بعد عملية التسخين. وقد بيّنت صور جسيمات الكوبالت النانوي للعيينة الأولى ظهور أشكال كروية وبيضاوية الشكل وخماسية وسداسية مع جسيمات أخرى متجمعة؛ حيث بلغ متوسط حجم الجسيمات لهذه العينة 27 نانومتر وفقاً لتوزيع غاوس. في حين ظهرت مورفولوجيا العيّنتين الأخيرتين على شكل ألياف وقضبان نانوية بنسبة الطول الى القطر ما بين 5.2 ~ 8.5 نانومتر و5.6 ~ 8.33 نانومتر مع ظهور بعضاً من الجسيمات الغامضة، تكاد هذه العيّنتين لاتحتوي على أشكال كروية لهذا السبب تم تجاهل حساب متوسط حجم الجسيمات لها.

الفصل الرابع

في هذا الفصل، تمت مناقشة وتفسير النتائج التي تم الحصول عليها من العينات المحضرة. حيث أظهرت نتائج تحليل الامتصاص الطيفي للأشعة المرئية والفوق البنفسجية لجسيمات الذهب النانوية AuNPs في المدى (300 نانومتر - 900 نانومتر) ظهور أشربة عند الطول الموجي 564 نانومتر و556 نانومتر و548 نانومتر، وقد فسرت هذه الأشربة بالرنين البلازموني السطحي SPR. ولوحظ أن هناك علاقة عكسية بين نسبة مستخلص عصير الليمون وموضع نطاق رنين السطح البلازموني SPR حيث يقل الطول الموجي مع زيادة المستخلص وهذا يشير إلى انخفاض حجم جسيمات الذهب النانومترية. في حين أظهرت قياس امتصاص الأشعة المرئية والفوق البنفسجية لجسيمات الفضة النانوية AgNPs في المدى (320 نانومتر - 890 نانومتر) أشربة عند الطول الموجي 432 نانومتر و452 نانومتر و448 نانومتر والتي فسرت أيضاً بالرنين البلازموني السطحي للفضة النانومترية. وقد لوحظ أن الطول الموجي يزداد مع زيادة تركيز نترات الفضة $AgNO_3$ للعينتين الأولى ثم تنخفض في العينة الثالثة مرة أخرى. وقد فسرت زيادة الطول الموجي للفضة النانومترية AgNPs إلى زيادة ايونات الفضة Ag^+ اثناء عملية التحضير، أما بالنسبة لإنخفاض الطول الموجي مرة أخرى فقد اعزيت إلى زيادة نسبة ملح الفضة مما أدى إلى ظهور جسيمات نانوية أكثر ولكن بحجم صغير. أيضاً بيّنت نتائج التحليل الطيفي لجسيمات الحديد النانوية FeNPs في المدى (205 نانومتر - 800 نانومتر) ظهور طيف امتصاص عند الطول الموجي 336 نانومتر و340 نانومتر و344 نانومتر. وقد أشارت النتائج أن هناك علاقة طردية بين زيادة نسبة ملح الحديد وطوله الموجي كما هو معروف تقليدياً. ومن ثم فسرنا أن زيادة الطول الموجي كان بسبب زيادة ايونات الحديد في المحلول مما أدى إلى الزيادة التّنوي بالتالي الزيادة في حجم الجسيمات النانومترية. اضافة الى ذلك، تم قياس نتائج امتصاص طيف الأشعة المرئية والفوق البنفسجية لجسيمات الكوبالت النانوية المحضرة CoNPs في المدى (250 نانومتر - 800 نانومتر) وقد أظهرت النتائج ظهور أشربة امتصاص عند الاطوال الموجية 520 نانومتر و548 نانومتر و528 نانومتر. ولوحظ أن هناك زيادة في الاطوال الموجية للعينتين الأولى ومن ثم انخفاضها مرة أخرى. يرجع زيادة حجم الجسيمات إلى زيادة هيدروكسيد الصوديوم في المحلول والذي يعمل على تكوين الجسيمات النانوية أما الإنخفاض مرة أخرى في الطول الموجي يشير إلى تحول الجسيمات النانوية إلى قضبان وألياف نانومترية، وقد أشارت نتائج الطول الموجي إلى تكون جسيمات نانوية بأحجام وأشكال مختلفة.

الفصل الثاني

يوضح هذا الفصل الإطار النظري والأساسيات الرياضية للأجهزة المستخدمة في عمليات قياس وتوصيف جسيمات النانو المحضرة. وقد بدأ بشرح الخلفية النظرية للأشعة الكهرومغناطيسية. تلى ذلك، مناقشة جهاز مطياف الأشعة المرئية والفوق بنفسجية مروراً بمبادئ امتصاص الضوء من خلال قانون بيرلامبرت و شرح لمستويات الإنبعاثات الإلكترونية نتيجة تعرضها لهذه الأشعة. كما تمت مناقشة الأساسيات النظرية لجهاز المجهر الإلكتروني النافذ وكيفية توليد شعاع الإلكترون وطريقة تفاعله مع العينة. بالإضافة إلى توضيح الإطار النظري لمقياس حيود الأشعة السينية مع شرح تفصيلي لقانون براغ. أما الجزء الاخير من هذا الفصل فقد تناول بعضاً من المفاهيم الأساسية لمطياف الأشعة تحت الحمراء متضمناً الأطوال الموجية الخاصة بها مع توضيح الأساسيات الرياضية لإمتصاص الطيف و من ثم اهتزازه بأعداد معينة.

الفصل الثالث

بداية هذا الفصل قُدم فيه عرضاً وافياً للمواد الكيميائية المستخدمة في تحضير الجسيمات النانوية مع طرق تحضيرها وفي نهاية الفصل تم عرض التقنيات العملية المستخدمة في التوصيف. تم تحضير جسيمات الذهب النانوية باستخدام نسب متساوية من ملح الذهب (كلورايد الهيدرات $HAuCl_4 \cdot H_2O$) مع تغيير تركيز كمية مستخلص عصير الليمون في العينات كما تم تحضير جسيمات الفضة النانوية باستخدام نسب مختلفة من ملح الفضة (نترات الفضة $AgNO_3$) مع نسب ثابتة من تركيز كمية مستخلص عصير الليمون في العينات. إضافةً إلى ذلك، تم تحضير جسيمات الحديد المغناطيسية المغطاة بالشيتوزان باستخدام نسب مولية مختلفة من ملح الحديد الثنائي والثلاثي (كلوريد الحديد $FeCl_2 \cdot 4H_2O$ ونترات الحديد $Fe(NO_3)_3 \cdot 9H_2O$) مع تثبيت نسبي كلاً من الشيتوزان وهيدروكسيد الصوديوم $NaOH$ كما تم تحضير جسيمات الكوبالت النانوية وذلك بإضافة نسب متساوية من ملح الكوبالت (كلوريد الكوبالت $CoCl_2 \cdot 6H_2O$) مع اختلاف نسب هيدروكسيد الصوديوم $NaOH$.

الملخص باللغة العربية

تهتم هذه الرسالة بتحضير وتوصيف جسيمات المعادن النانوية (الذهب والفضة) وبعض من الجسيمات المغناطيسية النانوية (الحديد و الكوبالت) بأحجام مختلفة ودراسة خصائصها الطيفية، بالإضافة إلى دراسة تأثير جسيمات النانو المحضرة على تركيز النيكل المذاب في الماء بتركيزات مختلفة. وقد نُظمت هذه الأطروحة العلمية إلى أربعة فصول مدعمة بالأشكال التوضيحية والرسوم البيانية والجداول والمعادلات اللازمة؛ حيث احتوى الفصل الأول على مقدمة عامة للنانو مع استعراض عدد من الدراسات السابقة المتعلقة بالبحث، الفصل الثاني وقد اشتمل على الأساسيات النظرية للأجهزة التي استخدمت في قياس العينات المحضرة و التي تم التطرق لها بينما احتوى الفصل الثالث على الطرق التجريبية لتحضير المواد النانومترية متضمناً الأجهزة المستخدمة في القياس واخيراً الفصل الرابع وقد تمت فيه مناقشة النتائج والقياسات التي تم الحصول عليها من كافة البحث.

الفصل الاول

احتوى هذا الفصل على جزئين رئيسيين وهما؛ خلفية عامة عن المواد النانوية والمسح الادبي. بدأ الجزء الأول بموجز لعلم النانو مع بعض التعريفات لتقنية النانو ثم تصنيف المواد النانوية اعتماداً على ابعادها في المدى النانومتري تلى ذلك ذكر العوامل الرئيسية التي تتوقف عليها خواص المواد النانوية وهما طاقة السطح وتأثير الحصر الكمومي ثم خصائص المواد النانوية الفريدة متضمناً المميزات النانوية الميكانيكية والمغناطيسية و البصرية. بالإضافة الى لمحة عامة لطرق تحضير المواد النانوية سواءً من الأعلى الى الأسفل او من الأسفل الى الأعلى مع شرح بعض الأمثلة لتقنيات التحضير الكيميائية والفيزيائية مثل الطحن بالكرة وترسيب البخار الكيميائي وطريقة السائل الجيلاتيني والاستئصال بالليزر. كما تم شرح طرق تحضير المواد المعدنية والمغناطيسية مع شرح لتوضيح تطبيقات النانو في الزراعة و الطعام والطب و الطاقة وتنقية المياه.

الجزء الثاني تم فيه عرض عدد من الدراسات السابقة المتعلقة بتحضير الجسيمات النانوية المعدنية والمغناطيسية كالذهب والفضة والحديد و الكوبالت وتطبيقاتها في البيئة وفي اخر هذا الفصل تم توضيح الاهداف و خطة العمل.

الملخص باللغة العربية

الإهداء

وهدي هذه الرسالة العلمية لي
والدي ووالدتي اللذان تأسيت شخصيتي من تربيتهم و
حكمتهم وتوفقت بعد توفيق الله برعايتهم،

إخواني سندي في هذه الحياة، ولى إخواني وأعمام عطايا رب العالمين،

وإلى كل طالب علم يسعى لكسب المعرفة وتزويد رصيده المعرفي والعلمي والثقافي.

وأسأل الله أن يجعله نبراساً لطلاب العلم.

نجوي برناوي

1441-2020



المملكة العربية السعودية

وزارة التعليم العالي

جامعة أم القرى

كلية العلوم التطبيقية

قسم الفيزياء

تحضير وتوصيف ودراسات طيفية للجسيمات النانوية المعدنية وتطبيقاتها في البيئة

رسالة مقدمة الى

قسم الفيزياء – كلية العلوم التطبيقية – جامعة أم القرى

كجزء مكمل للحصول على درجة الماجستير في العلوم (فيزياء)

الطالبة

نجوى علي محمد برناوي

(بكالوريوس فيزياء)

الرقم الجامعي: 43880124

تحت إشراف

أ.د. رشدي سعودي محمد عوض

أستاذ الأطياف وتقنية النانو

قسم الفيزياء – كلية العلوم التطبيقية – جامعة أم القرى

مساعد مشرف

أ.د. سعود حميد اللحواني

أستاذ الفيزياء الطبية

قسم الفيزياء – كلية العلوم التطبيقية – جامعة أم القرى

2020 م – 1441 هـ